



# Antarctic site testing : measurement of optical seeing at the South Pole

**Author:**

Marks, Rodney

**Publication Date:**

2005

**DOI:**

<https://doi.org/10.26190/unsworks/20081>

**License:**

<https://creativecommons.org/licenses/by-nc-nd/3.0/au/>

Link to license to see what you are allowed to do with this resource.

Downloaded from <http://hdl.handle.net/1959.4/58904> in <https://unsworks.unsw.edu.au> on 2024-04-30

**ANTARCTIC SITE TESTING:  
MEASUREMENT OF OPTICAL SEEING AT  
THE SOUTH POLE**

by

Rodney Marks

A thesis submitted in satisfaction of  
the requirements for the degree of

**Doctor of Philosophy**

in the Faculty of Science

**THE UNIVERSITY OF  
NEW SOUTH WALES**



May 2005

## STATEMENT OF ORIGINALITY

I hereby declare that this submission is my own work and to the best of my knowledge it contains no materials previously published or written by another person, nor material which to a substantial extent has been accepted for the award of any other degree or diploma at UNSW or any other educational institution, except where due acknowledgement is made in the thesis. Any contribution made to the research by others, with whom I have worked at UNSW or elsewhere, is explicitly acknowledged in the thesis.

I also declare that the intellectual content of this thesis is the product of my own work, except to the extent that assistance from others in the project's design and conception or in style, presentation and linguistic expression is acknowledged.

Rodney Marks

Rodney Marks died at the US Amundsen-Scott South Pole Station on 12 May 2000, after having written this PhD thesis, but before it was submitted. Darryn Schneider, a colleague of Rodney's at the South Pole, helped collate the chapters and figures into a suitable form. Melinda Taylor made typographical corrections and organised submission. Michael Burton wrote a short conclusion.

Michael Ashley 04 April 2005

## ABSTRACT

The effect of atmospheric turbulence on astronomical image quality, or “seeing”, has been studied at the South Pole, by measuring the microthermal fluctuations associated with the turbulence. The site-testing campaign took place over two years; during the first year, the contribution of the lower-boundary layer was examined, while the second year included measurement of the entire atmosphere.

The surface-layer study consisted of an array of microthermal sensors placed at three levels on a 27 m-high tower. The seeing contribution from this region was very large in comparison with similar experiments performed at other sites, with a measured mean value of  $0.64''$ . The optical turbulence often decreases sharply over the height of the mast. These measurements coincide with a large and highly variable temperature inversion, the behaviour of which is often correlated with the observed turbulence profile.

In the following season, the total atmospheric seeing was measured using balloon-borne microthermal probes. A marked division of the atmosphere into two characteristic regions was observed: (i) a highly turbulent boundary layer (0–220 m) associated with a strong temperature inversion and wind shear, and (ii) a very stable free atmosphere. The mean seeing, averaged over 15 balloon flights, was  $1.86''$  of which the free atmosphere component was only  $0.37''$ . The seeing from  $\sim 200$  m upward is hence greatly superior to the leading mid-latitude sites. It is also a highly favourable situation for the use of image correction techniques, and comparisons are made between the relevant adaptive optics parameters measured at the South Pole and some of the other sites.

Since the boundary layer seeing is strongly influenced by the inversion wind, it is possible that exceptionally good seeing may occur from surface level at other locations on the plateau such as Domes A and C, where the inversion wind is almost non-existent. The likely seeing conditions at some of these locations are discussed, based on the available weather data, and in light of the results from the South Pole.

# Contents

<b>Abstract</b>	<b>i</b>
<b>List of Figures</b>	<b>ii</b>
<b>List of Tables</b>	<b>iii</b>
<b>1 INTRODUCTION</b>	<b>1</b>
<b>2 BACKGROUND</b>	<b>11</b>
2.1 Theory . . . . .	11
2.1.1 Optical properties of atmospheric turbulence . . . . .	11
2.1.2 Turbulent layers in the atmosphere . . . . .	13
2.1.3 Adaptive optics . . . . .	15
2.2 Microthermal measurement of seeing . . . . .	16
2.2.1 Earlier results . . . . .	16
2.2.2 Microthermal sensors . . . . .	18
<b>3 SURFACE LAYER SEEING</b>	<b>21</b>
3.1 Procedure . . . . .	23
3.1.1 Hardware . . . . .	23
3.1.2 Software & data acquisition . . . . .	25
3.1.3 Data reduction . . . . .	27
3.2 Results . . . . .	28
3.2.1 Summary . . . . .	29
3.2.2 Characteristics of individual measurements . . . . .	32

3.3	Comparison with other sites . . . . .	40
3.4	Discussion . . . . .	41
<b>4</b>	<b>BOUNDARY LAYER / FREE ATMOSPHERE SEEING</b>	<b>45</b>
4.1	Method . . . . .	46
4.2	Results . . . . .	48
4.2.1	Summary . . . . .	48
4.2.2	Boundary layer characteristics . . . . .	54
4.2.3	Free atmosphere characteristics . . . . .	62
4.2.4	H-DIMM observations . . . . .	68
4.3	Comparison with other sites . . . . .	70
4.3.1	Overview . . . . .	70
4.3.2	Comparison of microthermal measurements at the South Pole and Cerro Paranal . . . . .	71
4.3.3	$C_N^2$ profiles at other sites . . . . .	72
4.4	Adaptive optics parameters . . . . .	75
4.4.1	Angular and temporal isoplanatism . . . . .	76
4.4.2	Scintillation index . . . . .	83
4.5	IR results . . . . .	83
<b>5</b>	<b>DISCUSSION</b>	<b>88</b>
5.1	Temperature comparisons . . . . .	90
5.2	Wind comparisons . . . . .	93
<b>6</b>	<b>CONCLUSION</b>	<b>97</b>
	<b>References</b>	<b>100</b>

# List of Figures

1.1	Map of Antarctica . . . . .	3
1.2	Near-infrared and sub-mm atmospheric transmission . . . . .	5
1.3	Zonal wind speeds for the northern hemisphere. . . . .	7
2.1	Theoretical model of $C_N^2$ intensity . . . . .	15
2.2	$C_N^2$ profiles . . . . .	17
2.3	Schematic of the $D_T$ sensor cicuity . . . . .	19
3.1	The NOAA tower . . . . .	22
3.2	Arrangement of sensors on the 27 m Met Tower . . . . .	24
3.3	<i>Seeing data statistics</i> . . . . .	31
3.4	$C_N^2$ vs. time . . . . .	34
3.5	$C_N^2$ vs time - Case i and ii . . . . .	36
3.6	$C_N^2$ vs time - Case iii and iv . . . . .	39
3.7	Comparison of the $C_N^2$ profile . . . . .	42
4.1	<i>Seeing data statistics</i> . . . . .	49
4.2	Average $C_N^2$ profile up to a height of 70 m . . . . .	51
4.3	$C_N^2$ vs altitude . . . . .	53
4.4	$C_N^2$ vs altitude . . . . .	56
4.5	Average $C_N^2$ profiles up to a height of 1km . . . . .	58
4.6	Comparison of all significant peaks . . . . .	60
4.7	$C_T^2$ vs $ d\theta/dz $ for $C_T^2$ peaks . . . . .	61
4.8	Average vertical wind speed profiles . . . . .	63
4.9	$C_N^2$ $ dU/dz $ and potential temperature profiles . . . . .	64
4.10	$C_N^2$ $ dU/dz $ and potential temperature profiles in the region 7–9 km . . . . .	66
4.11	A comparison of $C_N^2$ and $R_i$ profiles . . . . .	67
4.12	Comparison of H-DIMM and microthermal seeing measurements . . . . .	69
4.13	Comparison of Seeing as a function of height . . . . .	73

4.14	Comparison with the $C_N^2$ profile . . . . .	74
4.15	$\theta_{AO/SI}$ , as a function of the residual seeing $\epsilon_r$ . . . . .	79
4.16	Percentage sky coverage as a function of the residual seeing . . . . .	81
4.17	Distribution of the value of $\sigma_1^2$ . . . . .	84
4.18	South Pole / Paranal seeing comparison . . . . .	85
4.19	$\theta$ vs $\epsilon$ for $K= 2.4\mu\text{m}$ . . . . .	86
5.1	Contour map of temperature inversion strengt . . . . .	91
5.2	Variation of temperature inversion over a 24 hour period . . . . .	92
5.3	Contour map of surface wind directions . . . . .	94

# List of Tables

3.1	Turbulence contributions to surface layer seeing . . . . .	30
3.2	Characteristic data observed from the mast . . . . .	35
4.1	Summary of integrated seeing and boundary layer data . . . . .	50
4.2	Comparison of seeing conditions . . . . .	71
4.3	Summary of the astrophysical parameters . . . . .	77
4.4	Integrated seeing and boundary layer data . . . . .	87
5.1	Comparison of weather parameters . . . . .	89

# Chapter 1

## INTRODUCTION

One hundred years ago, the Antarctic was a mysterious, treacherous and unforgiving land; the last frontier, beyond the edge of the known world. It was a struggle for explorers just to survive in the stormy oceans of the Roaring Forties, and on the ice-bound coast, let alone carry out any of the scientific research that was ostensibly the main goal of their expeditions. The story of the first expeditions to the geographic South Pole of Amundsen and Scott is one of the great dramas of modern times. Not as widely known, but no less worthy, were the journeys of such explorers as Shackleton and Mawson, who travelled deep into the icy interior of the continent on epic voyages of exploration and discovery. The history of this heroic age of exploration remains an inspiration to scientists working in Antarctica almost a century later.

Nowadays, of course, many countries maintain a permanent presence “on the ice”, with dozens of research bases scattered around the coastline (and a very few inland). Life on an Antarctic station is no longer a battle for survival, and transportation to the continent by air and sea has become almost a routine operation. Antarctica has not been truly conquered, and it is still an exceptionally difficult task to carry out the increasingly ambitious scientific and technological projects that are undertaken there.

Of all the major research programs either proposed or underway in Antarctica, one of the most challenging is the proposal for a major astronomy observatory, on the high plateau of East Antarctica. If the astronomy community has its way, within 10–20 years there will be a large automated facility deep in the heart of the continent, preferably at the highest, coldest and driest site they can find. It is

believed that these barren and desolate places are nothing but the ideal locations on the planet for many kinds of astronomy.

The inaccessible upper reaches of the antarctic plateau present an unprecedented technological challenge for astronomers and telescope engineers, and it is only recently that the possibility of building an observatory there has been seriously considered (e.g. Vernin 1994, Gillingham 1993, Burton et al. 1994). Astrophysical research continues to grow rapidly, and as our understanding of the universe increases, so too does the demand for telescopes that can peer further into space, and penetrate deeper into areas that were previously hidden from view.

As it stands now, we appear to be approaching the limits of what is technologically achievable, in terms of telescope and detector engineering. The new generation of 8 m optical telescopes and large-format, high-efficiency detectors will not be surpassed without massive, and probably unjustifiable expense. Apart from financial considerations, as the sensitivity and resolution of the largest telescopes increase, so the characteristics of the sites at which they are located become the primary limitation in the quality of the observations. This is the case even at the high, desert sites chosen for such projects as the ESO-VLT where image resolution of 1'' is considered poor.

For these reasons, it is becoming an increasingly important priority, in terms of maximising scientific returns, to find gains in performance not by building larger telescopes, but rather, by choosing the optimum site. All of the major new observatory sites have undergone years of site-testing experiments to measure weather, seeing and transmission characteristics (e.g. ESO-VLT working group 1987, Murtagh & Sarazin 1995). The mid-latitudes have, by now, been fairly extensively surveyed in this sense, and it is generally agreed that the world's largest telescopes occupy the very best sites available, in terms of reasonably easily accessible locations. In order to make any gains on the present situation, it will be necessary to venture further afield.

Sending telescopes into the far-upper atmosphere and into space is extremely expensive, and has its own limitations in terms of the type and size of instrument that can be managed. It is at this point that the antarctic plateau begins to be seriously considered as an alternative site. Many astronomers believe that an observatory in Antarctica will have very great advantages over mid-latitude sites, and even approach the performance of a telescope in space in some cases, while not even coming close to the cost involved in the types of projects that might logically

succeed the Hubble Space Telescope (HST).

The reasoning behind this lies in the very characteristics of Antarctica that make it so daunting. “High”, “cold” and “dry” are the three key words that make the antarctic plateau, theoretically, the most favourable site for infrared, sub-millimeter, and millimeter wavelength astronomy on the surface of the earth. The high plateau, which includes the South Pole, covers an area of over  $3 \times 10^6$  km<sup>2</sup> above 3000 m (Fig. 1.1), and Antarctica is on average at a much higher altitude than any other continent (Schwerdtfeger 1984). The low pressure prevailing in the polar regions increases the equivalent altitude on the plateau by hundreds of metres further still. This places wide areas above a large fraction of the atmosphere which, alone, should mean significant improvements in atmospheric transmission for many wavelengths.

This great landmass is also the coldest place on earth by a long margin. The average temperature at the South Pole from sunset to sunrise is close to  $-60^\circ\text{C}$ , and can fall below  $-80^\circ\text{C}$ . Some of the higher points are even colder. This compares with the coldest mid-latitude sites, such as Mauna Kea in Hawaii, where the temperature rarely falls much below freezing. In the near and mid-infrared, where sensitivity is limited largely by the thermal background of the telescope and the atmosphere, the potential gains are obviously enormous. From  $2.27\text{--}2.45\ \mu\text{m}$  (K-band), for example, the low thermal background, combined with a natural minimum in airglow emission, is expected to reduce the sky brightness by a factor of 100 or more over other sites, down to a level close to the limit set by zodiacal emission (Burton et al. 1994). It seems likely, indeed, that windows will open up in the antarctic atmosphere through which the sky can barely be seen at all from temperate sites.

In addition, by most definitions the high antarctic plateau is also the largest desert in the world. Water vapour is the nemesis of astronomers who would hope to observe the skies in the sub-millimetre and millimetre wavebands. With precipitable water vapour columns averaging around 0.3 mm (about a factor of 10 lower than good mid-latitude sites) at the South Pole in winter, many sections of this large and very important region of the spectrum may, for the first time, be accessible to telescopes from the ground, where previously the only data had come from airborne telescopes such as the Kuiper Airborne Observatory (KAO).

Overall, many branches of astronomy might anticipate major benefits from an observatory in Antarctica. Fig. 1.2 shows the measured and theoretical atmospheric

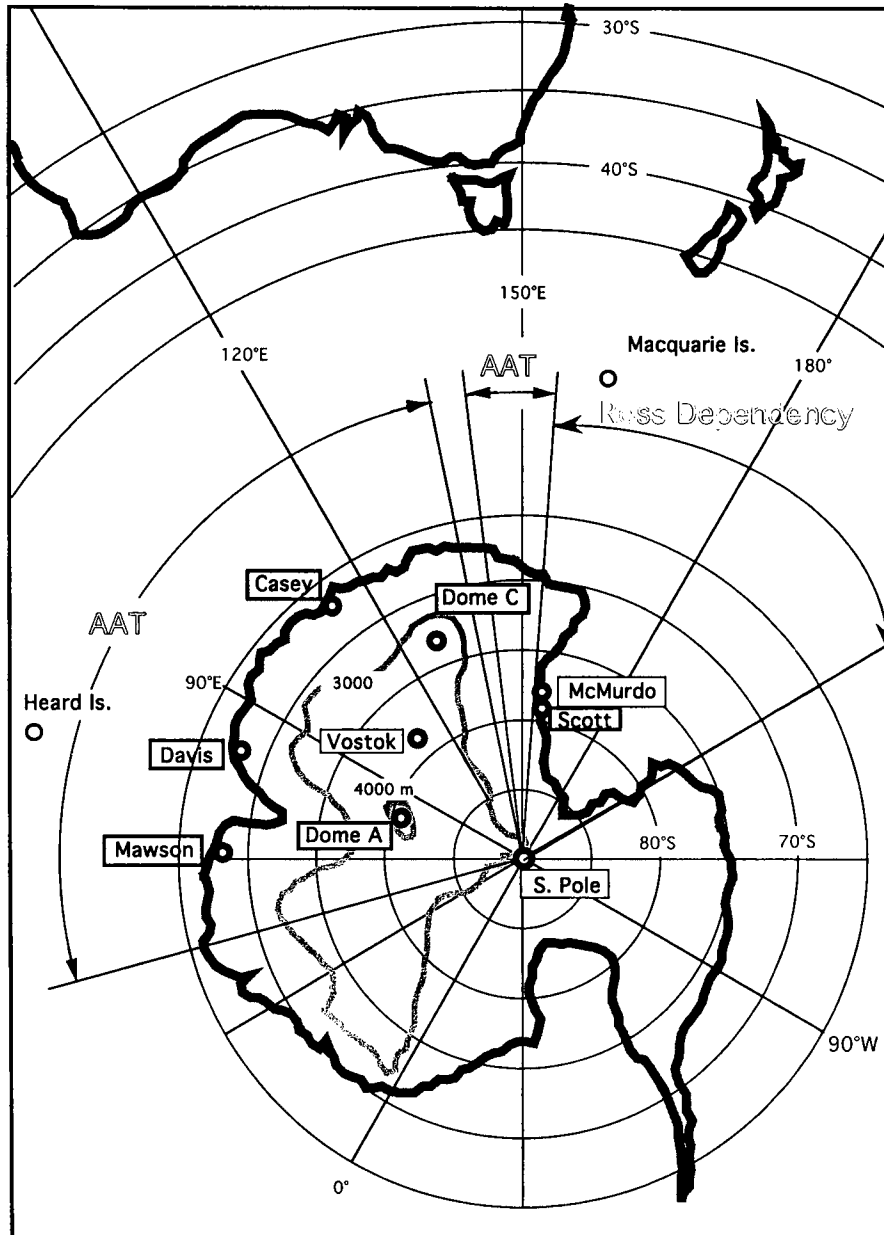


**Figure 1.1:** Map of Antarctica, showing the 3000 m and 4000 m contours, and the main sites under consideration on the high plateau. The range of the Australian Antarctic Territory is also indicated (Burton et al. 1994).

transmissions in the near-infrared and sub-millimeter wavebands, respectively, at the South Pole, with corresponding curves from Mauna Kea and Siding Spring Observatories included for comparison.

The points mentioned briefly here are the most fundamental arguments; however there are additional reasons to believe that the quality of astronomical observations will be improved in other ways. In particular, there is a strong possibility that the antarctic atmosphere may provide excellent conditions for high-resolution imagery at optical and infrared wavelengths. The fundamental limit on image quality at the shorter wavelengths is usually set by refractive index fluctuations associated with atmospheric turbulence, which cause distortions in the wavefront of an astronomical source as the light passes through the atmosphere. Turbulent disturbances generally occur in multiple thin layers, located at different altitudes depending on the site. The cumulative effect on image quality is known as “seeing”, and is one of the most important parameters defining the overall quality of an observatory site.

Little direct evidence is available on seeing conditions over the high plateau; some clues, however, are available from the meteorological records. The free atmosphere is expected to be very stable, with smooth wind and temperature gradients leading to exceptionally good seeing in this region. It is known from meteorological research that the upper-atmosphere jet streams common in temperate locations, and associated with the upper boundary of the troposphere at an altitude of around 10–12 km, can be very strong, averaging over  $40 \text{ ms}^{-1}$  in some places, as shown in Fig. 1.3(a) (McIlveen 1992). In contrast, high-altitude winds are very much weaker in the polar regions, with a relatively low (7–8 km) and less marked tropopause, as shown in Fig. 1.3(b). Upper atmosphere turbulence of this nature is a significant component of the seeing at many locations, and the lack of any apparent indicators for such turbulence on the antarctic plateau have led to the coining of the phrase “Super Seeing” (Gillingham 1993). In addition, the diurnal variation that is a significant factor contributing to optical turbulence in the boundary layer at most sites is absent in Antarctica; at least at all potential antarctic astronomy sites.

Mitigating against good seeing from the surface, however, is the intense temperature inversion, pervasive over the plateau during the winter months, and often exceeding  $0.1^\circ\text{Cm}^{-1}$  averaged over the entire boundary layer. The limited data available on boundary layer turbulence (Neff 1981) indicates some very intense optical turbulence, concentrated in quite narrow layers, extends throughout the lower

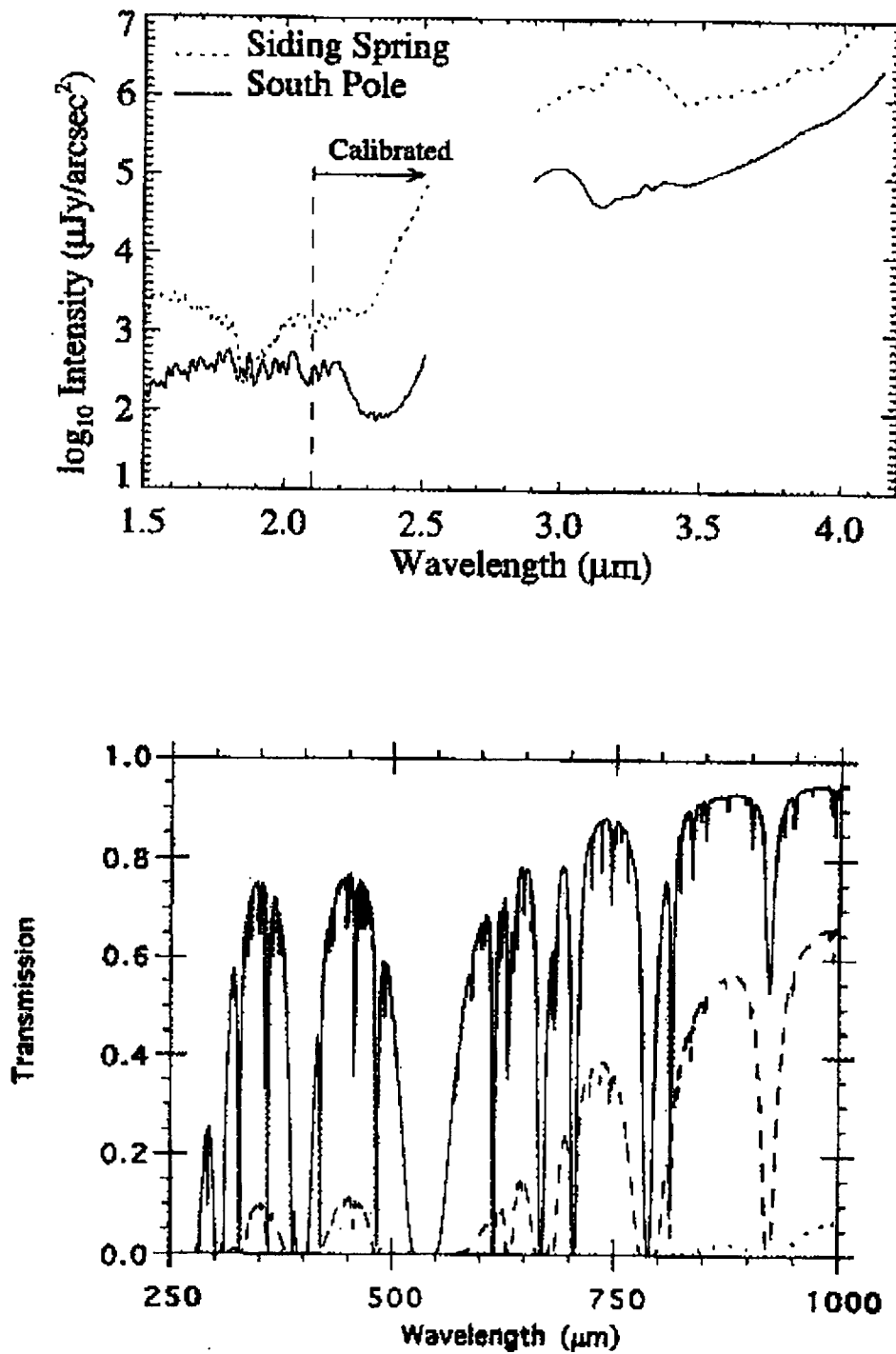


Figure 1.2: a) near-infrared atmospheric transmission at the South Pole and Siding Spring (Phillips et al. 1999), b) sub-mm transmission at the South Pole (solid line), Mauna Kea (dashed line) and Siding Spring (dotted line) (Burton et al. 1994)

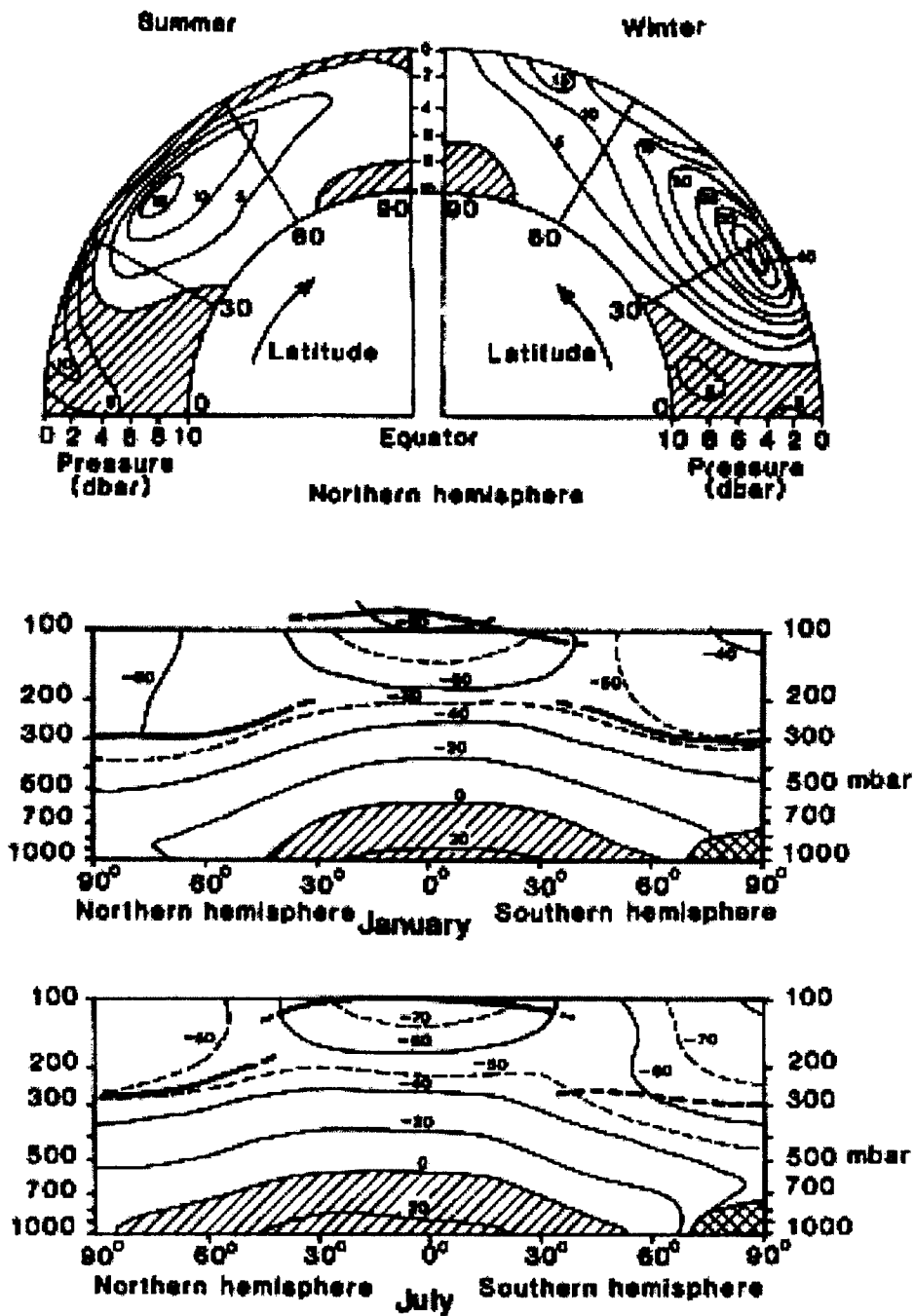


Figure 1.3: a) Seasonally averaged zonal (i.e. east-west) wind speeds for the northern hemisphere. Isotachs are labelled in  $\text{ms}^{-1}$ , vertical scales show the pressure in units of dbar, and shaded areas represent easterly components; all others are westerly. Peaks upper atmosphere winds in the southern hemisphere are slightly stronger than the values shown here, b) Average monthly isotherms for January and July. The dark line indicates the approximate altitude of the tropopause (McIlveen 1992)

parts of the inversion, which has a vertical extent of some 300–500 m. On the other hand, the fact that this atmospheric disturbance is concentrated so close to the surface, in comparison to the turbulence at other sites, might well have its own advantages. Most large telescopes these days employ some type of real-time image correction technique, which broadly come under the title of “adaptive optics”. The effectiveness of such methods is severely restricted by angular and temporal limitations set by the nature of the atmospheric turbulence. In general, the scale of these parameters is inversely proportional to the altitude of the turbulent layers, and hence high-altitude turbulence is much more difficult to correct than low-altitude disturbances (see, for example, Cowie & Songaila 1988, Olivier 1993). Hence, even if the boundary-layer seeing is poor, it may be relatively easy to eliminate this component over larger areas than is possible at other sites. A similar altitude dependence also applies to the scintillation of stellar sources caused by atmospheric turbulence. The expected vertical structure over the Antarctica plateau should therefore lend to more accurate photometry, especially in such fields as astroseismology and the study of variable stars.

Other factors unique to Antarctica are the ability to track sources for long periods of time through roughly the same airmass (exactly the same, of course, at the South Pole); the possibility of a large proportion of clear weather at the higher locations; and the absence of any natural or artificial sources of pollution or electromagnetic interference.

As astronomers began to consider the potential advantages of observing from Antarctica, it soon became a high priority that many of the factors noted above be analysed and quantified as rapidly as possible (Dopita 1993, Gillingham 1993). Unfortunately, there were only two permanently staffed research bases in the interior of the continent (which has since been reduced to a single station at the South Pole), and data pertinent to astronomical site quality was almost nonexistent. This led to the development of an international collaboration to determine the site characteristics at the South Pole, as a first step towards quantifying the benefits of building a large observatory somewhere on the plateau. This program grew within the structure of the US Center for Astrophysical Research in Antarctica (CARA), which is the umbrella organisation for astronomy at South Pole Station. Members from the Joint Australian Centre for Astrophysical Research in Antarctica (JACARA, Australia), and the Département d’Astrophysique, Université de Nice

(France) added their various expertise to the projects.

Beginning in late 1993, a suite of experiments was put in place at the South Pole, designed to measure atmospheric transmission at near and mid-infrared wavelengths (Ashley et al. 1995), and to determine the seeing contribution from both the boundary layer and the free atmosphere (Marks et al. 1996). Measurement of near-infrared sky brightness has confirmed expectations (Fig. 1.2(a)), with an exceptionally dark sky observed out to 4–5  $\mu\text{m}$  (M-band), which opens up the possibility of observations rarely even attempted from the surface before (Ashley et al. 1995, Nguyen et al. 1996, Phillips et al. 1999). Similar results have been obtained in the mid-infrared from approximately 10–20  $\mu\text{m}$  (Smith & Harper 1998).

It is the experiments measuring the seeing that are the subject of this thesis. Over a period of two years, microthermal measurements were made at the South Pole, both near the surface and from balloon-borne radiosondes, which provide direct measurements of the minute thermal fluctuations responsible for the seeing (Marks et al. 1996, 1999). In Chapter 2, the principles behind this experiment are described including the theoretical relationship between microthermal turbulence and the corresponding refractive index fluctuations, and the methods used to obtain the required microthermal data.

In Chapter 3, the results from the first stage of the experiment are presented, in which the optical turbulence fluctuations were measured over long periods by sensors mounted at three levels on a 27 m-high tower. These measurements provided an important insight into the behaviour of the boundary layer as a whole, and it was possible to discern some characteristic conditions for the occurrence of high and low seeing contributions, particularly in relation to the lowest part of the temperature inversion.

Chapter 4 covers the balloon launches, which carried sensors high into the stratosphere, and sent back data enabling vertical profiles of the turbulence to be calculated, as well as values for the total integrated seeing. The relative contributions from the boundary layer and free atmosphere were determined, and, once again, placed in the context of prevailing wind and temperature profiles throughout the atmosphere. Comparisons are made with similar measurements from other sites; in particular, with Cerro Paranal in the Atacama Desert, from whence data from a similar set of microthermal measurements are available.

In addition to the integrated seeing, the measurements made from the balloons

enable calculation of various parameters of importance to the application of adaptive optics. As mentioned already, a marked concentration of turbulence close to the surface should lead to a particularly favourable situation compared to other sites. The spatial and temporal characteristics of the measured optical turbulence at the South Pole are discussed in this context, with, again, some direct comparisons with similar data from other sites.

A major goal of the site-testing campaign is to determine the likely characteristics at other locations on the plateau. While the South Pole is very convenient, in the sense that it is the only station populated all year round, it is generally agreed that there are other sites where the astronomy conditions are potentially much better, in terms of atmospheric transmission, humidity and weather, as well as seeing. The South Pole lies some 1000 km away from Dome A, the highest point on the plateau at about 4300 m. Much of the boundary layer turbulence at the Pole is associated with the inversion winds which consist of cold air rolling gradually down the slope from the highest regions of the plateau, picking up speed as they go, before finally turning into the violent katabatic winds that are such a well-known feature of the weather along the Antarctic coastline. It is quite possible that the boundary layer seeing at Dome A is much lower than at the South Pole since, although the temperature inversion is still present, the calm winds close to the surface mean that the mechanical mixing of the different temperature layers is minimised.

There are other sites for which similar comments apply, and in Chapter 5, I compare some of the known precursors for optical turbulence at the South Pole (resulting from the microthermal measurements) with the relevant long-term weather data, obtained mainly from automated weather stations located at different places around the plateau (Keller et al. 1991, 1993, 1995). Potential candidate sites, apart from Dome A (which remains almost totally inaccessible, and for which no direct weather observations exist), include Vostok and Dome C (Fig. 1.1). Dome C has the further advantage that the infrastructure will soon be in place at this site to support a large observatory, with construction of the year round Franco-Italian *Concordia Station* now to be completed in 2005.

Obviously, direct measurements need to be made at these sites; however the sparse information available at this stage does allow some general comments to be made about the likely seeing conditions at the higher plateau sites, given the results from the South Pole.

# Chapter 2

## BACKGROUND

### 2.1 Theory

#### 2.1.1 Optical properties of atmospheric turbulence

The phenomenon of “seeing” refers to the blurring of long-exposure astronomical images due to distortion of the wavefront of the light from a source, as the light passes through the earth’s atmosphere. This distortion, arising from fluctuations in the refractive index of the atmosphere, causes the image to move around randomly in the focal plane. The refractive index variations are due to temperature (and, to a much lesser extent, humidity) fluctuations caused by turbulent mixing. Thus, in order to understand and quantify the study of astronomical image distortion, we must appeal to turbulence theory, many of the modern ideas of which follow the work of Kolmogorov in the 1940s (e.g. Kolmogorov 1941). In terms of its application to the study of astronomical image quality, the theory has been developed notably by Obukhov (1949), Tatarski (1961), Fried (1966), and Roddier (1981).

Kolmogorov supposes that turbulent energy begins in large-scale flows (typically, in the earth’s atmosphere, on the order of 10–100 m), which disperse into smaller and smaller cells, until a lower limit is reached (a few mm), at which point the energy is dissipated by viscous friction. Between these limits (the “inertial sub-range”), the turbulence is approximately locally isotropic, and the spectral power distribution of the turbulent cells is given by “Kolmogorov’s Law”:

$$\Phi_T(\kappa) \propto \kappa^{-11/3} \tag{2.1}$$

where  $\Phi_N(\boldsymbol{\kappa})$  is the power spectrum of the temperature fluctuations associated with the mechanical turbulence, and  $\boldsymbol{\kappa}$  is the three-dimensional wave vector.

We can define a structure function to describe the temperature fluctuations between two points separated by a distance  $|\boldsymbol{\rho}|$ , at altitude  $h$ :

$$D_T(\boldsymbol{\rho}, h) = \langle (T(\mathbf{r}, h) - T(\mathbf{r} + \boldsymbol{\rho}, h))^2 \rangle \quad (2.2)$$

which can be written in terms of a structure constant modified by the distance scale (Obukhov 1949):

$$D_T(\boldsymbol{\rho}, h) = C_T^2(h) \rho^{2/3}, \quad (2.3)$$

Similar relations apply for the corresponding refractive index fluctuations. The analogous refractive index structure constant  $C_N^2(h)$ , is related to  $C_T^2(h)$  using Gladstone's relation (e.g. Roddier 1981):

$$C_N^2(h) = \left( 80 \cdot 10^{-6} \frac{P(h)}{T(h)^2} \right)^2 \rho^{-2/3} D_T(\boldsymbol{\rho}, h). \quad (2.4)$$

where  $P$  is the pressure in hPa and  $T$  the temperature in Kelvin. Humidity effects are negligible for astronomy applications (Coulman 1985). This equation is the link between directly measurable microthermal fluctuations and the corresponding effects on image quality.

Microthermal turbulence generally occurs in many layers at different altitudes. So in order to quantify the overall effect it is necessary to integrate  $C_N^2$  over the whole atmosphere. There are a few commonly used measures of image quality, with probably the most universal being the ‘‘Fried parameter’’ (Fried 1966),  $r_0$ , which is defined as the diameter of a telescope for which the effect on image quality due to atmospheric turbulence is equal to the diffraction-limited resolution. For fully developed, locally isotropic turbulence following Kolmogorov's law,  $r_0$  may be written as

$$r_0 = \left( 0.423 k^2 \sec \gamma \int_{h_0}^{\infty} C_N^2(h) dh \right)^{-3/5} \quad (2.5)$$

where  $k$  is the wave number and  $\gamma$  is the zenith angle and  $h_0$  represents the height of the telescope.

This analysis may also be used to determine the size of the full-width half-

maximum seeing disc,  $\varepsilon_{\text{fwhm}}$ . For a telescope of aperture diameter  $D \gg r_0$  looking through the atmosphere, the image resolution is reduced from  $1.27(\lambda/D)$  (the width of the Airy disk) to  $0.98(\lambda/r_0)$  (Roddir 1981, Dierickx 1992), and hence:

$$\varepsilon_{\text{fwhm}} = 5.25\lambda^{-1/5} \left( \int_{h_0}^{\infty} C_N^2 dh \right)^{3/5} \quad (2.6)$$

One important implication of this equation is that the contributions to the seeing, in terms of  $\varepsilon_{\text{fwhm}}$ , from individual turbulent layers in the atmosphere do not add linearly, but rather

$$\varepsilon_{\text{total}}^{5/3} = \sum_i \varepsilon_i^{5/3}. \quad (2.7)$$

In the visible range,  $r_0$  is typical of the order of 10 cm or so at an average ground-based site, while in terms of the image full-width half-maximum, the criterion for good seeing is considered to be  $\varepsilon_{\text{fwhm}} \lesssim 1''$ . The result improves somewhat at longer wavelengths, since

$$r_0 \propto (\lambda^{-2})^{-3/5} = \lambda^{6/5} \quad (2.8)$$

and hence

$$\varepsilon_{\text{fwhm}} \propto \lambda^{-1/5} \quad (2.9)$$

In order to compare results from different sites, therefore, it is necessary to quote values of  $r_0$  and  $\varepsilon_{\text{fwhm}}$  at the same wavelength at each site. The informal standard is  $\lambda = 0.5\mu\text{m}$ , and this is the wavelength for which all values will be calculated here, unless otherwise noted. Some values are also given at  $2.4\mu\text{m}$ , since this is a particularly important wavelength in the context of infrared astronomy in Antarctica.

### 2.1.2 Turbulent layers in the atmosphere

In terms of a given telescope and site, the most important single parameter describing the effect of the atmosphere on image quality is the integral  $\int C_N^2(h)dh$  taken over either the entire atmosphere, or the individual layers causing the image distortion. There exist many methods for making measurements of the total seeing. Direct analysis of telescope images can of course be used where there is

already in place a telescope of large enough aperture diameter to be seeing limited. Other methods include direct or differential image motion monitors (e.g. Persson et al. 1990, Sarazin 1986), which measure the extremely rapid fluctuations in image position, and interferometric seeing monitors (Nightingale & Butcher 1991), which analyse the distorted wavefront.

These kinds of experiments, however, generally convey little information about the vertical structure of the atmospheric turbulence. Such data is of great importance from the point of view of selecting a site in the first place, placing a telescope at the optimal location at a site (considering the local topography), minimising the seeing contribution from thermal disturbances caused by the telescope and/or dome itself, and analysing the feasibility of image correction techniques (adaptive optics).

The thermal turbulence causing image degradation is often separated into four categories (Roddier 1981, Vernin & Tuñon-Muñoz 1992): seeing arising from (a) the telescope, dome, and local environment, (b) the surface layer, up to a height of a few tens of metres, (c) the planetary boundary layer, usually encompassing the first 1–2 km, and (d) the free atmosphere. Localised turbulence in and around the telescope tube is an often under-estimated source of seeing. It arises from temperature and wind velocity gradients between the telescope environment and the outside air and is, therefore, to some extent controllable.

In general, most of the seeing, for a well-designed telescope and enclosure, is due to natural turbulence. While the general structure of the atmosphere, in terms of temperature and wind characteristics, has been known for a long time, it was not until about the 1960s that the main regions of turbulence began to be identified, leading to the broad classifications outlined above.

The first realistic model for the  $C_N^2$  profile of the atmosphere (Fig. 2.1) was produced by Hufnagel (1964). This profile, based on the limited amount of atmospheric data available at that time, assumes a fairly smooth decrease in  $C_N^2$  from ground level up to the top of the planetary boundary layer, at 1–2 km. A minimum is reached in the troposphere in the region from 4–8 km, with a secondary peak in the tropopause (around 10 km). Beyond that, the optical turbulence is so weak as to be almost negligible. Hufnagel's models were useful at the time, since they provided a basis for approximate calculations of the seeing via Eq. 2.6, using available atmosphere data.

The relative contributions of the major sources of seeing have been studied since

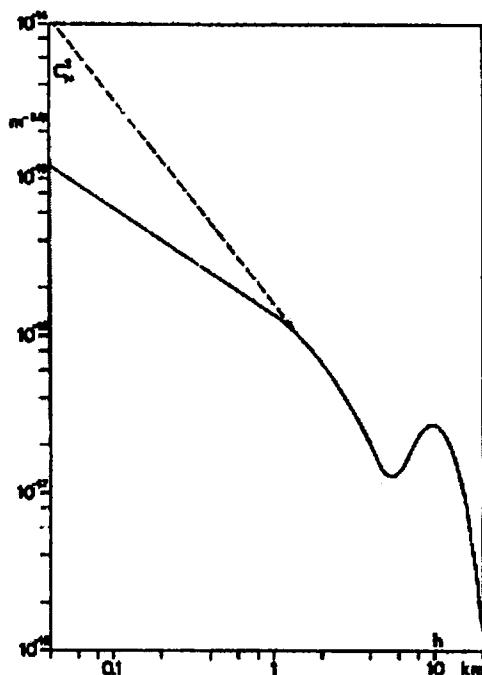


**Figure 2.1:** *Early theoretical model of  $C_N^2$  intensity through the entire atmosphere (Hufnagel & Stanley 1964), figure reproduced from Roddier (1981). The profile decreases smoothly to a minimum at around 5 km, before rising to a secondary maximum near the tropopause*

around the late-1960s and '70s, generally in the context of testing new sites. One of the most common methods, advantageous due to its ability to sample all layers of the atmosphere, is the use of microthermal probes. This method forms the basis of the research described in this thesis, and is described in more detail in Sect. 2.2. The approach is to make measurements of  $D_T$ , and calculate  $C_N^2$ , and hence the seeing, via Eqs. 2.2–2.6.

### 2.1.3 Adaptive optics

The turbulence structure of the atmosphere also has implications for the feasibility of image correction techniques such as adaptive optics and speckle interferometry. In particular, the isoplanatic angle and wavefront coherence time — the main spatial and temporal parameters limiting any image correction system — are highly dependent on the altitude of the strongest turbulent layers, and can be

calculated from the known  $C_N^2$  profiles at a given site (e.g. Vernin & Tuñon-Muñoz 1994, Fuchs 1995). A turbulence profile showing a higher proportion of boundary layer turbulence, with a relatively clear free atmosphere, will be much more tractable for a low-order adaptive optics system than one with, for example, strong jet stream-related turbulence in the tropopause. Most of the new generation of large telescopes are utilising some form of image correction of this type, and so the vertical profile becomes even more important with these considerations in mind.

The potential for adaptive optics at the South Pole and other sites on the plateau is discussed in detail in Chapter 4, in light of the parameters calculated from the measured  $C_N^2$  values.

## 2.2 Microthermal measurement of seeing

### 2.2.1 Earlier results

The use of microthermal sensors is a commonly used technique, and very versatile in that sensors may be used to examine a particular turbulent layer in great detail, or provide a measurement of the total integrated seeing, as part of a balloon-borne radiosonde. The first successful experiments using this method date back to the early 1970s (Coulman 1973, Bufton 1973, Barletti et al. 1976). Examples of the  $C_N^2$  profiles measured by some of these early experiments are shown in Fig. 2.2. Taken at a range of sites, the results show the common characteristics of well-defined turbulent zones at various levels in the atmosphere, as well as sharp peaks due to narrow turbulent layers of no more than a few tens of metres in depth. Almost all data show a relatively strong layer of turbulence at an altitude of around 9-12 km, at the level of the tropopause. In this region, the temperature gradient flattens out, and inversions can occur which, combined with the sometimes strong jet-stream winds, leads to turbulent instability (Coulman 1985). Boundary layer effects were highly variable from site to site, although turbulence in the first few tens of metres above the surface is generally not measurable with this method, since it takes at least ten seconds for balloon-borne sensors to stabilise, which corresponds to a height of 30–40 m.

In more recent years, with the advent of 8 m-class telescopes, microthermal measurements have become an integral component of comprehensive site-testing campaigns in the Canary Islands (Nightingale & Butcher 1991, Vernin & Tuñon-

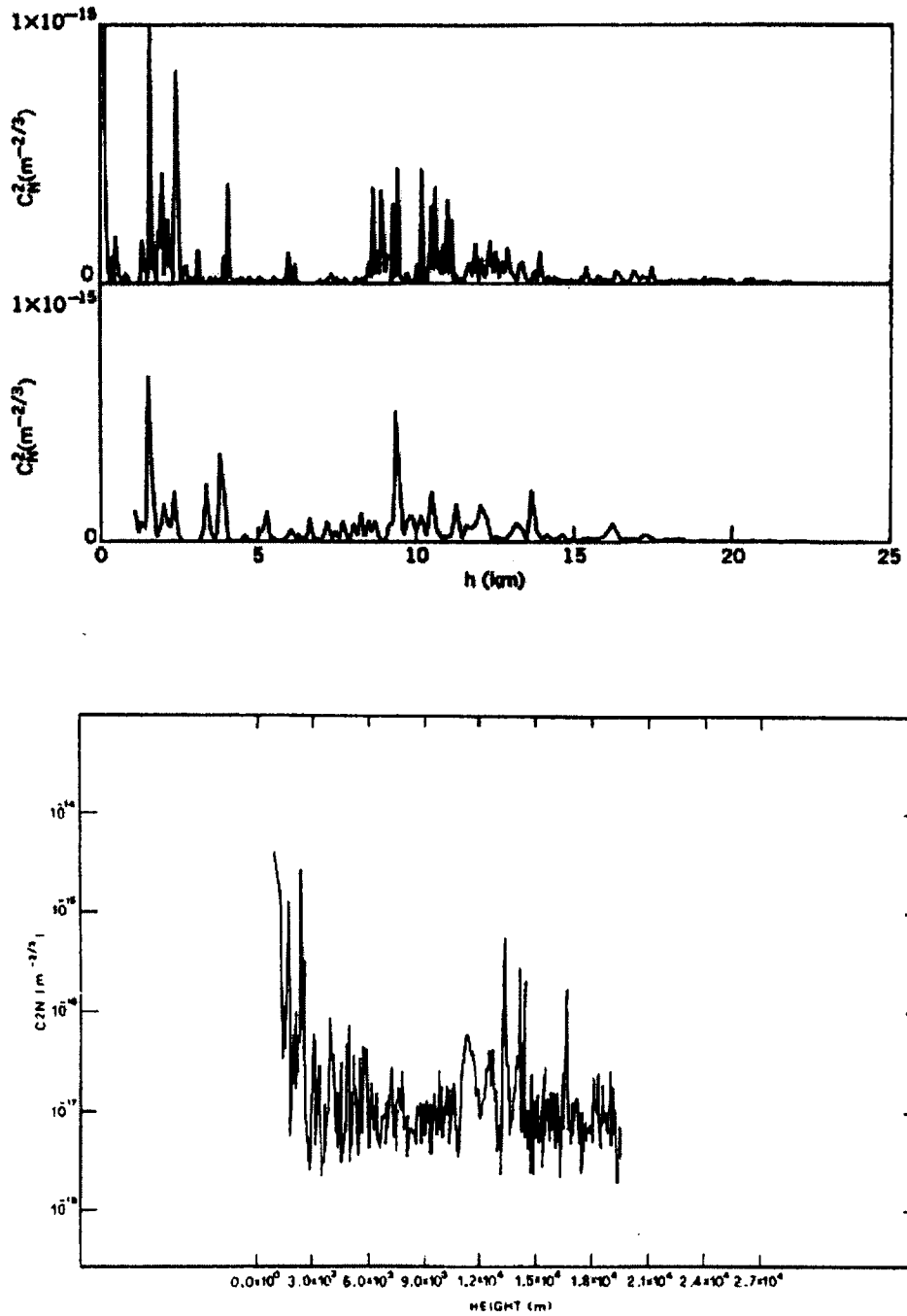


Figure 2.2: Examples of  $C_N^2$  profiles obtained from two early balloon-borne microthermal radiosondes; a) from Bufton (1973) and b) from Barletti et al. (1976). Both profiles contain pronounced elevations in optical turbulence associated with the tropopause, in agreement with Hufnagel's model. The two plots for Bufton's data are for both ascent (top) and descent (bottom).

Muñoz 1992, Vernin & Tuñon-Muñoz 1994), Mauna Kea in Hawaii (Roddiier et al. 1990) and in Chile at La Silla (ESO-VLT working group 1987) and Cerro Paranal (Fuchs 1995). While each of these sites enjoys sub-arcsecond seeing on average, the turbulence profiles are quite different. The Chilean sites, in particular, tend to have a high proportion of the seeing caused by turbulence in a boundary layer extending up to about 1–2000 m, with a relatively quiescent tropopause. This is in marked contrast to Mauna Kea, which at 4200 m is high enough to avoid boundary layer effects almost completely (Bely 1987). Here, however, an upper level jet stream greatly increases the high-altitude component of the seeing, so that, overall, the site quality is no better than the high desert sites in Chile. Some of the characteristics of these sites are discussed in more detail in Chapter 4, in comparison with the results from the South Pole.

Surface effects have been studied as well, by placing microthermal sensors on tall masts and towers. Atmospheric effects this close to the surface have been found to be very small at night (ESO-VLT working group 1987, Vernin & Tuñon-Muñoz 1992), with generally no more than 10% of the total seeing generated by the lowest 20–30 m or so. During the daytime, however, ground heating can produce stronger temperature gradients near the surface, and hence increased turbulence (Coulman 1985). The results of some of these experiments are compared with the South Pole measurements in Chapter 3.

### 2.2.2 Microthermal sensors

The microthermal fluctuations responsible for optical seeing may be measured by pairs of sensitive temperature sensors separated by a distance  $\rho$ , according to Eq. 2.2, with  $\rho$  between the inner and outer scales for the turbulence. Typically,  $\rho$  is chosen to be around 30–100 cm.

The temperature fluctuations to be measured have magnitudes on the order of 0.01°C, varying on a timescale of 10–100 Hz. Clearly, the sensors required to fulfil these criteria must be extremely fine, and have very low thermal inertia. The sensors used in both seasons of the the South Pole campaign, along with the electronics and other necessary hardware, were developed at the Université de Nice, and are essentially the same as those used by this group at other sites over the past couple of decades; most notably and recently at La Palma (Vernin & Tuñon-Muñoz 1992), La Silla (ESO-VLT working group 1987) and Cerro Paranal (Fuchs 1995).

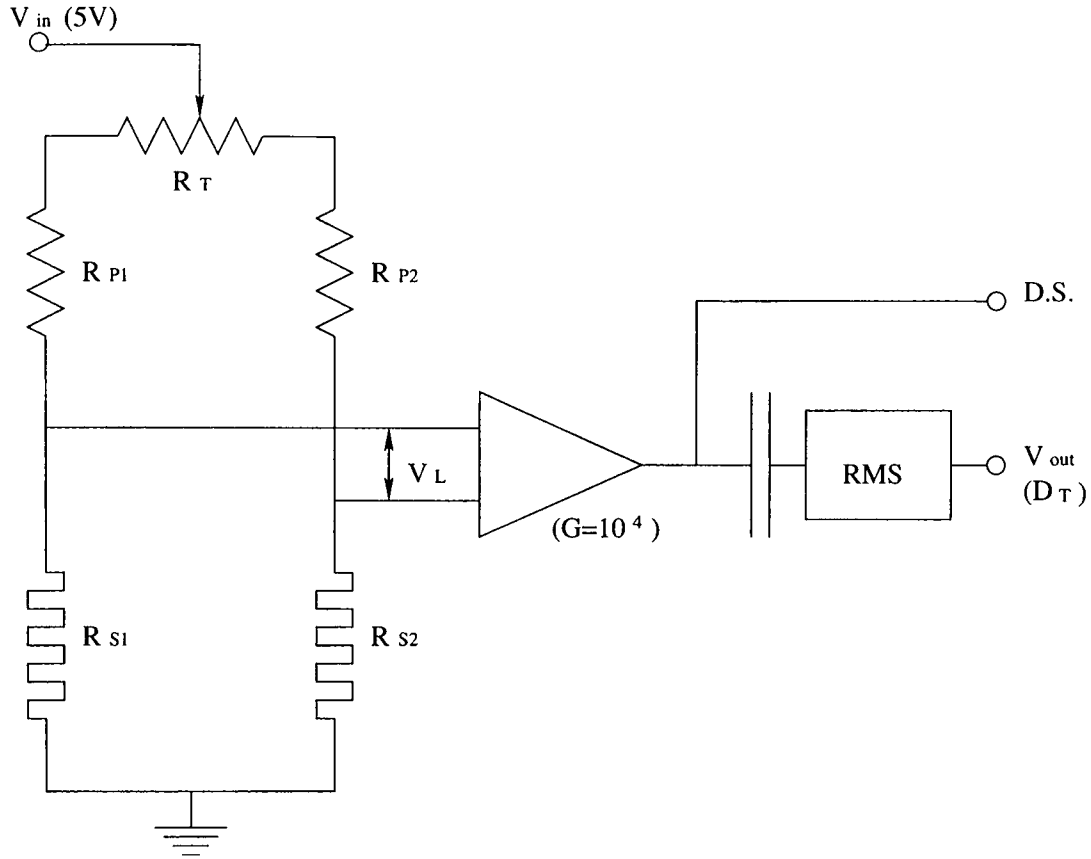


**Figure 2.3:** Simplified schematic of the  $D_T$  sensor circuitry. Microthermal fluctuations cause variations in the resistance of the sensors ( $R_{S1,S2}$ ), which create a small differential voltage  $V_L$  at the amplifier input. The RMS output ( $V_{out}$  gives  $D_T$  via Eqs. 2.11 and 2.2). The direct signal (D.S.) is also measured for calibration purposes.

The sensors consist of extremely fine tungsten filaments, supported on the struts of small light globes from which the regular light filament has been removed. This provides a robust support structure for the sensors, as well as a convenient means of connecting them electrically.

The circuit used to measure  $\Delta T$  between the two sensors is quite simple, consisting of a Wheatstone bridge with the microthermal resistors connected to a differential amplifier, as in Fig. 2.3. The amplified voltage signals pass through an RMS filter, as required by Eq. 2.2. Once the relationship between  $\Delta T$  and  $\Delta V_L$  is known, this output leads directly to the structure function,  $D_T$ .

The tiny differential voltage fluctuations measured at the input to the amplifier

arise from variations in the resistance of the sensors, which vary linearly with temperature:

$$R_{S,T} = R_{S,20} [1 + \alpha (T + 20)] \quad (2.10)$$

where  $T$  is the temperature in Celsius,  $20^\circ\text{C}$  being the temperature used to standardise the resistances, and  $\alpha$  is the temperature coefficient for the sensors.

Assuming that the sensors themselves are the only components whose resistance varies rapidly enough in response to environmental microthermal fluctuations to be measurable, then we can use Eq. 2.10 in combination with the standard bridge equation to give:

$$\Delta T / \Delta V_L = \frac{(R_P + R_T)_{av}}{V_{in} \alpha R_{S,20av}} \left[ 1 + \frac{(R_{S,T} + R_C)_{av}}{(R_P + R_T)_{av}} \right]^2 \quad (2.11)$$

where  $V_L$  is simply  $V_{out}$  divided by the amplifier gain.  $R_C$  is the resistance of the cable, and all other quantities are as labelled in the figure. The subscript ‘‘av’’ refers to the average value of the labeled resistance in each branch of the circuit.

For this technique to be accurate, the resistances of all sensors must therefore be measured accurately at room temperature before deployment. In the case of the mast experiment, this must include each of the  $\sim 100$  m-long cables connecting the sensors to the electronics boxes back in the laboratory. Before taking data, each pair of sensors must then be carefully equilibrated. The procedure differs slightly for the mast and balloon experiments, and is described in more detail for each case in Chapters 3 and 4. Essentially, it is necessary to measure the offset voltage of the amplifier, which becomes the base level for the turbulence-induced fluctuations. All sensors and cables are then connected and, in the absence of turbulence, the trim pot  $R_T$  is adjusted so that  $V_{out} = V_{off}$  at operating temperature. Accurate measurement requires that this equilibrium point remains stable throughout the duration of a data run. This does not present a problem for the balloon sondes, where the additional wiring is minimised. It was expected, however, that slight temperature difference between the long cables running out to the tower would require re-equilibration from time to time due to drifts in the input balance.

## Chapter 3

# SURFACE LAYER SEEING

Our site-testing campaign began at the Amundsen-Scott South Pole Station in the austral summer of 1993/94, during which we set up an experiment designed to measure the seeing generated by optical turbulence in the lowest few tens of metres of the atmosphere, using sensors sensitive to extremely small and rapid temperature fluctuations. Given the likelihood that a large proportion of the seeing at this site is caused by boundary layer turbulence associated with the temperature gradient and inversion winds close to the surface, it was considered a very important first step to perform a detailed study of the intensity of the turbulence in this region, and its variability over time.

By running this experiment throughout the year, we hoped to determine: a) the overall strength of the turbulence in the lowest 30 m or so of the atmosphere, and its relationship to the intensity of the temperature inversion, b) an indication of the types of weather conditions corresponding to good seeing (low turbulence) measurements, and the frequency of these conditions, and c) more detailed factors, such as the rate and intensity of short timescale fluctuations, which may be of interest from the point of view of image correction (adaptive optics).

A secondary consideration was the desire to test our equipment in the field, in particular the sensors and electronics, in a setting where they could be monitored and, if necessary, repaired relatively easily by the responsible winter-over technician. The information thus obtained was expected to be useful from the point of view of maximising the likelihood of success of the more technically demanding balloon-borne instruments during the following season (see Chapter 4).

The experiment ran right through the 1994 winter, providing over 100 hours

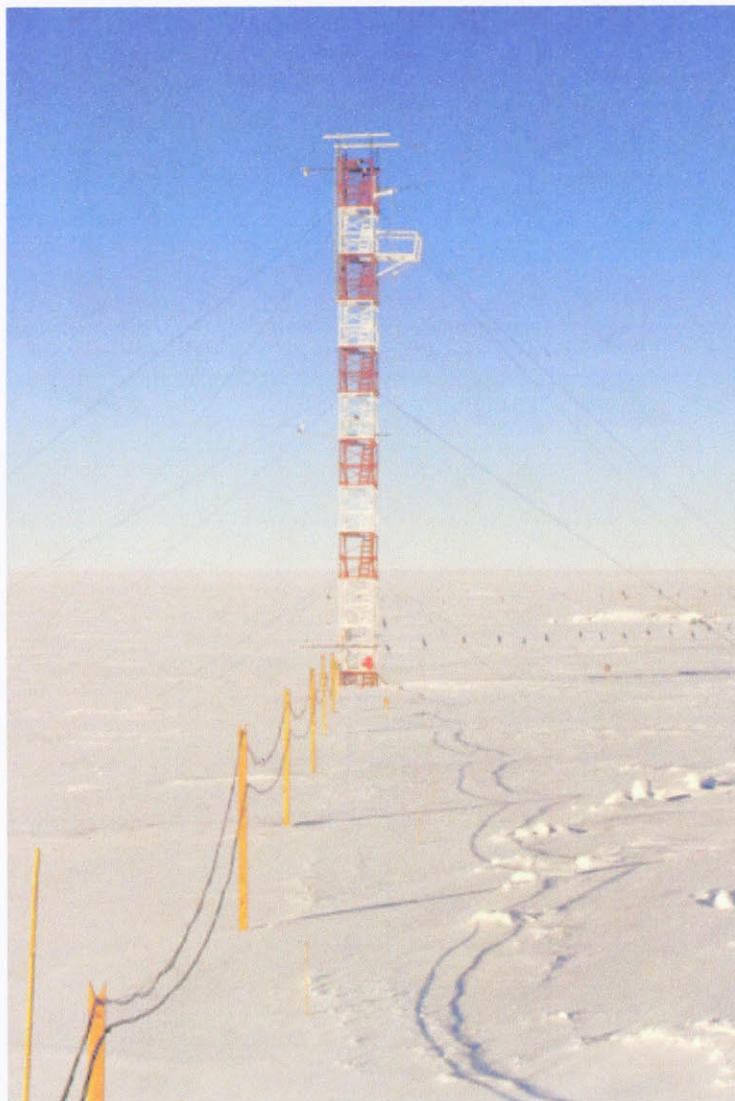


**Figure 3.1:** *The National Oceanic and Atmospheric Administration (NOAA) tower.*

of data in all weather conditions. Enough information was obtained to perceive the different characteristic conditions that occur, and to estimate the prevalence of low optical turbulence conditions close to the surface. The height of the sensors (a maximum of 27 m) turned out to be sufficient to discern the upper limit of the lowest turbulent layer much of the time.

## 3.1 Procedure

### 3.1.1 Hardware

Two pairs of microthermal sensors were placed at each of three levels on the National Oceanic and Atmospheric Administration (NOAA) tower (Fig. 3.1), as shown in Fig. 3.2. This tower is located in the “Clean Air” sector on the up-wind side of the Station. The prevailing surface winds at the South Pole are from the north-east quadrant (i.e. between grid  $0^\circ$  and grid  $90^\circ$ ), with a very high directional constancy, due to the combined effect of the inversion wind, the geostrophic winds (from the general direction of grid  $0^\circ$ ), the coriolis effect and friction forces due to the surface structure (Fig. 5.3), as described by Schwerdtfeger (1984). This is the best location on station for the measurements of atmospheric aerosols conducted on the tower by NOAA, since it minimises the effect of heat and pollution generated by the station itself. For the same reason, it is ideally located for microthermal measurements of lower-boundary layer turbulence.

As shown in the figure, the sensors are positioned at 7, 17 and 27 m. The height of the lowest sensor was chosen to avoid the worst of the blowing snow near the surface, which could potentially damage the sensors during high wind conditions. In any case, it is also probably as close to the surface as the aperture of any medium to large optical telescope would be located at the site, for the same reason. The top sensor was attached to a winch-driven extension, taking it to the highest possible point on the tower. The sampled region was therefore the lowest 20 m of the atmosphere above a hypothetical telescope 7 m above the surface.

The sensor supports each consisted of a 1.8 m-long beam, with a cross bar at the end about 1 m in length. The three main beams were fastened to the tower pointing horizontally in the direction of the prevailing wind, to minimise the effect of localised turbulence caused by the mast.

Two pairs of sensors were used at each level, one pair on each end of the one

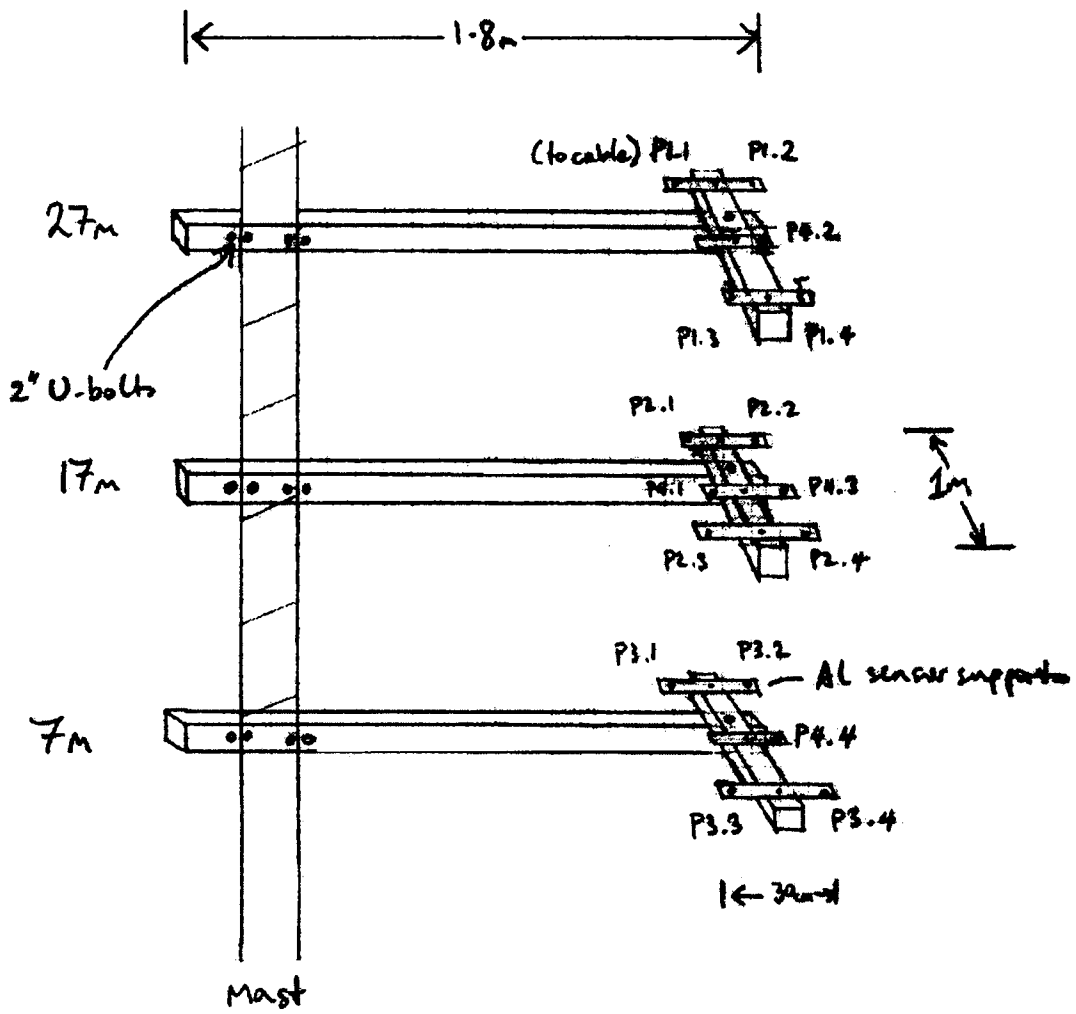


**Figure 3.2:** Arrangement of sensors on the 27m Met Tower. Two pairs of microthermal sensors were placed at each of the three levels, each oriented differently to minimise the risk of local turbulence effects. Two pairs of platinum sensors were also used to measure the vertical temperature gradient

meter cross bar, oriented at an angle of about  $45^\circ$  to each other. This offset angle was chosen to increase the accuracy of the sampling and, again, reduce the impact of local disturbances on the measured turbulence. A wide range of wind conditions can be covered in this arrangement, with at least one of the sensor pairs at the correct angle to measure “clean” turbulence. The sensor separation used was  $r_0 = 30$  cm; this distance puts the sampling well within the inertial sub-range for Kolmogorov turbulence.

Additional sensors were placed at each level to measure the temperature differences between levels, as well as the absolute temperature at the 17 m level. Four thermocouples were used for this purpose. Although these sensors do not have the same frequency response as the very fine microthermal sensors, they did respond rapidly enough to provide some interesting results on turbulent fluctuations on the 10 m scale.

We also had access to data from the NOAA instruments on the tower throughout the season, including temperature measurements at 2 m and 20 m, wind speed and direction, and atmospheric pressure. The extra temperature readings enabled calibration of our sensors (Sect. 3.1.3), as well as adding extra points to the sampling of the vertical temperature profile. Measurements of the atmospheric pressure were required to perform the  $C_T^2$  to  $C_N^2$  computations (see Eq. 2.4). Finally, the wind velocity is also important as it contains information about mixing of the different temperature layers, as well as helping in the identification of large scale weather features corresponding to particular seeing conditions.

The sensors on the tower were connected, via extreme-low-temperature rated ( $-75^\circ\text{C}$ ) teflon-shielded cables, to data acquisition and processing equipment located in the NOAA “Clean Air” building, about 100 m from the tower.

### 3.1.2 Software & data acquisition

The raw signal from the microthermal sensor pairs was sent to electronics boxes designed and built in-house at the Université de Nice. These boxes contain circuitry to carry out amplification and the required RMS computations, as described in Chapter 2. These boxes are essentially the same as those used for balloon-borne probes at other sites (such as Vernin & Tuñon-Muñoz 1994, Fuchs 1995), without the need for telemetry. In addition to the RMS-filtered “ $D_T$ ” channel for each sensor couple, we saved the direct signal, with a low-pass filter (0–0.3 Hz) used to

siphon off the DC component of the input (Fig. 2.3), and enable measurement of the amplifier offsets, as well as equilibration of the sensors at the beginning of each data run.

The amplified output from the sensors was sent to a PC via a 16-channel NIDAQ analog-digital converter. Control programs for this device were written to collect and process the raw data, and to specify the sampling frequency and averaging time, as well as to allow measurement of the amplifier bias, and offsets caused by the slightly different resistances of the sensors and cables within each pair as they responded to gradual changes in the ambient temperature. Since I would not be operating the experiment myself during the winter, it was necessary to write visually-based programs, to make the system as simple as possible for the operator. The control system that was developed displayed the output from all channels in real time, which enabled continuous monitoring the sensors for ice build-up during data-taking, and check for damaged or broken sensors.

Each output file contained the 16 channels of the A/D card, which included the RMS and direct signal for each of the six pairs of microthermal sensors, along with the temperature measured at the middle (17 m) level, and the upper and lower temperature differential (with respect to the central sensor). The sixteenth channel was reserved for a short circuit, to record the amplifier offset.

The offset voltage of each amplifier was measured by short-circuiting the inputs, and running the acquisition program, which gives a real time display of both the RMS-filtered and direct outputs. This allowed us to set the base level for the voltage fluctuations produced by the sensors, and to adjust the input levels with sensors in place, shielded from any turbulence.

The general aim was to allow the experiment to run more or less uninterrupted throughout the entire winter, shutting down only for occasional repairs or servicing. It quickly became evident that this plan was not achievable (see next section), and a strategy had to be developed for capturing the maximum amount of information from relatively short data runs. We ended up collecting two data sets for each run. The first, covering the entire duration of the run, included data from all sensor pairs, recorded every 1 s and integrated over 60 slices. The second file was a “snapshot” of the high-frequency turbulent fluctuations, containing raw data for a period of 30 min or so, at the maximum rate possible without interfering with the data flow (about 10–20 Hz). This method was chosen as a means of capturing information about the variations in intensity of the optical turbulence over both short (seconds)

and long (hours) time scales, while generating data files of a manageable size, given the restricted satellite bandwidth available.

Due to the very small and rapid resistance fluctuations being recorded in the experiment, it was critical to understand and minimise any sources of noise. These considerations were particularly important with 100 m or more of cable running from the control room in the Clean Air building out to the sensors on the tower, the resistance of which varied enough potentially to influence the results.

To determine the background noise level from all sources excluding the sensors themselves, the cables were short-circuited, and the output viewed using the display program. Once these values were reduced to a satisfactory level, by keeping the electronic boxes as far as possible from any sources of EM interference, and minimising the motion of the cables, they were recorded for reference during the data reduction process. Periodic checks were made to ensure that the noise levels were accurately known throughout the season. Despite the inherent difficulties, we were able to keep the combined effect of noise and equilibrium drift down to around 5–10 mV at the output, which corresponds to an error level of about 0.5% of the active signal level.

### 3.1.3 Data reduction

The first stage in the data reduction process was the removal of the amplifier offset, as recorded continuously in the unused data channel, and the background noise from each electronic box, previously measured by short-circuiting the cables.

The computation of  $D_T$  required the determination of the  $\Delta T/\Delta V$  ratio on output, from Eqs. 2.10–2.11, using the previously-recorded values for the resistances of the cables and sensors for each sensor couple, at both ambient and room temperature. The raw output (received as RMS voltages) was thus converted into temperature fluctuations for each pair of sensors. Knowing the amplifier gains and sensor separations, these values could then be used directly to calculate the temperature structure function,  $D_T$  and hence the structure constant,  $C_T^2$  via Eqs. 2.2–2.3.

In order to determine the corresponding refractive index parameter (Eq. 2.4), pressure and temperature values were required at each level. The pressure variation over a rise of 20 m is negligible for the purposes of this experiment, however the temperature gradients were sometimes very substantial, and these needed to be calculated in order to provide accurate values at each of the three levels. The read-

ings from the platinum sensors were used for this purpose. Since the experiment is designed for accurate measurement of temperature fluctuations and gradients, rather than baseline temperatures, it was necessary to calibrate the platinum sensors against the NOAA thermometers during conditions of near-zero temperature inversion, which occurred on around six occasions. These measurements enabled determination of the temperature at each level for all runs.

Armed now with  $C_N^2$  values from each of the three levels on the tower, it was then possible to measure the integrated seeing contribution from each of the 10 m-high slices, according to Eq. 2.6. The problem here is that there are only three data points with which to perform the integrations, and the vertical profile is clearly not linear much of the time, but rather, often decreases sharply with altitude. A power law variation with altitude was fit to the data over each ten-metre slice, of the same form as that used during the La Palma site-testing campaign (Vernin & Tuñon-Muñoz 1992) for  $C_N^2$  measurements over the lowest 21 m:

$$\int_{h_1}^{h_2} C_N^2 dh = h_2 C_N^2 \left[ \left( \frac{h_2}{h_1} \right)^{a+1} - 1 \right] / (a + 1) \quad (3.1)$$

where

$$a = (\log C_N^2(h_2) - \log C_N^2(h_1)) / \log \frac{h_1}{h_2} \quad (3.2)$$

This function applies a more steeply climbing curve as the difference between the  $\int C_N^2$  values for each ten-metre slice increases over the height of the mast (and vice versa), and reduces to linearity for a smooth variation. The departure from linear integration was only significant for very steeply varying  $C_N^2$  profiles, and it is estimated that the formula supplies the correct integrated values within an uncertainty range of a few percent.

## 3.2 Results

The software for the experiment was written, tested, and fully debugged with all necessary instrumentation in Sydney, before the experiment was successfully deployed on the NOAA ‘‘Clean Air’’ tower during Jan.-Feb. 1994, by our winter-over scientist (John Briggs), with assistance from other members of CARA and JACARA. All necessary tests and measurements of offsets, noise limits and sensor

and cable resistances were made during this period, and several test runs performed to confirm the successful operation of the control and data acquisition software.

These parameters were checked again during April, before the first science data were taken: a 3 hour run on April 22. It became apparent even during these early runs that the sensitivity of the sensors diminished after a couple of hours, with a corresponding drift in equilibrium. A check of the sensors at the end of the first run revealed a substantial build-up of ice crystals on the filaments. Throughout the season, this effect appeared to be more severe on the lower levels than near the top of the mast, and a few sensors were broken due to the weight of the ice.

As mentioned previously, it had originally been envisaged that the experiment would be left running continuously for days at a time, with only occasional pauses to check the equilibrium of the amplifiers. Clearly, the results of the first few runs meant that the duration of the data runs would be very limited, and that they would need to be closely supervised by the winter-over technician, in order to ensure that the maximum amount of valid data was obtained, and to minimise the risk of damage to the sensors caused by the weight of the ice on the extremely delicate filaments.

Covers were made in order to avoid damage to the sensors *between* runs, and a switchable heating circuit was set up to keep them free of ice when not in use. This arrangement required that the winter-over scientist climb the mast at the start and end of each data run to remove the covers; however, it did enable the experiment to continue for the whole season. As it turned out, the rate of ice formation on the filaments was highly variable, and there were several occasions where data runs of 8–10 hrs or more were possible. Conversely, at other times, the effect of ice on the data was noticeable after less than 1 hr. Although several sensors were broken, there were enough spares available to maintain the full complement at each level.

### 3.2.1 Summary

Microthermal data from the mast were taken on a total of 49 occasions during the 1994 winter, between April 26 and August 10. The duration of the runs varied from 1 to 14 hrs, depending on the condition of the sensors. The “icing” problem occurred during approximately half of these runs, and the data were examined closely to determine the point at which the ice began to have an effect, with all suspect data deleted before any further processing.

Height range	$\epsilon$ (arcsec)				
	mean	median	$\sigma$	best	worst
lower (7–17m)	0.46	0.42	0.29	0.04	1.01
upper (17–27m)	0.37	0.31	0.27	0.02	0.91
total (7–27m)	0.64	0.59	0.40	0.13	1.44

**Table 3.1:** Turbulence contributions to surface layer seeing (7–27m), for separate and combined levels, measured on the NOAA mast over 49 data runs between 26 April and 10 August 1994. Note that the seeing contributions from the two ten-metre “slices” do not add linearly (Eq. 2.7)

The data runs took place under a wide variety of weather conditions, in terms of wind, cloud cover, temperature, and inversion strength. This provided a good overall picture of the relationship between the optical turbulence observed and the larger scale atmospheric conditions prevailing at the time.

The mean seeing values for total and combined levels were obtained simply by combining the  $C_N^2$  data sets in their entirety, and averaging over the full set. Only the first hour of integrated data from each run was used for this purpose, to avoid a bias towards the weather conditions where longer data runs were possible. Since the weather conditions, and hence the seeing, sometimes varied appreciably over the course of some of the longer runs, two one hour samples were taken from some of these runs, separated by 10–12 hr, and used in the statistics as two distinct runs. This was done in order to utilise as much data as possible in the analysis. Hence, the mean values calculated represent the average over a total of 53 hrs, spread more or less randomly throughout the period.

The results are summarised in Table 3.1. The integrated seeing contribution from 7–27 m was 0.64", with measured values ranging from 0.13" to >1.4" (an enormously strong disturbance for a 20 m slice of the atmosphere) over the full vertical range. This total value was not evenly distributed, but instead the optical turbulence in the lower 10 m section was significantly stronger, with an average value around 0.1" higher than the upper layer, as shown in the table. The lower section alone produced around 1" on a few occasions. Fig. 3.3(a,b) shows the probability and cumulative distributions for the entire season's data, for both separate and combined levels.

The temperature inversion over the height of the mast also varied widely, and was often surprisingly large, ranging from 0–10°C between 7 and 27 m. No signifi-

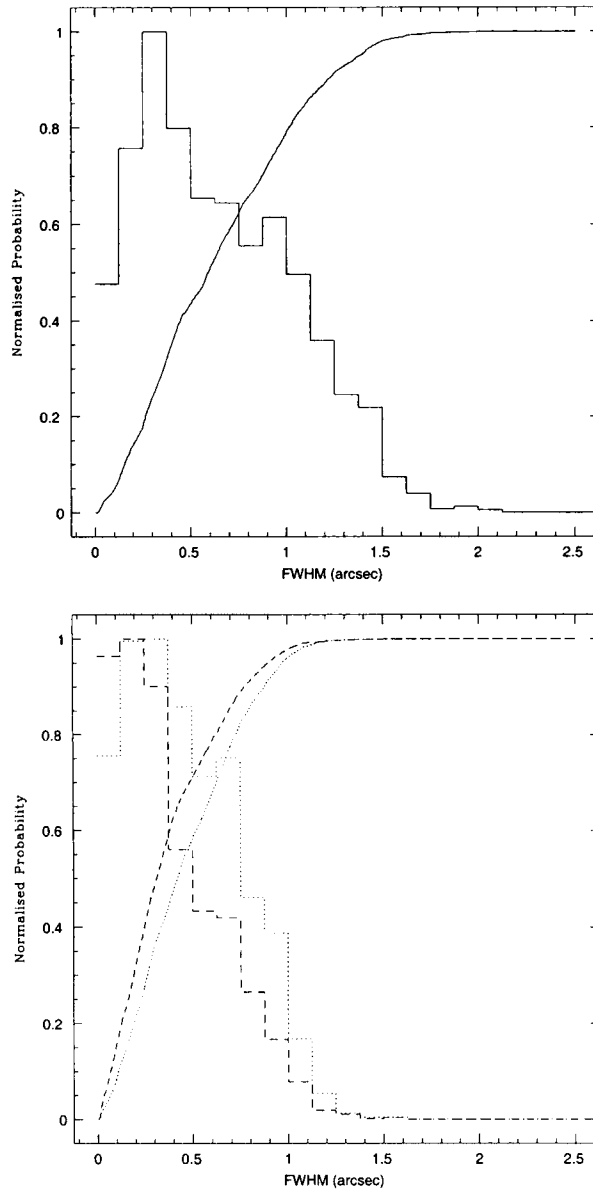


**Figure 3.3:** Seeing data statistics: full-width half-maximum probability distribution and associated cumulative distribution for a) combined levels (i.e., 7–27m), b) the two separate levels, 7–17m (dotted line) and 17–27m (dashed line).

cant positive temperature gradients were recorded. The temperature gradient was also frequently highly uneven over the height of the mast, with a stranger gradient in the lower level.

The wind direction was almost invariably from the quadrant facing towards the highest regions of the plateau (i.e. between approximately grid  $0^\circ$  and  $90^\circ$ ). This was the situation anticipated when the placement and orientation of the sensors was chosen at the beginning of the season, and as a result the two sensor couples at each level each received very “clean” turbulence, with minimal disturbance from the mast, sensor supports, or any other obstacles. The correlation function for the  $C_N^2$  readings from the two pairs at each level was computed for each run, and a cross-correlation of  $C > 0.9$  was obtained in almost every case, confirming that virtually all of our signal was produced by natural turbulence.

In addition, the high-frequency turbulent fluctuations (as opposed to the filtered average data) were quite often highly correlated as well, indicating that, much of the time, the individual turbulent cells producing the signal in the sensors must have been at least as large as the distance between the two sensor pairs: about 2 m. In fact, the fluctuations in the output from the pairs of temperature sensors (separated by 10 m in the vertical plane) were also, to varying degrees, often correlated with the turbulence measurements, showing that the outer scale,  $L_0$ , and large-scale structure of the turbulence vary quite substantially in different conditions, with much of the  $C_N^2$  signal often being produced by single large, intense cells. This result has particular implications for the feasibility of adaptive optics, and some examples are given in the next section.

### 3.2.2 Characteristics of individual measurements

The temperature and turbulence structure observed at different times varied markedly, sometimes changing significantly within the course of a run. The great difference in  $C_N^2$  readings from the three levels was a feature of the  $C_N^2$  profiles in the vast majority of runs where a significant seeing contribution was measured. On a few occasions, the seeing integrated over the lower level was greater than the upper level by as much as a factor of five.

Two illustrations of the wide variability of conditions observed are shown in Fig. 3.4. In the first example Fig. 3.4(a), almost identical microthermal variations were seen at each of the three levels. The seeing contribution integrated over

the height of the mast was  $\varepsilon = 0.53''$ , which is around average. The weather was hazy with some blowing snow, and the temperature inversion was very weak:  $\Delta T < 0.5^\circ\text{C}$ . With a rather strong breeze of  $9 \text{ ms}^{-1}$  at the surface, as well, one might expect relative stability near the surface on a day like this. This is not the case, with a significant amount of optical turbulence observed evenly distributed over the height of the mast, even in the absence of a vertical temperature gradient.

The second example (Fig. 3.4(b)) illustrates conditions tending to the opposite extreme, where the  $C_N^2$  values decreased by two orders of magnitude from 7 to 27 m. The average integrated seeing values for this run were  $0.117''$  (7–17 m) and  $0.019''$  (17–27 m). Weather conditions were very clear, and the temperature inversion during this run was relatively large,  $\sim 4^\circ\text{C}$ . Apparently, the lowest turbulent layer extends to a height of only  $\sim 20$  m on this particular occasion, and it is interesting to note how clearly our array of sensors resolves the upper limit of this layer.

These two examples illustrate the highly variable nature of both the turbulence structure and intensity, and the profile of the temperature inversion near the surface at the South Pole, and hence the importance of this region to the overall seeing. The results from all data runs were examined in detail, in an effort to relate the  $C_N^2$  measurements to other atmospheric parameters, and gain some understanding of the strength and structure of the optical turbulence in different types of weather conditions.

As with most other sites, it is very difficult to deduce any general relationships between the seeing and large scale meteorological parameters of sufficient accuracy to use as a predictive tool, or to make sweeping statements about the turbulence properties of the lower boundary layer. Nevertheless, several characteristic types of conditions were observed, which are interesting to analyse. In order to simplify the study, the data were placed into four categories, with characteristic  $C_N^2$  and  $\Delta T$  profiles summarised in Table 3.2. The classification of the seeing on a given day is not quite as clear-cut as the table perhaps suggests, and often the readings would change from one characteristic signal to another over the course of a few hours. They do show, though, that there is some inter-relation of the wind and temperature parameters in terms of their effect on the seeing, and, perhaps in the future, further observations of these phenomena might lead to a firm understanding of the mechanisms that generate optical turbulence in different conditions.

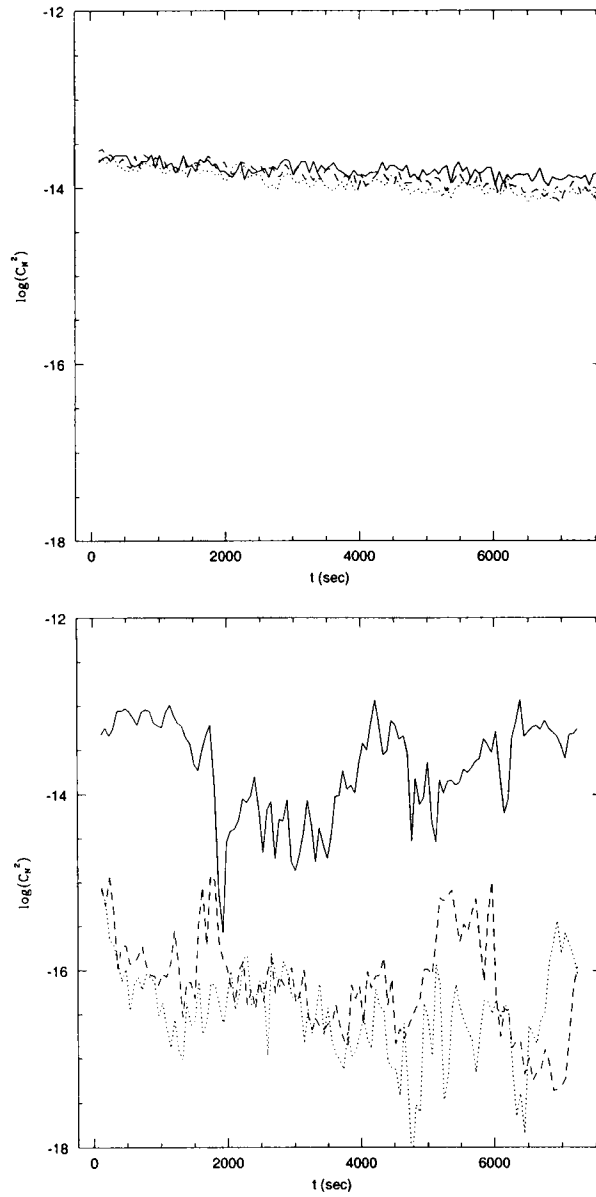


**Figure 3.4:**  $C_N^2$  vs. time: a) for 23/05/94, b) for 20/05/94. Solid lines represent the 7m level, long dashes the 17m level and short dashes the 27m level.

	$\varepsilon$	$\Delta T(^{\circ}\text{C})$	Comments	Fraction of Data
(i)	$\varepsilon > \bar{\varepsilon}$	$1 < \Delta T_{1,2} < 2$	Average to poor seeing. Can occur in all types of weather. $\varepsilon_1/\varepsilon_2 \sim \Delta T_1/\Delta T_2$	40%
(ii)	$\varepsilon \ll \bar{\varepsilon}, \varepsilon_1 \simeq \varepsilon_2$	$\Delta T < 0.5$	Very good seeing. Usually occurs during bad weather.	20%
(iii)	$\varepsilon_1 < \varepsilon_2$	$\Delta T_1 \ll \Delta T_2$	Generally good weather, large uneven inversion. Good seeing above $\sim 17\text{m}$ .	20%
(iv)	$\varepsilon_1 < \varepsilon_2$	$\Delta T_1 > \Delta T_2$	$\varepsilon_1/\varepsilon_2 < \Delta T_1/\Delta T_2$ . Good weather, large, uneven inversion, temp. gradient increasing with height. Good seeing, esp. above $\sim 17\text{m}$ .	10%

**Table 3.2:** The four characteristic types of data observed from the mast. The subscripts 1 and 2 refer to the upper (17–27m) and lower (7–17m) levels respectively.  $\bar{\varepsilon}$  is the mean value of the seeing.

### Case (i):

The first case includes the majority of runs where worse than average seeing was measured ( $\varepsilon > 0.6''$  or so). An example is shown in Fig. 3.5(a). The temperature inversion is moderate and fairly consistent over the height of the mast. The most interesting feature of these observations was the fact that there was a high correlation between the relative seeing contributions from each 10 m slice and the ratio of the two sections of the temperature inversion, as alluded to earlier. In fact, the  $C_N^2$  outputs were frequently highly correlated with the fluctuations measured from the temperature sensors on a short time scale as well, and calculation of the integrated seeing contribution using the magnitude of the temperature variations (7–17 m and 17–27 m) was very close to the same as the result from the microthermal sensors.

This is a very interesting observation since, first of all, it shows that the outer

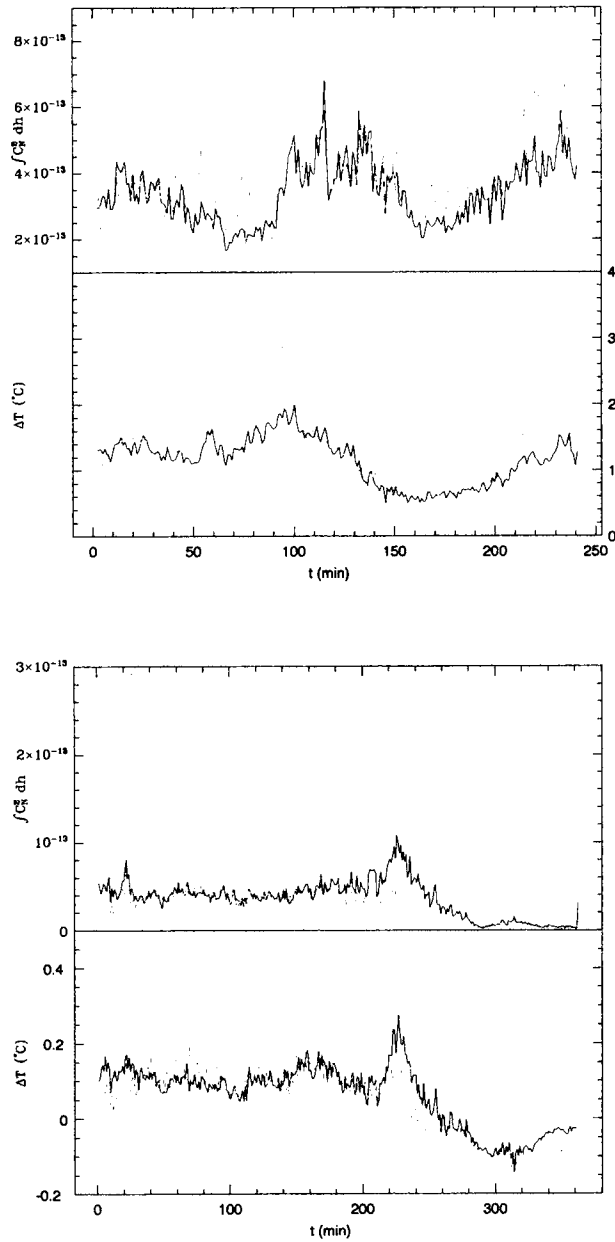


Figure 3.5:  $C_N^2$  vs time for a) 30 July (case (i) in the text) and b) 10 June (case (ii))

scale of the turbulence,  $L_0 > 10$  m a great deal of the time. Not only that, but the close correlation of individual peaks leads one to envisage single large, intense cells containing most of the turbulent energy, drifting across the aperture of a telescope, no more than a few tens of metres above the surface. As will be discussed in the next chapter, even though this turbulence produces very poor seeing much of the time, the scenario is ideal from the point of view of adaptive optics, where the isoplanatic angle and coherence time depend very heavily on the structure and altitude of the turbulent cells responsible for the majority of the wavefront distortion (Section 4.4).

This result also has implications for the assumptions made in the Kolmogorov theory about the development and power spectrum of turbulent layers close to the surface. If the measurements on such widely different spatial scales are proportional in both phase and intensity, then these conditions do not appear to represent “fully-developed” turbulence, and hence their effect on the seeing may, perhaps, not be accurately quantified by the usual formalism.

#### Case(ii):

The second case described in the table, in which both the temperature inversion and  $C_N^2$  readings are relatively very low, generally occurs during bad weather for astronomy: significant cloud cover with lower level blowing snow. An example of the seeing measured during these conditions is shown in Fig. 3.5(b). Moderate to heavy cloud cover effectively suppresses the temperature inversion, which in turn reduces turbulent mixing. Winds are often rather strong in these conditions (up to  $10 \text{ ms}^{-1}$ ). Although low relative to the average value of this experiment, the  $C_N^2$  values remain in the  $10^{-14} \text{ m}^{-2/3}$  range, giving a seeing contribution over the height of the mast of slightly above  $0.1''$ , which is still quite large by the standards of most mid-latitude sites. Also, as shown in Fig 3.4(a), these weather conditions are not *always* associated with low turbulence.

These two situations (Fig. 3.5(a,b)) are good examples of the effect of both temperature gradients, and wind speeds and gradients, on the seeing contribution from the surface layer. It was generally expected that the lower-level seeing would be caused by the combination of these factors — wind gradients providing mechanical mixing of different temperature layers to generate optical turbulence — and many of our observations reinforced this point very clearly.

**Case (iii):**

Case (iii) illustrates the most common conditions for the occurrence of relatively good surface-layer seeing during good weather. The temperature inversion is large and uneven; up to 10°C or more from 7–27 m, concentrated in the lower section. Fig. 3.6(b) is an example of this case. The inversion was so intense that it saturated the amplifier for the 7–17 m section for much of the duration of the run. Once again, it appears that the turbulent layer closest to the surface has a depth roughly equal to the height of the mast, or slightly less.

This was the scenario for much of the data where low  $C_N^2$  measurements were obtained during good weather. Wind speeds were generally lower than usual, at around 3–5 ms<sup>-1</sup>, with the wind out of grid 90–120° — the wind direction most commonly associated with clear, cold weather at the South Pole. Under these conditions, the surface layer is dominated by the inversion wind (see Fig. 5.3). Some direct observations of what happens to the seeing where the surface winds meet the synoptic flow in the lower free atmosphere are discussed in more detail in Chapter 4. Here, however, it can be seen that the light inversion wind produces a relatively very stable layer near the surface, tending to suppress turbulent mixing in the first few tens of metres, at least. This is despite the fact that the temperature inversion is very strong.

While this is an encouraging result, the general picture that was emerging by now warned against undue optimism about the turbulence conditions in the lower boundary layer. It is quite possible, for example, that the lowest wind-shear layer had merely been forced by the stable inversion wind at the surface to an elevation above the height of the mast, with the associated strong optical turbulence.

Finally, for this example, we see once again the close correlation between the temperature fluctuations measured on scales of 0.3 m and 10 m. This appears to be another example of the “breaking wave” structure, with little development of the turbulence on a small spatial scale.

**Case (iv):**

The final characteristic conditions, described as case (iv) in the table, with an example shown in Fig. 3.6, again relate to data for which the seeing contribution was quite small. This case occurred about 10% of the time, and is hence more difficult to analyse in terms of meteorological parameters due to the small sample size.

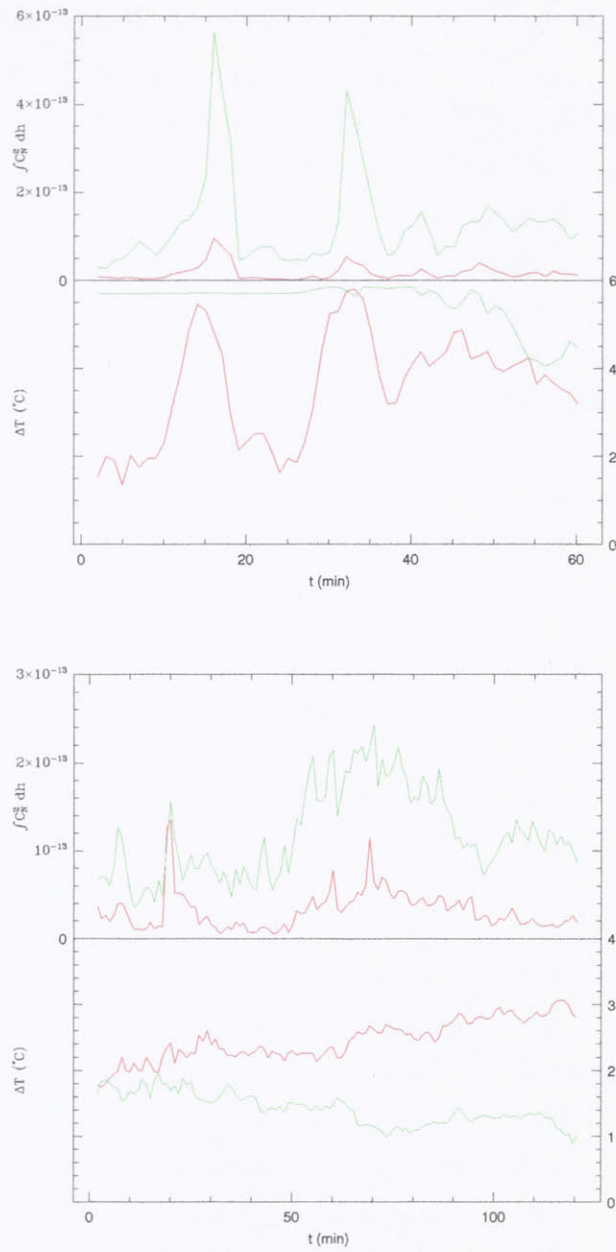


Figure 3.6:  $C_N^2$  vs time for a) 02 July (case (iii) in the text), and b) 24 June (case (iv))

It appears to be representative of quite a different surface layer structure, since the temperature gradient actually becomes steeper over the height of the mast, although the bulk of the optical turbulence is still concentrated near the surface. The common factor in these measurements, is, once again, the very low surface level wind speeds: less than  $4 \text{ ms}^{-1}$ . The wind direction may be less important, however, with surface wind directions anywhere from grid  $30\text{--}90^\circ$ , indicating that the inversion wind is therefore probably less of a dominant factor.

The difference between the  $C_N^2\text{--}\Delta T$  comparison here and in cases (i) and (iii) is quite striking in terms of the apparent structure of the turbulence. The  $C_N^2$  values measured at each level, on the 0.3 m scale, vary much more rapidly and randomly with respect to the larger scale temperature fluctuations. The surface layer is no longer dominated by massive, slowly-evolving individual cells, but instead seems to be more fully-developed, in terms of the spatial spectrum. The clue must lie in the different wind and temperature structure, but it is very difficult to draw any conclusions on the basis of the minimal weather data available.

### 3.3 Comparison with other sites

Microthermal and acoustic measurements of optical turbulence at surface level (in the first few tens of metres) have been carried out at several mid-latitude observatory sites (ESO-VLT working group 1987, Vernin & Tuñón-Muñoz 1992, Gur'yanov et al. 1988) and these results offer quite an illuminating comparison with the data presented here. Fig. 3.7 is a summary of the surface layer data from several of the best mid-latitude sites, taken from Gur'yanov et al. (1988) and replotted for clarity, along with average  $C_N^2$  from each of the three levels measured at the South Pole.

The results from the South Pole stand out in this comparison as representing an entirely different vertical optical turbulence structure from anywhere else, with the measured signal about a factor of 10 greater than any of these sites over this small range. Most of the sites displayed here start off in the  $C_N^2 = 10^{-14}$  to  $10^{-15} \text{ m}^{-2/3}$  range and many of them drop quite sharply over the 60 m vertical scale of this figure. Note that the quoted values from Mauna Kea and Mt. Graham (Merrill & Forbes 1987) were taken with a SODAR, which introduces a possible uncertainty, considered by Gur'yanov to be potentially quite large (with the microthermal measurements in better agreement with optical data).

The integrated seeing contribution from the region of 0–30 m or so is generally in the  $0.1''$  range (ESO-VLT working group 1987, Vernin & Tuñon-Muñoz 1994). If the comparison were to continue in this vein throughout the boundary layer and into the free atmosphere, then the integrated seeing at the South Pole would surely be many times that of the other sites (most of which enjoy  $\varepsilon_{\text{fwhm}} = 0.7\text{--}1.0''$  or so, on average). The minimal amount of anecdotal evidence for the total seeing from the surface at the South Pole available up to this point in time indicated an average somewhere in the region of  $1\text{--}2''$ , occasionally higher. This value, while not very impressive, does indicate that, at some fairly low altitude, the  $C_N^2$  curve must drop down to a level in line with the other sites, since a large fraction of the extra  $1''$  or so is already accounted for by the data presented in this chapter. As will be seen in the boundary layer / free atmosphere study of Chapter 4, this indeed is the case; in fact, the optical turbulence at the South Pole falls well below most other sites upward of 100–200 m.

### 3.4 Discussion

For the reasons described earlier, it was expected that boundary layer turbulence would generate a substantial fraction, and probably the majority, of the seeing above the South Pole. This experiment was intended to provide some insight into the intensity and structure of the optical turbulence near the surface, as a first-order estimate of the total boundary layer contribution.

In terms of these aims, the experiment was a great success. These results confirm that the strong temperature inversion present over the cold ice of the high antarctic plateau, combined with the interaction of the inversion wind and geostrophic air flow, produces a very intense seeing contribution near the surface, which is often an order of magnitude greater than that observed at other sites around the world, and certainly stronger than we would have expected. The measured values averaged around  $0.6''$  over the 20 m slice between 7–27 m, and varied between  $0.1''$  to more than  $1''$  – a severe amount of optical turbulence for such a minute fraction of the total atmosphere. It is worth a reminder, at this point, that the seeing contributions from the different altitude turbulent layers in the atmosphere do not add linearly in terms of  $\varepsilon_{\text{fwhm}}$  (Eq. 2.7), and the contribution of the surface layer will be somewhat less when considered as part of an integrated value over the entire atmosphere.

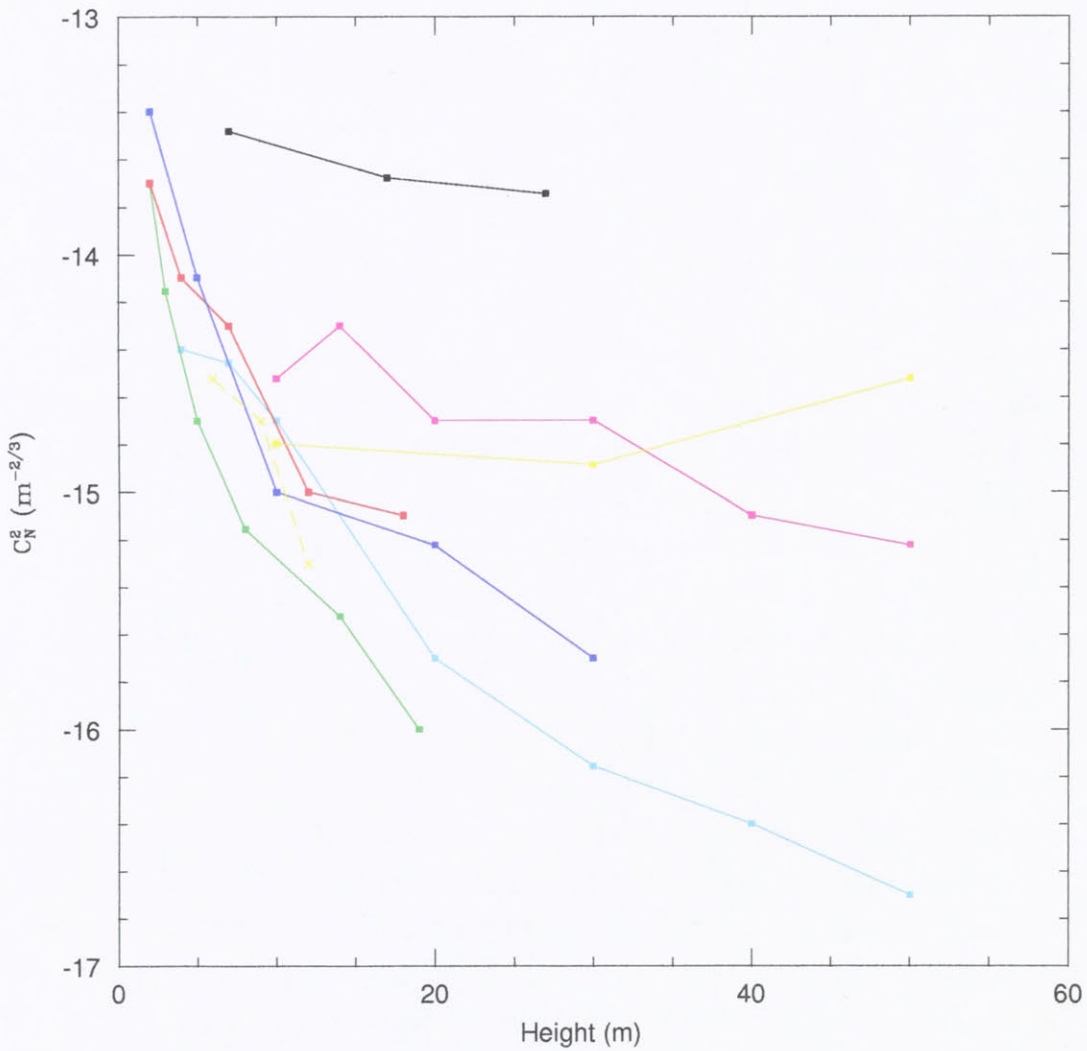


**Figure 3.7:** Comparison of the  $C_N^2$  profile at the South Pole (black) with a range of mid-latitude sites: Special Astrophysical Observatory, Mt. Pastukhov (red), Institute of Astrophysics, Mt. Sanglok, Tadjikistan (green), Mt. Maidanak, Uzbekistan (blue), (all Gur'yanov et al. 1988); Mt. Graham, Arizona (magenta), Mauna Kea, Hawaii (cyan), (both Merrill & Forbes 1987); La Silla, Chile (yellow, solid), (ESO-VLT working group 1987); La Palma, Canary Is. (yellow, dashed), (Vernin & Tuñon-Muñoz 1992)

The results also show that the lowest turbulent layer is thin enough to be resolved by our array of sensors much of the time, and some clear correlations between larger-scale weather parameters and microthermal turbulence were observed. These comparisons reveal a fascinating relationship between the large and small-scale patterns, and it is clear that the major factor in the strong optical turbulence observed is an intense and variable temperature inversion, which is unique to this site (and other potential sites on the antarctic plateau, of course).

Very little data has ever been obtained at the South Pole that is directly relevant to the study of astronomical seeing. The acoustic soundings of Neff (1981) in the 1970s are very valuable. Although it has relatively poor resolution, this experiment did illustrate the turbulence structure of the lower boundary layer, and agreed with our measurements of a very intense layer right above the surface which was often limited to the first 30 m or so. The acoustic backscatter data generally indicate that the turbulence is not evenly distributed throughout the boundary layer but, rather, occurs in two or three narrow, intense layers, such as the lowest one measured by our vertical array of microthermal sensors on the tower. They also indicate a sharply-defined upper limit to the boundary layer turbulence. The “breaking wave” characteristics that were a feature of much of our data are also evident in Neff’s study. The seeing contribution of the entire boundary layer and free atmosphere is studied in detail in Chapter 4.

It seems that the surface layer turbulence measured in this experiment is intense enough that significant gains can be achieved by placing a telescope on a raised platform of 30–40 m in height, thereby avoiding a significant fraction of the seeing. With this consideration in mind, the second phase of the experiment (balloon-borne sondes) began to take on more importance than we had initially imagined. At this point in the campaign, it appeared possible that, under favourable conditions, there may exist a situation where almost the entire seeing contribution occurs close enough to the surface (say,  $\sim 2$  times the height of the mast), in perhaps only one or two layers, that a telescope might feasibly be raised above almost all of the seeing, with a need for only a modest engineering effort to elevate it by a few tens of metres. This could lead to the attainment of the so-called “super seeing” that was predicted for the free atmosphere. This possibility could be proven one way or the other quite simply, once we were able to sample  $C_N^2$  higher in the boundary layer.

Another aspect of this study of great importance to the long-term plans for a

large telescope in Antarctica is the feasibility of using image correction techniques at this site. This question, too, is discussed further in Chapter 4, however some initial comments can be made on the basis of the data from the tower. The limiting factors in any adaptive optics method are the spatial and temporal coherence of the wavefront that one is trying to correct. In general, the high-altitude turbulence that forms a large proportion of the seeing at many mid-latitude sites is very difficult to correct, and very sophisticated methods are usually required to extract much improvement in image quality (e.g. Cowie & Songaila 1988), since it is isoplanatic over an angular scale of only a few arcseconds. Here, however, we have the exact opposite scenario, where a very large proportion of the turbulence is produced very close to the aperture of the telescope, and so the isoplanatic angle should be much larger. Indeed, considering the single large turbulent cells that were often observed, we might reasonably expect that the South Pole should be almost the ideal site for the application of relatively simple low-order image correction methods, even despite the large amplitude of the fluctuations observed.

## Chapter 4

# BOUNDARY LAYER / FREE ATMOSPHERE SEEING

The second season of the campaign to measure the seeing and characterise the atmospheric turbulence profile above the South Pole was based on the use of balloon-borne radiosondes. These balloons usually ascend to an altitude of 20 km or more, sending back data with a vertical resolution of 5 m. This provides a means to determine the total FWHM seeing via Eqs. 2.4-2.6. The microthermal sondes from the Université de Nice used exactly the same type of sensors as had been placed on the NOAA tower the previous year (see Ch. 3), enabling a direct comparison with the previous season's data, and providing a smooth transition between the surface level and boundary layer/free atmosphere profiles. Balloon launches were scheduled for the entire dark season, and eventually took place from June through August, 1995.

The results from the sensors on the tower had indicated very strong optical turbulence near the surface: over  $0.6''$  from 7-27 m alone (Ch. 3). Although it was predicted that the boundary layer would produce a disproportionate amount of the seeing at the South Pole relative to other sites (where the contribution is generally  $\leq 0.1''$ ), the very strong and variable signal measured from the tower made it clear that determining the vertical extent of turbulence in the boundary layer was of utmost importance in characterising the seeing at this site.

The second phase of the experiment was carried out successfully, after some initial problems, mainly related to the difficulty of performing the balloon launches in the extreme cold conditions. Not only was the integrated seeing obtained from a

large number of balloon flights, but a great deal of knowledge was gleaned from the data about the vertical profile of the turbulence, and, importantly, its relationship with wind velocity and temperature profiles.

## 4.1 Method

The principles underlying this experiment are essentially the same as described for the tower (Ch. 3). Two pairs of microthermal sensors were attached to each sonde, as a check for inconsistencies in the raw data (perhaps caused by spurious turbulence generated by the balloon or sonde), and as a safeguard against any breakages during the launch procedure or free flight. The separation used was  $|\rho| = 0.3$  m, well within the inertial sub-range. The initial processing hardware, i.e. the amplifier and RMS circuitry, was carried on-board inside the insulated payload. The relevant turbulence data is thus transmitted in the form of  $D_T$  values (see Eq. 2.2).

A standard Vaisala sonde was attached as well, to relay temperature, atmospheric pressure and humidity data, essential for the calculation of  $C_N^2$  via Eq. 2.4. The telemetry stream thus included both the microthermal and essential accompanying meteorological data. A line of data was transmitted every 1.5 s, and the balloons were inflated so as to ascend at a rate of approximately  $3\text{--}4\text{ ms}^{-1}$  — about the right rate to resolve the narrowest turbulent slices in the atmosphere. Inspection of the raw data confirmed that the resolution was fine enough that linear interpolation between the data points was an accurate method to calculate the integral  $\int_{h_0}^{\infty} C_N^2(h)dh$ ; i.e. there were no fine turbulent layers “squeezed” unnoticed in between the data points.

In addition, launches were timed to coincide with the daily weather balloon launch by the Meteorology Department. This enabled us to access their wind velocity measurements, in addition to providing confirmation of our pressure and temperature measurements.

Since the data from the two flights were not transmitted from exactly the same levels during the ascent, all data sets from both the Met and microthermal sondes were standardised to 5 m altitude increments by linear interpolation, to enable the construction of a single file containing all relevant data, as well as improving the comparison of fine-structure features between flights. The required  $C_N^2$  integrals were then calculated by incrementing between the mid-point of each 5 m slice.

A few factors limited the accuracy of the turbulence sampling in the region close to the surface. Ideally, the microthermal sensors should be at least 50 m below the balloon in order to minimise the effect of the turbulent wake of the balloon itself during ascent. Under polar winter conditions, however, it can be very difficult to achieve a “clean” launch with a tether of this length. After a couple of early abortive attempts to launch using a very long tether, the method ultimately used was to attach a tether of 10–20 m during the launch, with a pay-out reel included to add another 30 m or so to the length during the early part of the ascent. This ensured the successful launch of almost all of the balloons from that point on. The disadvantage is that the turbulent wake of the balloon can have an unquantifiable effect on the data during the early part of the flight, before the tether rolls out to its full extent.

Another problem, recognised in similar experiments at other sites around the world (e.g. Bufton 1973), is that the first 5–10 s of each flight’s data are generally contaminated by large temperature fluctuations associated with the launch procedure itself. This effect is, of course, greatly magnified on the polar plateau, where the temperature differential between the preparation area and the ambient air may be as much as 80–100 °C.

Due to the combination of these two effects, it was estimated that the first 30–50 m of data from each flight would be unusable, or at least greatly overestimated. Two methods were used to try to estimate the contribution from this region, including reference to the data from the previous season, taking into account the prevailing weather conditions at the time of the launch. This analysis is discussed in Sect. 4.2.

One final consideration was that the balloons reached a lower altitude than usual before they burst. This was due to balloon material weakening under the very cold conditions, exacerbated by the fact that the microthermal sondes are significant heavier than the small Vaisala instruments used by the Met department, requiring the balloons to be inflated more to gain the required speed of ascent. The maximum altitude was typically 12–15 km (100–150 hPa) above sea-level, rather than the 25+ km that would normally be expected. Thus we could not sample any optical turbulence that may have been present above about 15 km. Due to the very low air pressure at this altitude (Eq. 2.4), however, and the lack of a significant disequilibrium in temperature or wind velocity gradients (confirmed by Met and NOAA data), this was not expected to have a serious impact on the results. The

single flight that did attain a height of  $> 20$  km confirmed the fact that the signal continued at a very low level. Integrating over this profile, as well as using an artificial  $C_N^2$  profile based on pressure and temperature data from the Met launches indicated that the unsampled region of the atmosphere contributed around  $0.01''$  to the FWHM seeing.

## 4.2 Results

### 4.2.1 Summary

Fifteen balloon launches were successfully completed between June 20 and August 18, 1995. Out of a total of twenty-five sondes, four were either damaged during the launch or lost contact due to a fading signal, with another half-dozen used for test flights during the summer and early in the winter season.

The seeing measurements from the fifteen flights are summarised in Table 4.1. According to the weather observers' observations, ten of the fifteen flights took place in clear conditions, with a variable amount of cloud present on the other five days. The average total integrated FWHM (at  $\lambda = 0.5\mu\text{m}$ ) was measured to be  $1.86 \pm 0.02''$ , which corresponds to a Fried parameter of  $r_0 = 5.5$  cm. The great majority of this rather high seeing value is generated by the boundary layer, with an average free atmosphere contribution of only  $0.37''$  — about 7% of the integrated  $C_N^2$  measurements, based on Eq. 2.7. Sub-arcsecond seeing from surface level occurs about 20–25% of the time (three flights recording total integrated seeing  $< 1''$ ). The median seeing is somewhat lower than the mean ( $1.6''$ ), with the mean value pushed up by two or three occasions of very poor seeing around the  $3''$  level.

The statistical distributions of both total and free atmosphere seeing contributions are shown in Table 4.1. Conditions are widely variable among the 15 flights, with a standard deviation among the integrated seeing measurements of  $\sigma_T = 0.75''$ . Almost all of this variability occurred in the boundary layer, as the free atmosphere remained very stable throughout the season — from  $0.23$ – $0.42''$ , with a single measurement up to  $0.52''$ , giving a standard deviation of  $\sigma_{FA} = 0.07''$ . The strong and highly variable optical turbulence measured through the boundary layer is consistent with the results from the previous season (Chapter 3), where the  $C_N^2$  readings from the 27 m tower averaged over  $0.6''$ , with individual values ranging from  $0.1''$  to over  $1''$ .

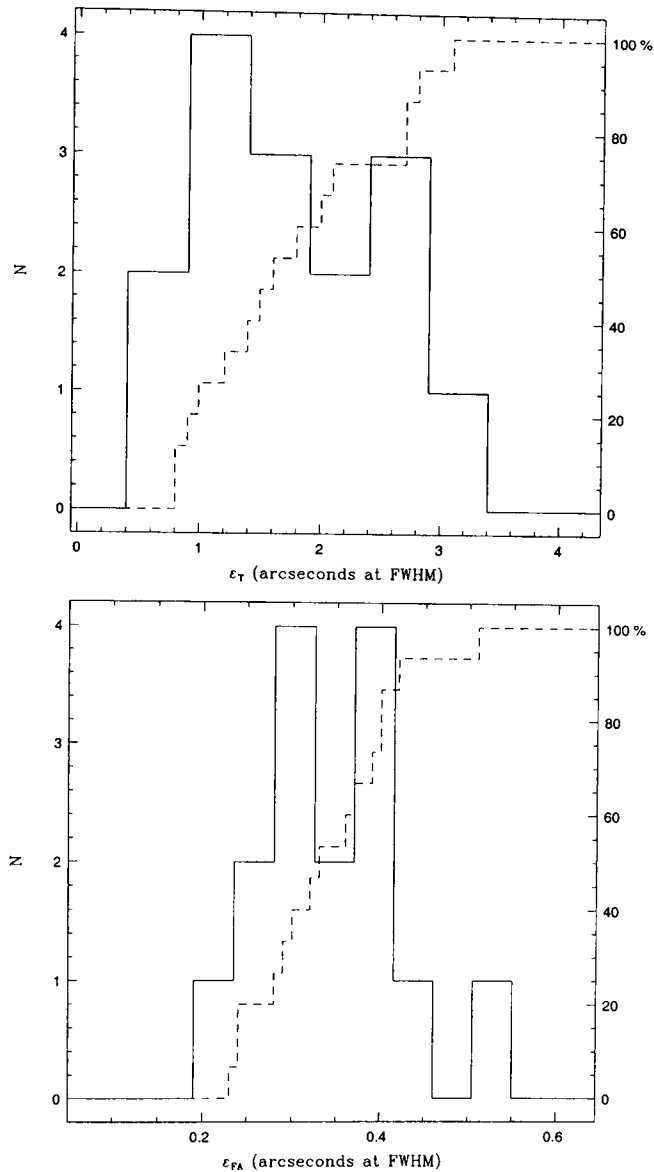


**Figure 4.1:** Seeing data statistics: full-width half-maximum probability distribution and associated cumulative distribution for the 15 balloon sondes launched in 1995: a) total (from ground level), b) free atmosphere.

Measurement	Mean	Std. Dev.	Median	Best 25%	Best	Worst
Seeing (arcseconds)						
-total	1.86±0.04	0.75	1.6	1.0	0.8	3.1
-free atmosphere	0.37	0.07	0.32	0.29	0.23	0.52
$r_0$ (cm)						
-total	5.48±0.05	3.40	6.4	9.9	12.3	3.3
-free atmosphere	27.2	7.2	28.2	34.8	44.6	23.3
Boundary layer height (m)	220	70	190	165	120	275

**Table 4.1:** Summary of integrated seeing and boundary layer data, from 15 balloon launches between 20 June and 18 August 1995. The “free atmosphere” refers to the entire atmosphere excluding the boundary layer. Values are quoted for a wavelength of 0.5  $\mu\text{m}$ .

As mentioned above, it was necessary to make an approximation for the contribution from the lowest 30–50 m or so, as the data from the balloon-borne sensors were not valid in this very important region (a link between the measurements from the tower up to 27 m and the rest of the boundary layer). Two methods were used to deal with this problem. The first method was simply to compare the average  $C_N^2$  profile from 0–30 m with the data from the Met tower during the previous year. The long-term averages from the mast should be about the same as for the same region averaged over a sample of 15 flights, and should therefore give a good indication of the lower limit of validity of the balloon data, as shown in Fig. 4.2. An extrapolation can be made across the unsampled region based on this comparison. It can be seen from the figure that the  $C_N^2$  values from 0–30 m from the balloon-borne sondes are about a factor of 4 higher than the average readings from the tower, and are clearly artificially elevated.

The problem was also approached by examining the raw data from the individual flights in detail, with particular reference to the wind velocity and temperature gradients. Given the observed correlation between strong vertical wind and temperature fluctuations, and microthermal turbulence (discussed in detail in Sect. 4.2.2), the  $C_N^2$  values close to the surface were edited by hand for each flight, before being included in the computation for the integrated seeing. The results using this method are also included in the figure. While this subjective analysis is a weaker

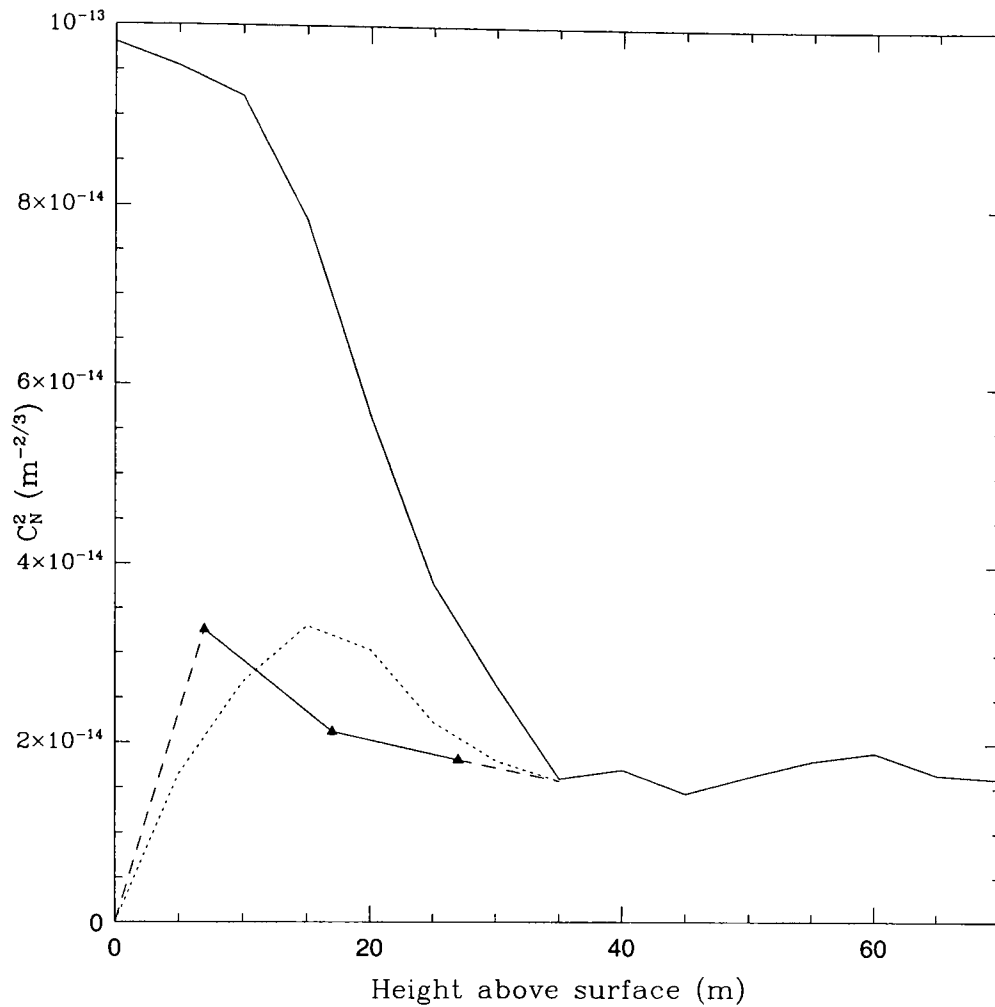


**Figure 4.2:** Average  $C_N^2$  profile up to a height of 70 m, calculated from the 15 balloon sondes. Included are the two methods used to determine the lower altitude limit of the data, and extrapolate down to the surface. The mean  $C_N^2$  measurements from the 27 m-high tower (Marks et al. 1996) are indicated by the triangles, with extrapolations from 0–7 m and from 27–35 m shown by the dashed lines. The dotted line shows the average values obtained by editing the individual  $C_N^2$  profiles in the 0–40 m range, with reference to the corresponding wind and temperature profiles.

approximation, it does provide an estimate for the lower-boundary layer profile for the individual flights, and is thus useful for an analysis of the vertical turbulence structure.

The cut-off point for the balloon data was found to be 35–40 m, and the results obtained using the two methods for the atmosphere below this point agree quite closely. The uncertainty limits quoted in the table represent the discrepancy between the two methods of calculation.

The full  $C_N^2$  profile at the South Pole is shown in Fig. 4.3, as well as a more detailed plot of the first 1000 m above the surface. Corresponding profiles for microthermal data taken at Cerro Paranal are included for comparison (see Sect. 4.3).

The height of the boundary layer, in terms of microthermal turbulence, was about 220 m on average, with values ranging from 120–275 m. The criterion used to define the top of the boundary layer for each flight was the lowest height,  $h_0$ , for which successive calculations of the integrated seeing up to that point (using standardised 5 m altitude increments) varied according to

$$\varepsilon_{h_0+1}^\infty - \varepsilon_{h_0}^\infty \leq 0.001'' \quad (4.1)$$

where the sub- and super-scripts refer to the integration limits in Eq. 2.6.

This definition gives a much lower figure than the 300–500 m temperature inversion that usually defines the boundary layer depth at the South Pole. This is due to the fact that the optical turbulence intensity depends strongly on the vertical gradients of the wind velocity and temperature inversion. Near the top of the boundary layer, the inversion begins to flatten out at around 200–250 m, at which point the microthermal turbulence becomes quiet, even though the inversion continues weakly for a further 100 m or more.

In contrast with the severe optical turbulence present in the boundary layer, the free atmosphere is very quiescent in comparison with other sites. The tropopause is very weak, and only produces a noticeable increase in  $C_N^2$  above the background on two or three occasions. The inversion that often occurs in the tropopause at mid-latitudes does not exist here. Instead, the temperature profile generally levels off weakly and smoothly. However there are occasional slices of relatively high turbulence elsewhere in the free atmosphere from time to time, however, which appear at random altitudes. These peaks are invariably associated with disturbances in the temperature or wind velocity profiles, and are examined further in Sect. 4.2.3.

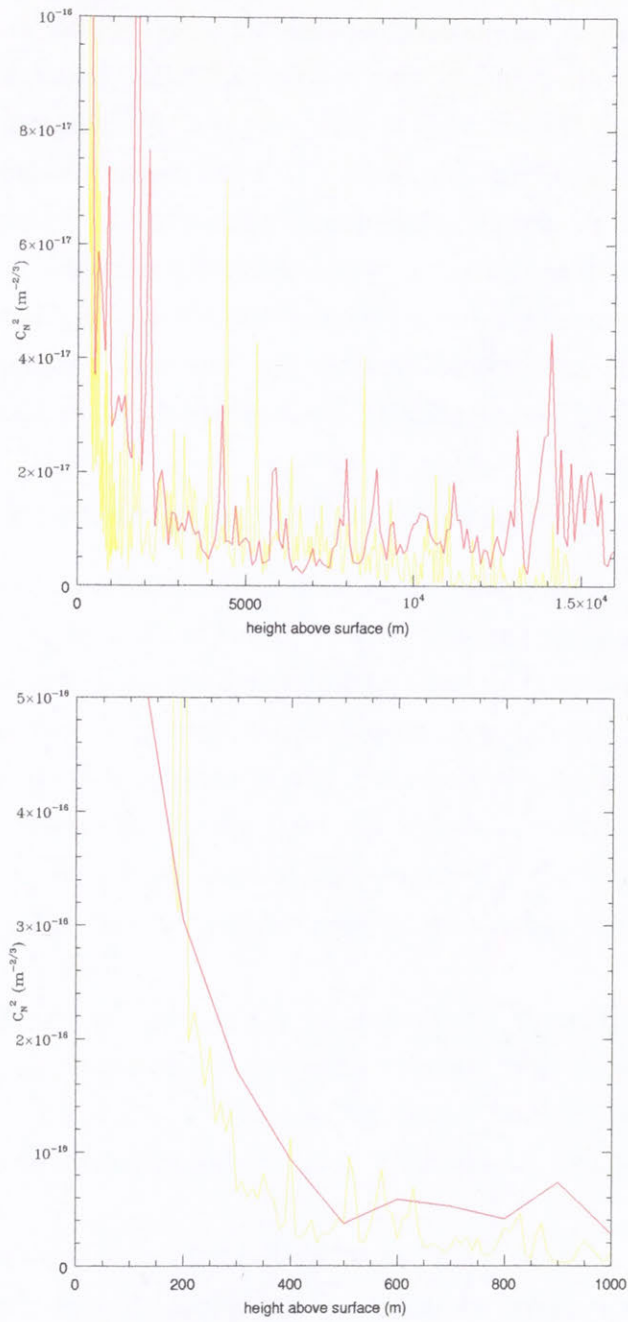


**Figure 4.3:**  $C_N^2$  vs altitude for the South Pole (yellow) and Cerro Paranal (red) Fuchs (1995):  
a) total atmosphere and b) boundary layer

All results here apply to visual wavelengths, with the calculations performed with  $\lambda = 0.5\mu\text{m}$ . This is a standard wavelength for comparison with other sites. More importantly, from the point of view of Antarctic astronomy, however, are the values at infrared wavelengths, since it is in the IR that the greatest gains stand to be made over other terrestrial sites. Calculations of  $\varepsilon_{\text{fwhm}}$  and  $r_0$  at different wavelengths are straightforward, depending simply on the scaling factors noted in Eq. 2.8–2.9. The relevant values are presented in Sect. 4.5 for  $\lambda = 2.4\mu\text{m}$  (K band) — one of the key near-IR wavelengths where significant gains stand to be made in Antarctica, due to the very low thermal background, and the natural minimum in airglow emission at this wavelength (Phillips et al. 1999).

## 4.2.2 Boundary layer characteristics

Our first experiment at the South Pole, using microthermal sensors to measure turbulence along a 27 m tower, showed that the optical turbulence can vary over an extremely wide range, depending to a large extent on the temperature gradient. This point has been demonstrated even more strongly with the balloon flights, where the total integrated seeing is heavily dependent on the structure of the boundary layer. Boundary layer  $C_N^2$  values occasionally reach over  $10^{-13}\text{m}^{-2/3}$  — near the saturation limit of our amplifiers. By contrast, the strongest layers observed in the free atmosphere reached no more than about  $10^{-15}\text{m}^{-2/3}$ , 2 orders of magnitude lower.

Fig. 4.4(a–f) is a plot of  $C_N^2$  vs. altitude for three of the balloon flights, including potential temperature<sup>1</sup> and wind velocity profiles, and illustrates some typical conditions. Fig. 4.4(a, c, e) show the boundary layer profiles, while Fig. 4.4(b, d, f) cover the entire atmosphere. Note that the  $C_N^2$  axis scales are different for each flight.

A striking feature of the data is that the boundary layer turbulence structure is not evenly spread throughout the inversion layer, but rather, is concentrated in anywhere from one to half a dozen narrow strips, generally 10–20 m in depth. They are almost always associated with a sharp peak in either the potential temperature or wind velocity gradient, or both. Quite often, the strongest turbulence above the surface layer appears close to the top of the boundary layer ( $\sim 200\text{m}$ , as defined

---

<sup>1</sup>Potential temperature is defined as:  $\theta(h) = T(h) \left( \frac{P(h)}{1000} \right)^{-0.286}$ . The value of  $\theta$  corresponds to the temperature of the air adjusted adiabatically to a standard pressure of 1000 hPa.

above). This is evident particularly in Fig. 4.4(a, c), for example, and was observed in several other flights. It corresponds to a very characteristic “two-tiered” inversion, indicated by the secondary peaks in  $|d\theta/dz|$  in these flights.

Almost all flights show intense turbulence extending from near the surface up to a height of 30–60 m. Although, as discussed above, it is impossible to separate this accurately due to the launch effects, the peak values of the natural turbulence do generally reach at least the mid- $10^{-14}\text{m}^{-2/3}$  range. Above this region, the intensity of single turbulent layers is highly variable, and can have an enormous effect on the total integrated seeing. Fig. 4.4(e), for example, contains very little optical turbulence above the surface layer, apart from a single region about 20 m wide, 60 m above the surface, which reaches a maximum  $C_N^2 = 10^{-13}\text{m}^{-2/3}$ . The integrated seeing for this flight was  $\varepsilon_T = 2.64''$ , which is well above average. It can be seen clearly on the graph that this layer coincides with both the top of the surface wind shear region, and a sharp peak in  $|d\theta/dz|$  of  $> 0.2^\circ$ . The combination of these factors leads here to one of the most intense single turbulent peaks observed during the whole season. Note that for this flight,  $\varepsilon_{FA} = 0.23''$ ; one of the lowest values measured. So, even though the seeing from the surface is very poor, it appears that a rise of less than 100 m is sufficient to avoid almost all of it.

Fig. 4.4(c) illustrates somewhat more typical conditions, with the usual strong surface layer component (up to about 60 m), followed by one or two weaker layers between  $10^{-14}$  and  $10^{-15}\text{m}^{-2/3}$  at around 200 m, resulting in near-average seeing of  $\varepsilon_T = 1.76''$ .

Sub-arcsecond seeing from ground level was observed in 3 of the 15 flights, and a correlation between the prevailing conditions during these flights is difficult to ascertain. One of the flights, at a relatively warm  $-42^\circ\text{C}$ , about  $18^\circ\text{C}$  above average, with a layer of broken cloud, low wind speed from grid SE and a small inversion, corresponds with case (ii) in Ch. 3: an influx of warmer air from the coast, counteracting the normal katabatic flow, and tending to smooth out the temperature gradient in the boundary layer (Schwerdtfeger 1984). In any case, despite the good seeing, this is fairly poor observing weather.

The other two sub-arcsecond flights took place during clear weather, and these, too, indicate very low wind shear throughout the boundary layer (e.g. Fig. 4.4(a)). The wind direction was from a more typical NE-E, and so there is no obvious explanation for the calm boundary layer seeing conditions.

The opposite applies for relatively poor seeing ( $\varepsilon_T > 2.5''$ ); it is usually caused

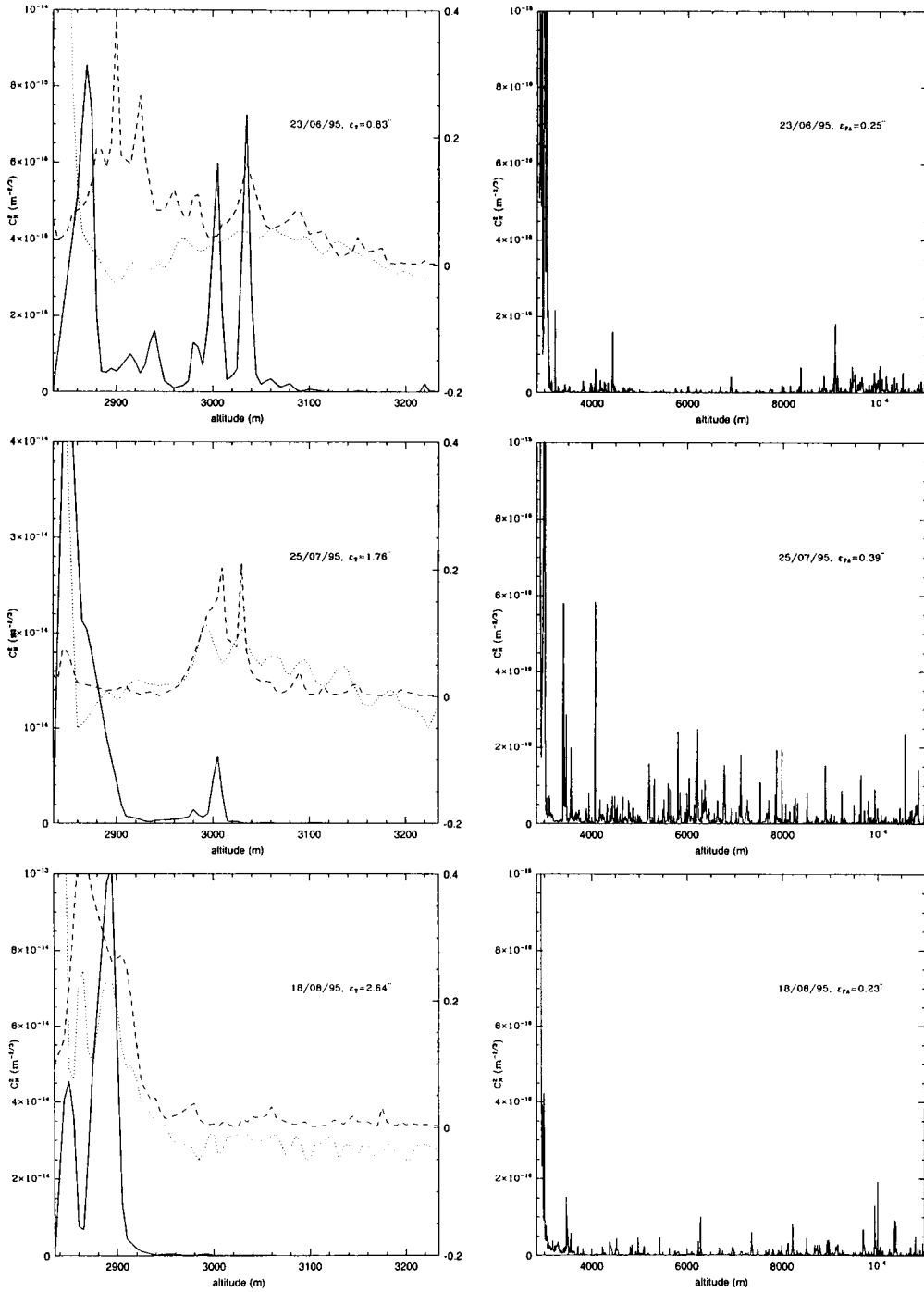


Figure 4.4:  $C_N^2$  vs. altitude: a-b) for 23/06/95, c-d) for 21/07/95, e-f) for 18/08/95. The boundary layer plots include potential temperature gradient,  $|d\theta/dz|$  (dashed lines) and wind velocity gradient,  $|dU/dz|$  (dotted lines). The axes on the right of each plot show  $|d\theta/dz|$ , in units of  $^\circ\text{C}/\text{m}^{-1}$ . Units for  $|dU/dz|$  are not shown; it is approximately equal to 0.5 (RHS axis scale)  $\text{ms}^{-1}$ , offset by  $-0.05$  for clarity.

by a small number of intense peaks (Fig. 4.4(e) is a good example) in  $|d\theta/dz|$ , combined with relatively strong wind shear. A frequent feature is the presence of the two-tiered inversion structure on these days. This tends to result in the single intense peaks that occur at elevations of not much more than about 100 m. This is still probably too high to think about avoiding physically (as opposed to the surface level turbulence, where 20–30 m tall telescope towers might be feasible), but it is an important observation for the consideration of adaptive optics. Optical seeing concentrated at such a low altitude is the ideal scenario for the successful application of image correction techniques, and in this sense, the worst seeing at the South Pole may turn out to be the easiest to eliminate. The potential for image correction at the site is discussed in more detail in Sect. 4.4.

Another common element in the poor-seeing flights is that the surface winds are somewhat stronger than usual, and tending towards  $90^\circ\text{E}$ ; i.e. the fall line of the terrain (see Fig. 1.1). This indicates that the dominance of the inversion wind near the surface is generating increased turbulence at its upper boundary (especially at these higher speeds), due to increased wind shears where it meets the geostrophic flow towards the top of the boundary layer.

Fig. 4.5 shows the  $C_T^2$ ,  $|d\theta/dz|$  and  $|dU/dz|$  profiles averaged over all 15 flights. The correlation between the three quantities confirms the observations made from the individual flights so far; the poor seeing close to the surface is dependent upon the existence of a strong positive temperature gradient, combined with mechanical turbulence produced by wind shear. The strong lower-boundary layer turbulence occurs almost all the time, since both the temperature inversion and the inversion wind component are just about permanent features of winter weather at the South Pole. This agrees with the general picture obtained from the tower, where the seeing contribution from 7–27 m above the surface is around  $0.6''$  on average, and  $> 0.3''$  75% of the time (Fig. 3.3).

These general observations agree broadly with the only other detailed study of atmospheric boundary layer turbulence undertaken at the South Pole, described by Neff (1981), and discussed briefly in the previous chapter. In this experiment, an acoustic sounder was used to probe the turbulence structure up to an altitude of  $\sim 1$  km. Although the acoustic backscatter measurements of  $C_N^2$  have much coarser vertical resolution than the microthermal sondes ( $\sim 10$ – $20$  m), the graphical representations of the turbulence shown in this study are very close to the results of the microthermal experiment; there is a turbulent layer close to the surface

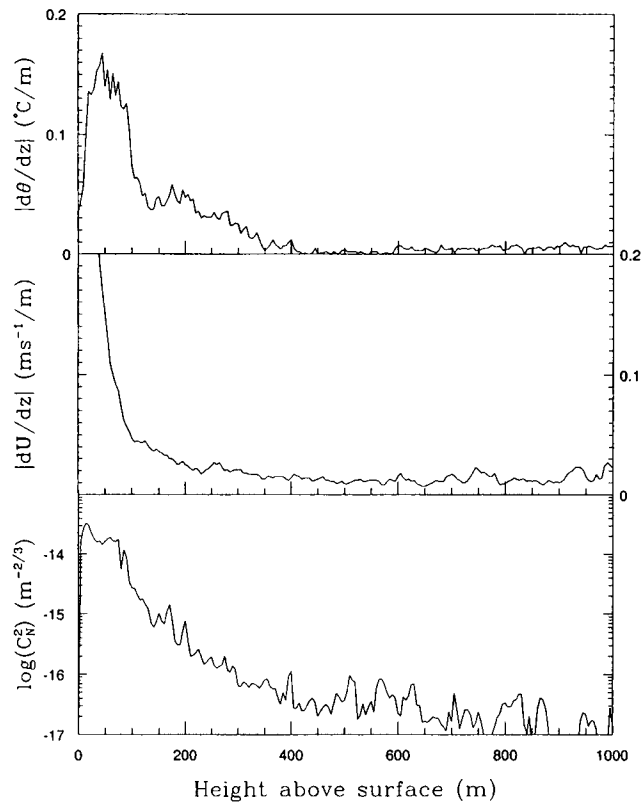


**Figure 4.5:** Average  $C_N^2$ ,  $|d\theta/dz|$ , and  $|dU/dz|$  profiles up to a height of 1km above the surface. Wind velocity data were obtained from weather balloon launches performed almost simultaneously with the microthermal flights.

almost constantly, with the occasional characteristic breaking-wave and striated turbulence associated with wind-shear, above an intermediate quiescent region. The upper limit of the SODAR turbulence data is also sharply defined, at an altitude of 200–300 m, with very much weaker activity thereafter. The two experiments are in agreement, that the turbulence terminates well below the height at which the temperature gradient changes from positive to negative (Schwerdtfeger 1984).

It should be pointed out that the discussion here of the best and worst boundary-layer seeing conditions, and corresponding  $C_N^2$  profiles, is based on statistics of only 3 or 4 examples in each case, and so any generalisations should be treated with caution. However, the observations described here do suggest possibilities for further analysis of the site seeing conditions, however. The fact that all  $C_N^2$  features can be related to peaks in the temperature or wind velocity gradients (or usually both) means that useful information should be present in all of the weather balloon launches.

The total number of significant boundary layer  $C_N^2$  peaks was, in fact, low enough that it was possible to study them all individually. Fig. 4.6(a, b) shows the relation between the turbulence strength of these layers, and the corresponding wind and temperature gradients. The original  $C_T^2$  values were used, in order to avoid the effects of pressure and temperature (Eq. 2.4). There was not a single peak in  $C_T^2$  without a corresponding elevation in  $|d\theta/dz|$  or  $|dU/dz|$ .

There do not appear to be any strong correlations in the data in the two plots. It is the combination of elements that causes the seeing, however, and so distinct correlations in these two graphs would not necessarily be expected, although the interesting structure in Fig. 4.6(b) is suggestive of a relationship between  $C_T^2$  and  $|d\theta/dz|$ .

In order to extract some more meaningful information from these values,  $C_N^2$  was plotted against  $|d\theta/dz|$  for peaks having the same wind gradient. The only single value of  $|dU/dz|$  with a good number of repeated occurrences was  $0.3 \text{ ms}^{-1}/\text{m}$ , and the results are displayed in Fig. 4.7. This time, a clear correlation is observed, and a straight line can be fitted, with a gradient of about 0.7. It seems that a minimum level of wind shear is therefore necessary to generate turbulence, but beyond that, its intensity is not important.

This result does not offer any new or surprising insights ; the main point is really to show that the seeing may, in many cases, be approximated using data from the daily weather balloons. Further work would be needed to quantify these ideas more

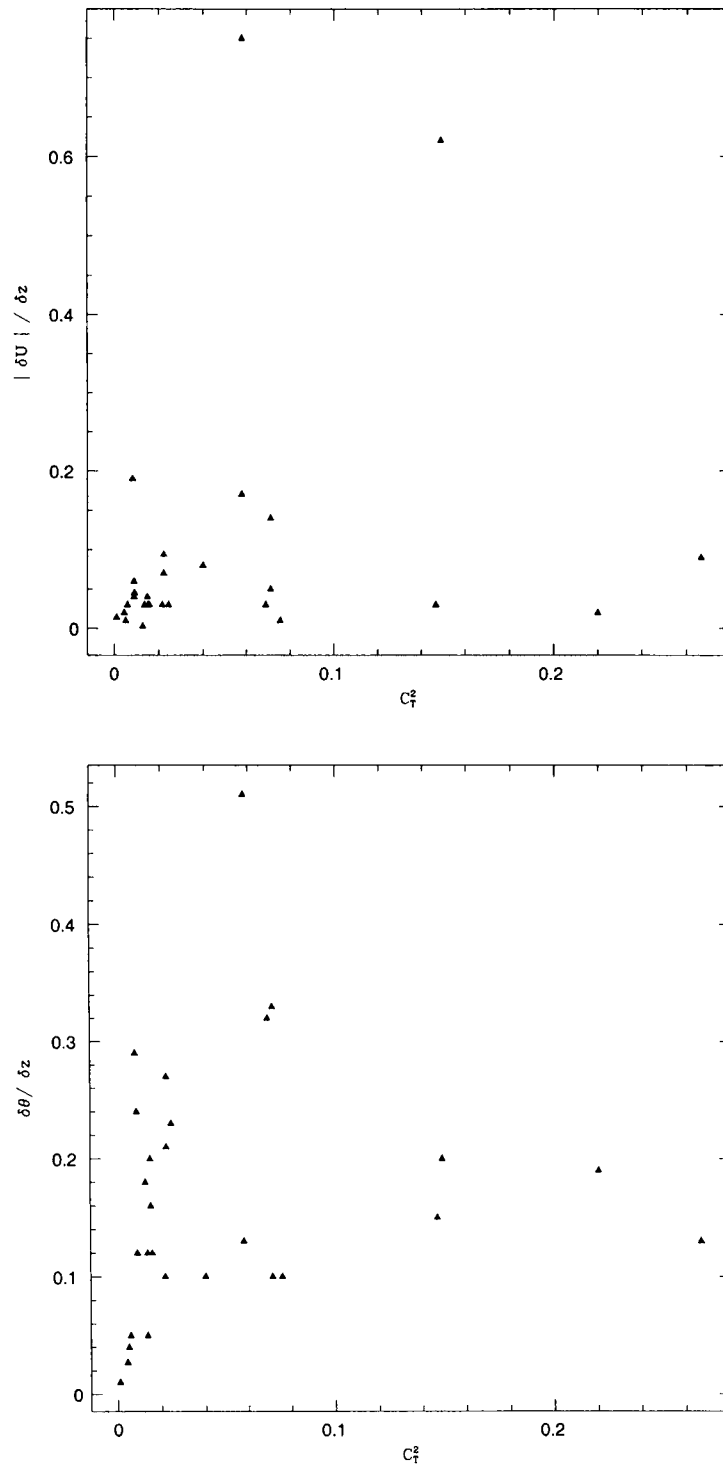


**Figure 4.6:** Comparison of all significant peaks with corresponding values of the wind and temperature gradients

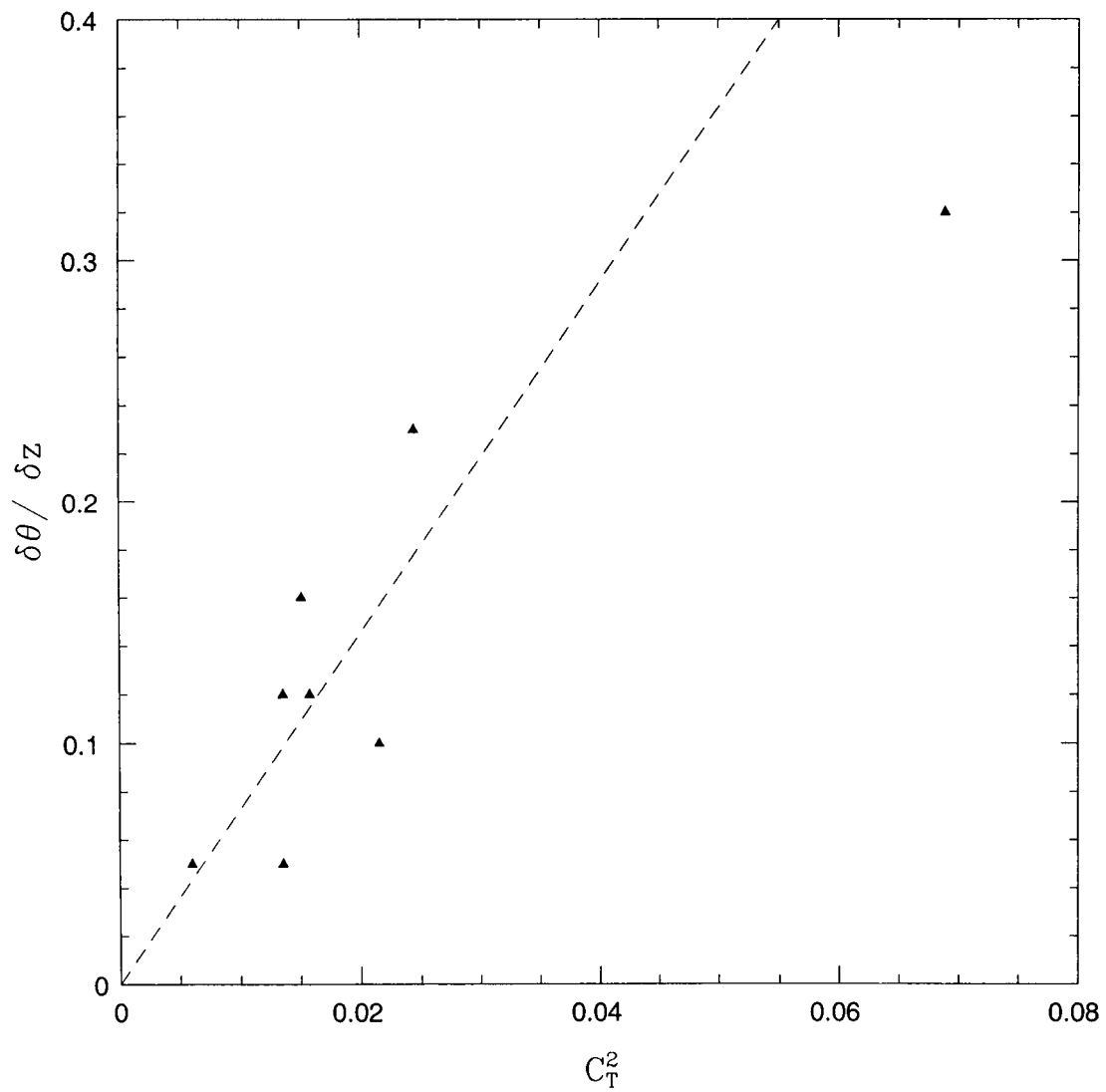


Figure 4.7:  $C_T^2$  vs  $|\delta\theta/\delta z|$  for  $C_T^2$  peaks with a corresponding wind velocity gradient of  $|dU/dz|=0.3\text{ ms}^{-1}$

accurately, for example, by comparing a larger number of weather balloon launches with visual seeing observations. This subject is discussed further in Sect. 4.2.4.

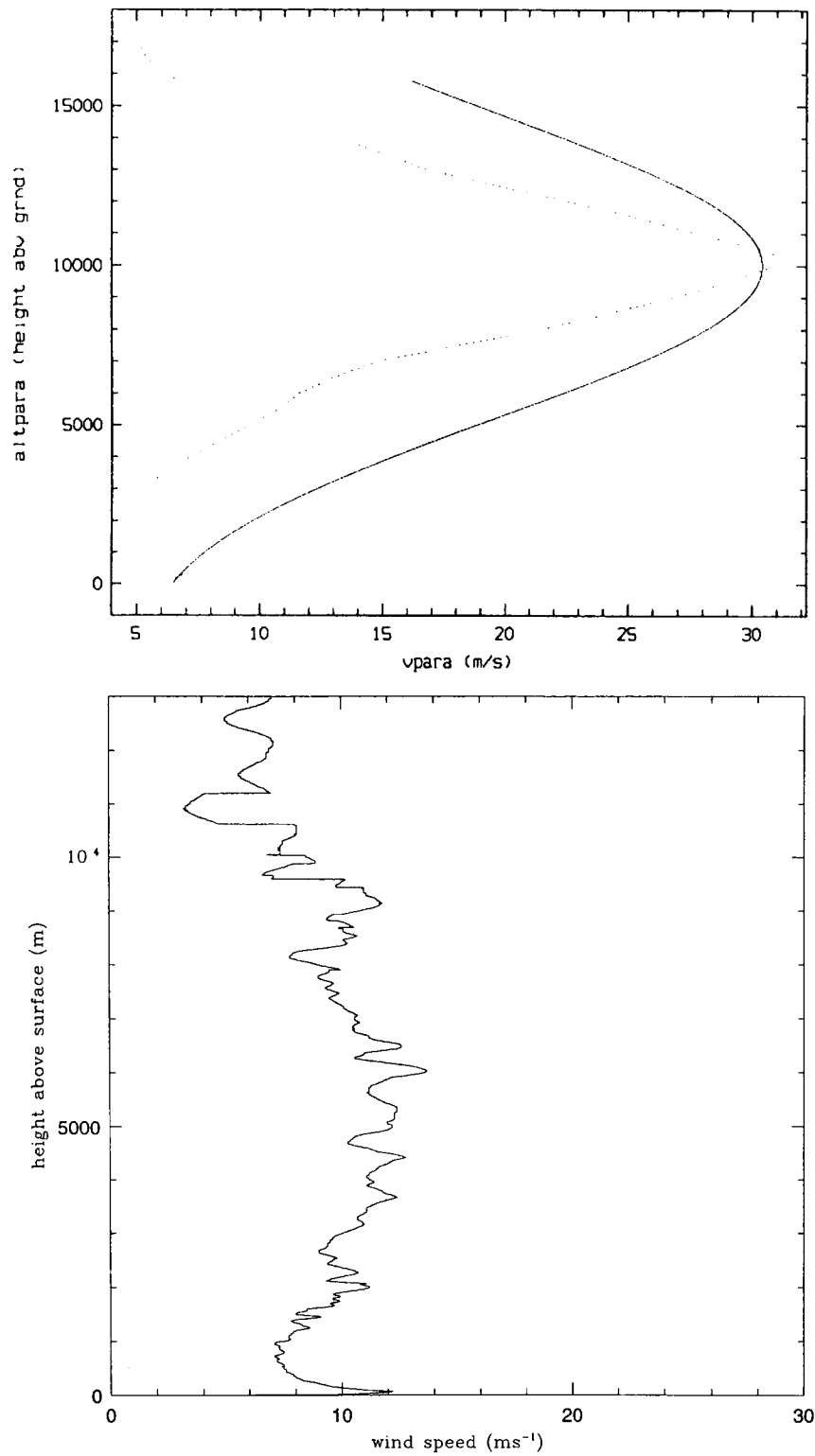
### 4.2.3 Free atmosphere characteristics

Similar comments to the boundary layer turbulence characteristics apply for the free atmosphere (taken here to mean the entire atmosphere above the limit of the boundary layer seeing, according to Eq. 4.1), although the effects are much smaller. Average troposphere winds are much calmer than probably anywhere to be found in the mid-latitudes (see Fig. 1.3). Fig. 4.8 shows the average wind speed profile averaged over all fifteen flights, in comparison with similar data from Cerro Paranal (note the distinction between wind speed and the wind velocity gradient, which includes a directional component). The sharp contrast between these profiles is an indicator of stability at the South Pole in terms of the seeing, since the lower wind speeds throughout the tropopause reduces the effect of any shear layers.

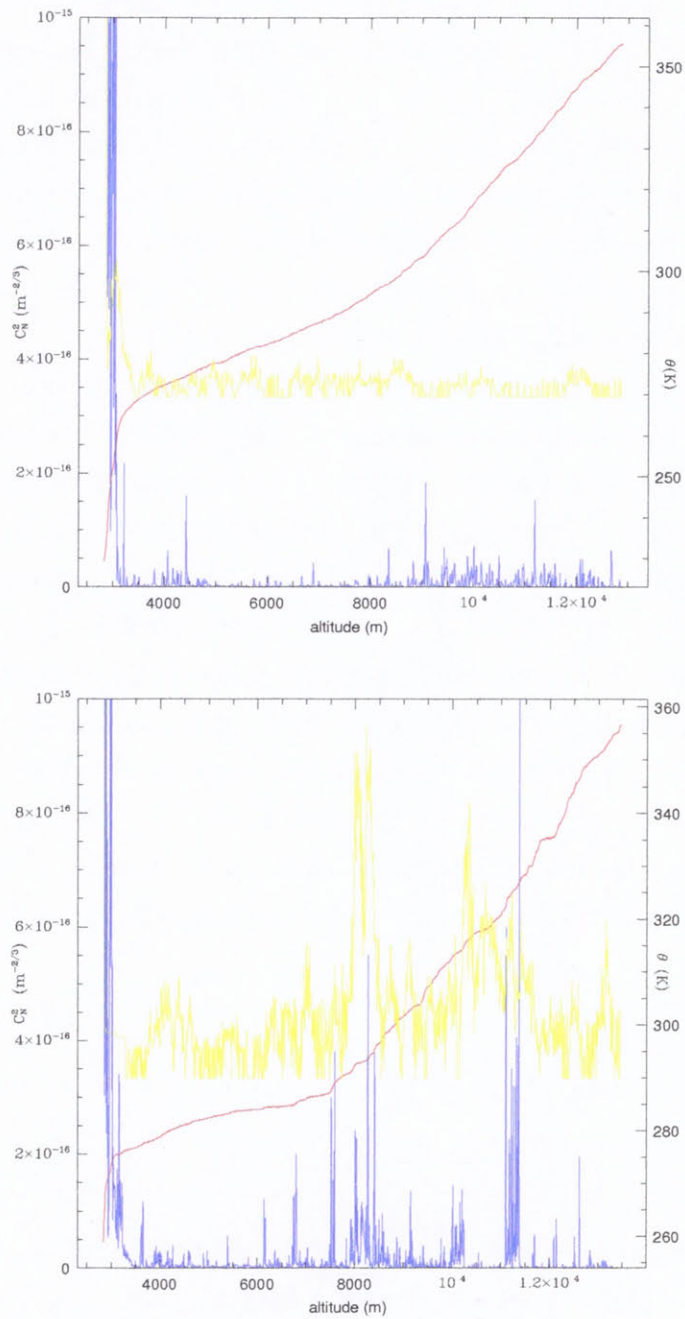
Fig. 4.9 shows examples of close to the best and worst free atmosphere seeing conditions, along with the potential temperature and wind velocity gradient in each case. The potential temperature increases smoothly in Fig. 4.9(a) (the same flight as Fig. 4.4(b)), which, in general, is an indication of a very stable atmosphere (Coulman 1985). The  $C_N^2$  profile contains only one or two peaks above  $10^{-16} \text{m}^{-2/3}$ , and the integrated seeing contribution from the free atmosphere (starting from 230 m on this day) was  $0.24''$ . There is very little indication of optical turbulence in the region of the tropopause at around 8–9 km (which is barely noticeable in the potential temperature profile), and nor are there any other regions of wind shear. Exceptionally stable free atmosphere conditions such as these were observed about 25% of the time. They represent close to the cleanest free atmosphere seeing conditions observed at any site on earth.

Fig. 4.9(b), on the other hand, has a much less stable temperature gradient, with several associated regions of relatively high  $C_N^2$  signal, into the high- $10^{-16} \text{m}^{-2/3}$  range. The total free atmosphere seeing contribution for this flight was  $0.42''$ , which was one of the highest measurements for the season. The strongest regions of optical turbulence are clearly linked to fluctuations in the potential temperature and some very strong wind shears, as observed in the boundary layer.

This free atmosphere profile is especially interesting since it appears to contain a number of the “twin layers” of  $C_N^2$  first described in detail by Vernin & Tuñon-



**Figure 4.8:** Average vertical wind speed profiles over a) Paranal (Fuchs 1995) and Mauna Kea (Olivier & Gavel 1994), figure reproduced from Sarazin (1995), b) the South Pole for the 15 microthermal balloon flights



**Figure 4.9:**  $C_N^2$  (blue),  $|dU/dz|$  (yellow) and potential temperature (red) profiles for a) 23 June ( $\epsilon_{fa} = 0.24''$ ) and b) 02 July ( $\epsilon_{fa} = 0.42''$ )

Muñoz (1994). Fig. 4.10 is a magnified view of the region from 7–9 km, which appears to contain a number of such regions. The effect is caused by a wide region of wind shear, which mixes the already smoothly increasing  $\theta$  profile so thoroughly as to become almost isothermal (i.e.  $|d\theta/dz| = 0$ ). As a result, the optical turbulence drops to a very low value, despite the strong wind shear. At the upper and lower boundaries, however, the potential temperature peaks sharply, as it must in order to regain the overall smooth average gradient. It is at these two points that sharp peaks in  $C_N^2$  are generated, as can be seen in the figure. These narrow layers, no more than a few tens of metres thick, account for the majority of the overall free atmosphere seeing contribution.

The characteristic layers appear to repeat in this flight with a period of  $\sim 100$  m. They appear to be related to the classic “shear waves” observed elsewhere (McIlveen 1992), arising from Kelvin-Helmholtz instability in the shear layers strong enough to overcome the static stability of the smoothly positive potential temperature gradient (Coulman 1985).

Further interpretation of these shear layers will not be given here. They do appear, to some degree, in all of the data with well above average free atmosphere seeing, however, and are the dominant factor in this component of the seeing on these occasions. It would therefore be very useful to be able to predict their occurrence in advance. A quantity often used to define the criteria for the development of wind shear-generated turbulence is the Richardson number,  $R_i$ :

$$R_i = \frac{g}{\theta} \frac{(d\theta/dz)}{(d\bar{U}/dz)^2} < \frac{1}{4} \quad (4.2)$$

$R_i$  was calculated for all flights, and while it holds for the lower-boundary layer as a whole, it does not really identify the intense individual peaks responsible for most of the seeing. It does, on the other hand, appear to be a much more useful parameter for describing the turbulence in the free atmosphere. Fig. 4.11 shows the  $C_N^2$  data for the flight analysed above, along with the  $R_i$  profile (inverted, to show any correlations more clearly), calculated from the wind velocity and temperature measurements at each 5 m standard level. The most intense  $C_N^2$  peaks at the borders of the shear layers do seem to agree quite well with the theoretical critical

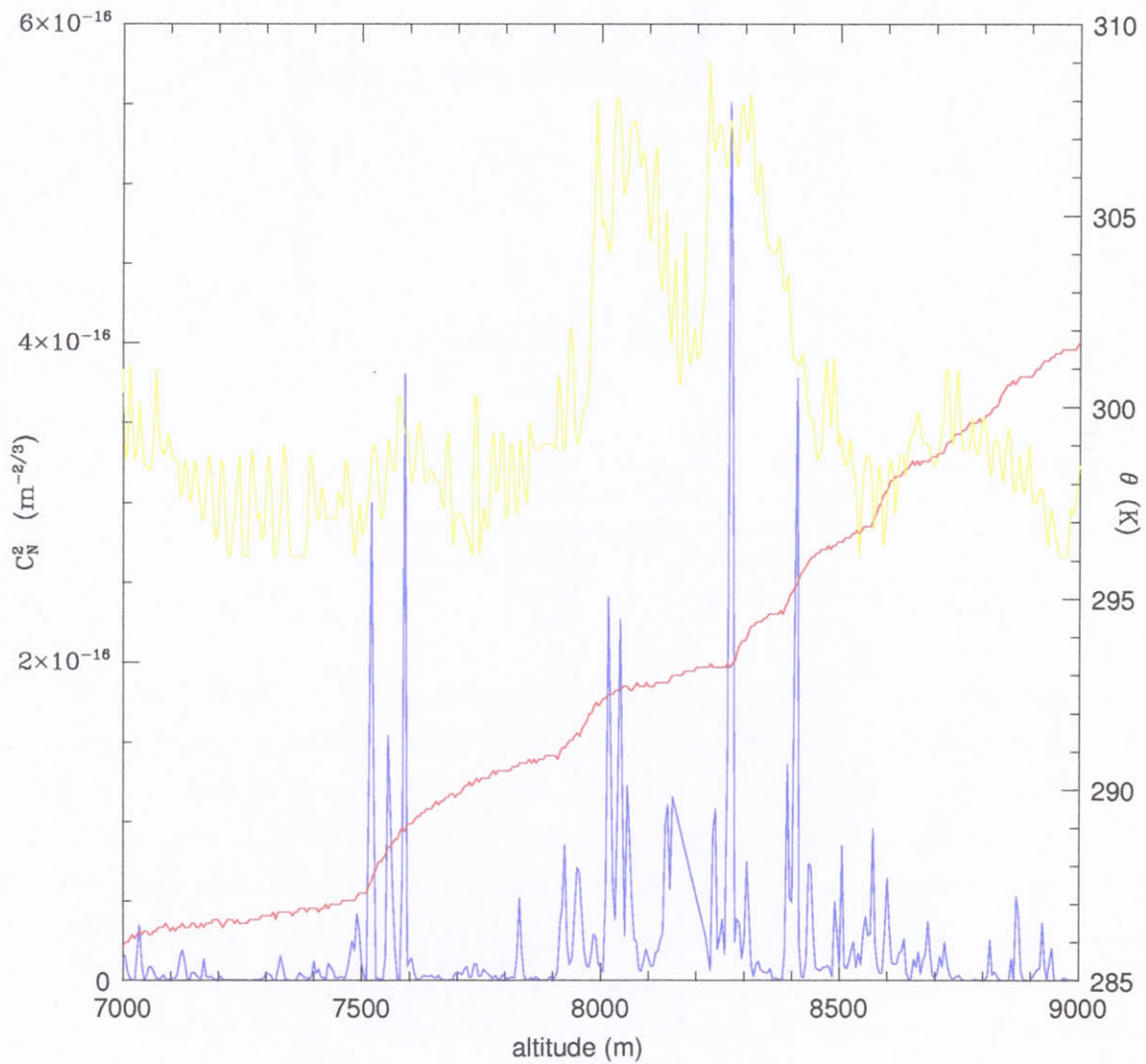


**Figure 4.10:** Same as Fig. 4.9(b), restricted to the region from 7–9 km altitude, showing the  $|\frac{d\theta}{dz}|$  and  $|\frac{dU}{dz}|$  disturbances responsible for the peaks in turbulence.

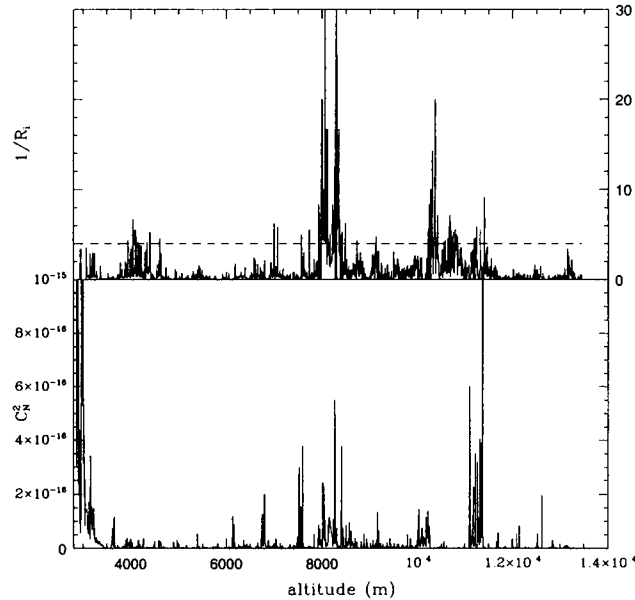


**Figure 4.11:** A comparison of  $C_N^2$  and  $R_i$  profiles for 02/07/95 (the same flight shown in Fig. 4.9(b)).  $1/R_i$  is plotted to show more clearly the regions of instability: any peaks above the dashed line satisfy  $R_i < 1/4$ . The integrated seeing values calculated for this flight were:  $\epsilon_{\text{tot.}} = 0.83''$ ,  $\epsilon_{\text{FA}} = 0.42''$ .

value of 0.25 for  $R_i$ . This is generally the case for the other flights containing some strong “shear wave”  $C_N^2$  peaks as well; conversely, the best free atmosphere flights ( $\epsilon_{\text{FA}} = 0.23\text{--}0.26''$ ) contain almost no  $1/R_i$  peaks.

The fact that  $R_i$  would seem to be a reasonable indicator of relatively strong upper-air turbulence in the atmosphere at the South Pole is further evidence that it may be possible to determine the frequency of very good free atmosphere seeing at the site by analysis of historic and ongoing meteorological records, as a follow-up to the results presented here. The importance of this is that if, in practice, it is possible to correct for the boundary layer turbulence by the use of adaptive optics (see Sect. 4.4), then the free atmosphere component of the seeing will be the limiting factor in large telescope image resolution at the site. One could then hope to forecast, or at least “nowcast” (Murtagh & Sarazin 1993, 1995), seeing conditions in terms of just a few parameters easily obtainable from standard balloon launches

performed daily by the Meteorology Department. The infrequent formation of the shear layers described above could perhaps be reported some time in advance, depending on their typical lifetime, and then be used to generate an approximate value for the upper atmosphere seeing at that time.

As will be discussed in Sect. 4.4, the concentration of the bulk of the seeing in the lower-boundary layer means that a low-order, or turbulence conjugated, adaptive optics system should be able to remove the large majority of the seeing over very wide angles. The small free atmosphere component would remain uncorrected in this scenario, and hence the possibility of predicting the rare occurrences of 0.4–0.5'' free atmosphere seeing would be very helpful.

#### 4.2.4 H-DIMM observations

Seeing measurements were also taken during this season with a “Hartmann” Differential Image Motion Monitor (H-DIMM) (Bally et al. 1996, Loewenstein et al. 1998). This instrument is the same in principle as the standard DIMM used over the past several years in site-testing measurements around the world (Sarazin & Roddier 1990). The DIMM consists of a pair of small apertures placed in front of a telescope. A bright star is imaged at a very rapid frame rate, ( $\sim 100\text{Hz}$ ); fast enough to “freeze” the motion of the images in the focal plane due to atmospheric seeing. The amplitude of the differential motion between the two images can be used to derive values for  $r_0$  and  $\epsilon_{\text{fwhm}}$ .

The H-DIMM uses instead a multiple-aperture mask — in the case of the 60 cm SPIREX telescope, 48 apertures were used, giving a total of 36 different pairs having the smallest separation, as well as a multitude of other combinations. This arrangement provides multiple redundancy in the measurements, to the point of being able to detect localised effects, for example, within the telescope tube itself. The data also contains information about the horizontal wind speed and, indirectly, the altitude of the most intense turbulent layers. Cross-correlations of the magnitude of differential motions across the array of aperture pairs, separated in time by one or more frames, can potentially be used in conjunction with available wind data to determine the height and intensity of the strongest turbulent layers. These studies are not directly relevant to this thesis; they are mentioned simply as an interesting possibility in terms of obtaining some information about the vertical turbulence structure at another site, in the absence of microthermal profiles. Such

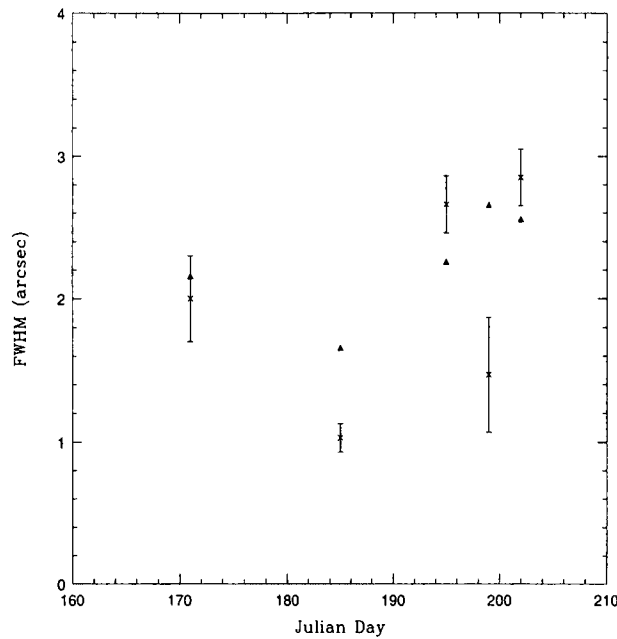


**Figure 4.12:** Comparison of H-DIMM (triangles) and microthermal (crosses) seeing measurements on the five occasions that the two experiments were performed simultaneously, from 23 June to 21 July, 1995. The error bars derive from the uncertainty in the  $C_N^2$  values from 0–40 m.

an experiment is proposed as part of the AASTO project (Storey et al. 1995, Dopita et al. 1996).

The only direct use for the data here is for comparison with the integrated seeing values obtained by the microthermal sondes. H-DIMM data were taken almost simultaneously with microthermal balloon launches on five occasions during the winter, with the results compared in Fig. 4.12. The correlation is reasonably good for three of the runs, however the H-DIMM gives a much larger result than the microthermal data during the other two. Discrepancies of this magnitude are worrying, however it seems that the explanation lies in the fact that an internal heater was inadvertently left running in the telescope tube during many of the H-DIMM observations throughout the year, which would obviously increase the image motion artificially. Although efforts were made at the reduction stage to try to minimise this effect, by removing the data from the most badly affected areas of the mask image, it is very likely that some effect is present over the entire area, which would be most noticeable during periods of relatively low seeing, as is the case for the two runs shown in the figure.

## 4.3 Comparison with other sites

### 4.3.1 Overview

The results presented here, from both the surface layer and free atmosphere parts of the experiment, present a sharp contrast with the seeing characteristics of all other terrestrial sites. The seeing from surface level is clearly quite poor a large proportion of the time, at least in comparison with the very best observatory sites currently in use.

However, it has been shown here that over 90% of the refractive index fluctuations responsible for the seeing at the South Pole are caused by an intensely turbulent boundary layer extending up to an altitude of only 200 m or so. This is in contrast to other sites, where boundary layer effects extend to a much greater height, and account for a much smaller proportion of the total seeing. Free atmosphere effects contribute substantially to the seeing at many other sites, whereas the free atmosphere above the South Pole is very quiescent.

Table 4.2 compares the seeing characteristics of the atmosphere above the South Pole with a selection of measurements from some of the world's leading observatory sites, all of which claim average seeing from ground level in the sub-arcsecond range. At the sites in Chile and the Canary Islands, boundary layer effects extend to around 1–2 km above the surface, and account for some 60–70% of the total integrated seeing. Atop Mauna Kea, on the other hand, at an altitude of 4200 m, the observatory is high enough to avoid the influence of a conventional terrestrial boundary layer; this region only contributes 0.28'' to the integrated seeing.

The stated values for the free atmosphere contribution are similar for almost all of these sites, including the South Pole. Again, the exception is Mauna Kea ( $\epsilon_{\text{FA}} = 0.46''$ ), which tends to suffer from a relatively intense turbulent region at an altitude of about 10 km (above sea level), produced by strong wind-shears due to jetstreams at the upper boundary of the troposphere.

The comparisons made here with the South Pole are not quite accurate, however, in the sense that the figures quoted for the free atmosphere contribution begin at the top of the boundary layer for each site. Since the the South Pole boundary layer extends to a height of only 200 m or so, the 0.37'' of free atmosphere seeing includes the region from 200–2000 m that is included in the boundary layer at most other sites. The average contribution from the atmosphere above 2000 m at the

Site	Alt. [m]	Total seeing ["]	FA seeing ["]	BL seeing ["]	SL seeing/ range [" , m]	BL height [m]
South Pole	2835	1.86	0.37	1.78	0.64, 27	220
Cerro Paranal, Chile	2500	0.64 (med.) 0.73	– 0.4	– 0.55	– –	– 2000
La Silla, Chile	2400	0.97 0.87	0.31 –	0.85 –	0.15, 30 –	800–1000 –
Mauna Kea, Hawaii	4200	0.57	0.46	0.28	–	–
La Palma, Canary Is.	2100	0.96	0.40	0.73	0.07, 12	1–2000

**Table 4.2:** Comparison of seeing conditions at the South Pole and some of the world's major observatory sites. FA, BL and SL refer to the free atmosphere, boundary layer and surface layer, respectively. References – South Pole: Marks et al. 1996, 1999 – Cerro Paranal, Chile: Murtagh & Sarazin 1993 Fuchs 1995 – La Silla, Chile: ESO-VLT working group 1987 Murtagh & Sarazin 1993 – Mauna Kea, Hawaii: Roddier et al. 1990 – La Palma, Canary Is.: Vernin & Tuñon-Muñoz 1992, 1994

South Pole is  $< 0.3''$ . Conversely, the contribution from the atmosphere beginning from an altitude of 200 m at the mid-latitude sites is still a large fraction of the ground level seeing. In particular, at Cerro Paranal, a site with which a detailed comparison has been made (see next section),  $\epsilon_{200+} = 0.6''$  or so.

To summarise these results, the microthermal turbulence at the South Pole is concentrated much closer to the surface than at the best mid-latitude sites — the locations of some of the world's largest telescopes. So, while the integrated seeing from surface level does not compete, the free atmosphere is quieter than the other sites, with the result that the seeing contribution above about 200 m (the depth of the South Pole boundary layer) is significantly less than any other site.

### 4.3.2 Comparison of microthermal measurements at the South Pole and Cerro Paranal

The problem with comparing the seeing quality between different sites is that different methods are often used to obtain the results. This inevitably leads to

some doubts about calibration, and hence the validity of any conclusions drawn. The availability of measurements from a set of microthermal balloon sondes over the ESO-VLT site at Cerro Paranal, Northern Chile (Fuchs 1995) enables a direct comparison of the  $C_N^2$  profiles at each of these two sites. The results clearly illustrate the points made in the preceding section regarding the seeing contributions from different regions of the atmosphere at the various sites. This comparison is shown in Fig. 4.13, as a plot of the integrated seeing against the height of a hypothetical telescope above the surface. It is obtained by increasing the lower limit of the integral in Eq. 2.6 in 5 m increments, using the average  $C_N^2$  profile shown in Fig. 4.3.

All of the main features discussed previously can be seen very clearly in the South Pole curve; the optical turbulence falls just above the surface, up to an altitude of about 120 m, then decreases more gradually up to 200 m, beyond which the remaining seeing contribution is very small, and decreases smoothly with altitude.

The plot for the Cerro Paranal data, based on the average  $C_N^2$  profile over thirteen balloon flights, is derived using the same method. Paranal is clearly a much better site from surface level, with average seeing of around  $0.7''$ , but since the optical turbulence at the South Pole is concentrated so close to the surface, it drops below the Paranal curve very quickly. The cross-over point is at about 90 m,  $\varepsilon_{\text{fwhm}} \sim 0.65''$ . Above 200 m at the South Pole, beyond the boundary layer seeing, the contribution is about 60% of the corresponding value calculated from the Paranal data.

The actual average  $C_N^2$  values (Fig. 4.3(a & b)) also show the contrast between the two sites very clearly. The turbulence at the South Pole drops sharply at around 200 m, and continues at around the same level or just below the Paranal curve for the remainder of the atmosphere, and in particular the region up to about 2 km. In addition, a small, but still significant, increase in  $C_N^2$  is noted at Paranal at a height of about 12–15 km, associated with the tropopause. This is absent at the South Pole, and does add an extra margin of some  $0.05\text{--}0.1''$  to the difference in free atmosphere seeing between the sites, as indicated in Table 4.2.

### 4.3.3 $C_N^2$ profiles at other sites

A good summary of measurements ranging from 0–1200 m above the surface at several different sites is provided in Gur'yanov et al. (1988), shown in Fig. 4.14.

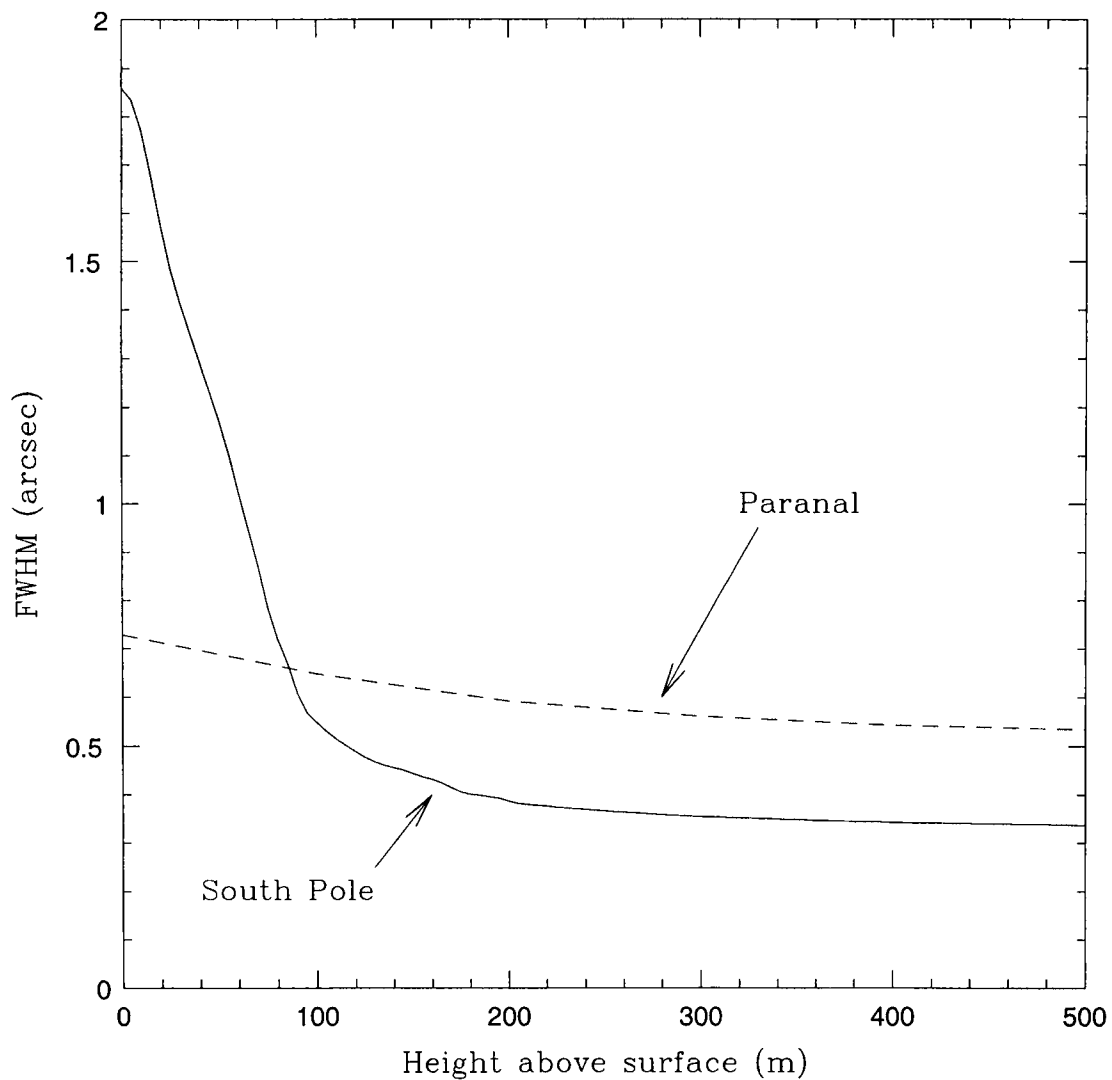


**Figure 4.13:** Seeing as a function of height of the telescope above the surface. The solid line represents average results from our launches at the South Pole, while the dashed line is a summary of a similar experiment performed at the ESO-VLT site at Cerro Paranal, northern Chile (Fuchs 1995) in May 1993, averaged over 13 flights.

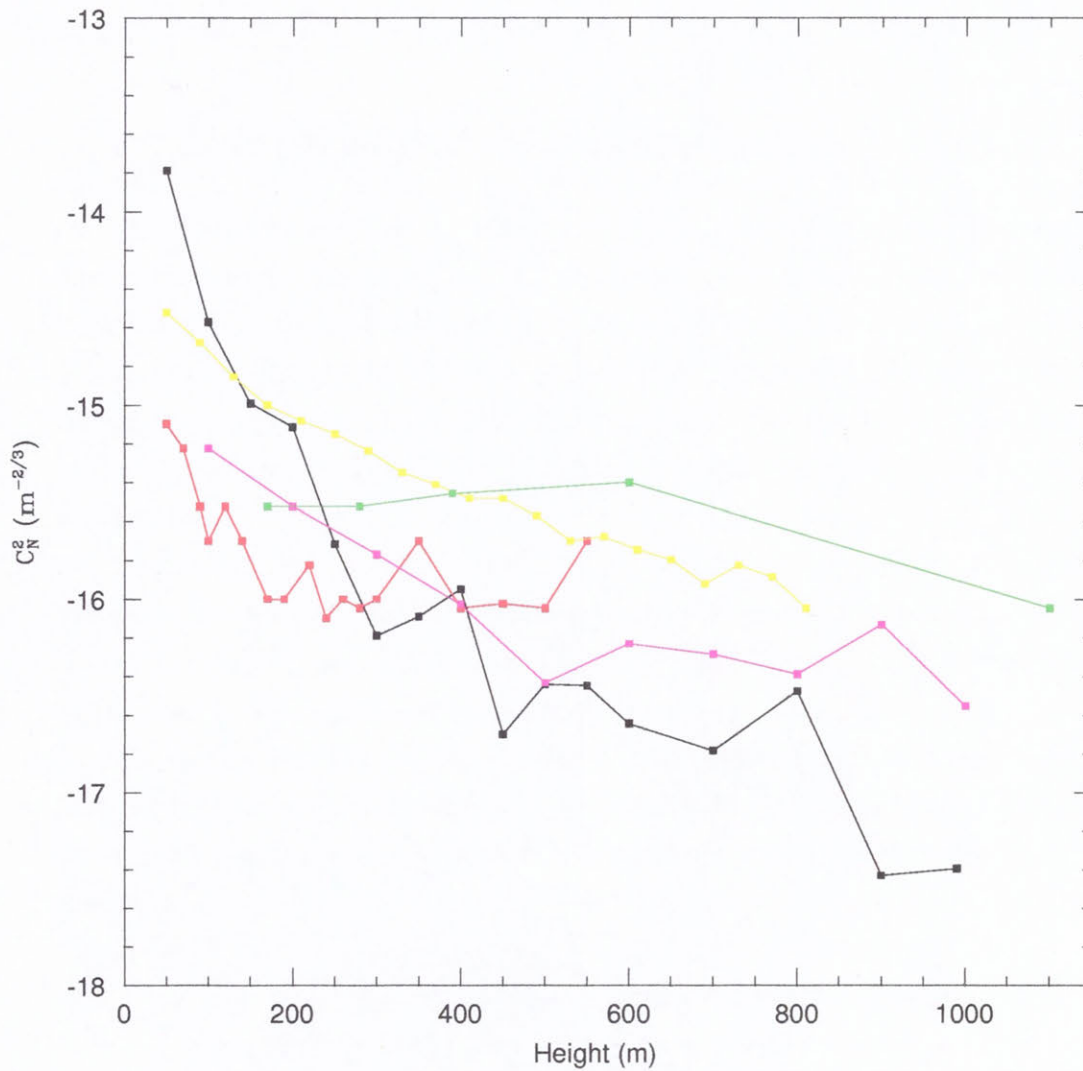


**Figure 4.14:** Comparison with the  $C_N^2$  profile at the South Pole up to 1000 m (black) with mid-latitude sites: Special Astrophysical Observatory, Mt. Pastukhov (red), Mt. Maidanak, Uzbekistan (green), (both Gur'yanov et al. 1988); La Silla, Chile (yellow), (ESO-VLT working group 1987); Cerro Paranal (magenta) (Fuchs 1995)

It includes mountaintop sites in Uzbekistan, Tadzhikistan and Russia, as well as Mt. Graham in mainland USA, and Mauna Kea in Hawaii. For almost all of these sites, there appears to be a moderately active boundary layer extending well beyond 1 km in altitude, as is the case at Cerro Paranal. The South Pole profile dips below most of them in the 100–500 m range. The integrated seeing is once again lower at the South Pole from about 200 m, by comparison to other profiles in Fig. 4.14. The  $C_N^2$  profile at Mauna Kea is much lower in the boundary layer, however, as discussed previously, this site suffers more from upper atmosphere disturbances.

## 4.4 Adaptive optics parameters

There are two obvious approaches to capitalising on the excellent seeing at the South Pole above the strong optical turbulence that extends up to 100–200 m. One solution might be to build some sort of raised platform or tower to elevate the telescope to a height of 200 m or so. Without discussing the feasibility of such an engineering project here, the concentration of the optical turbulence near the surface is also an exceptionally promising scenario for the use of adaptive optics techniques.

The measured  $C_N^2$  profiles can be used to calculate directly several spatial and temporal parameters that characterise the potential for adaptive optics at the site. These parameters are well-known and widely used, and comparisons are available with some of the sites mentioned above.

The values used are slightly different for the two common techniques of adaptive optics (AO) and speckle interferometry (SI) (Vernin & Tuñon-Muñoz 1994, Roddier et al. 1982), and may be obtained following the derivation of Roddier (1981). Using the notation:

$$C(x, \eta) = \int_{h_0}^{\infty} x^\eta(h) C_N^2(h) dh, \quad C(0) = \int C_N^2(h) dh \quad (4.3)$$

these quantities are given by Eqs. 4.4–4.8. The subscripts AO and SI refer to adaptive optics and speckle interferometry respectively.

*Isoplanatic patch:*

$$\theta_{\text{AO}} = 0.31r_0 \left( \frac{\mathcal{C}(h, 5/3)}{\mathcal{C}(0)} \right)^{-3/5} \quad (4.4)$$

$$\theta_{\text{SI}} = 0.36r_0 \left( \frac{\mathcal{C}(h, 2)}{\mathcal{C}(0)} - \left( \frac{\mathcal{C}(h, 1)}{\mathcal{C}(0)} \right)^2 \right)^{-1/2} \quad (4.5)$$

*Coherence time:*

$$\tau_{\text{AO}} = 0.31r_0 \left( \frac{\mathcal{C}(U, 5/3)}{\mathcal{C}(0)} \right)^{-3/5} \quad (4.6)$$

$$\tau_{\text{SI}} = 0.36r_0 \left( \frac{\mathcal{C}(U, 2)}{\mathcal{C}(0)} - \left( \frac{\mathcal{C}(U, 1)}{\mathcal{C}(0)} \right)^2 \right)^{-1/2} \quad (4.7)$$

*Scintillation index:*

$$\sigma_{\text{I}}^2 = 19.12\lambda^{-7/6}\mathcal{C}(h, 5/6) \quad (4.8)$$

#### 4.4.1 Angular and temporal isoplanatism

The spatial and temporal characteristics of the distorted wavefront at the aperture of a telescope caused by the seeing depends upon the altitude and intensity of the turbulent layers. Clearly, with the assumption that all turbulent layers have a very similar appearance and (Kolmogorovian) power spectrum, the higher altitude layers produce wavefront errors on a smaller angular scale than layers close to the telescope.

Real-time image correction methods, in which optical components are adjusted on a short enough time scale to cancel out the rapid, random image wander caused by the atmospheric turbulence, require the presence of a relatively bright reference star close to the source of interest so that the wavefront fluctuations are essentially the same for both sources, and hence the seeing may, in principle, be fully removed by making adjustments to the optics based in the motion of the guide star. The area around the reference star within which the corrections are valid is referred to as the *isoplanatic patch*, with an associated radial angle,  $\theta$ , which depends on the altitude distribution of the turbulent cells along the line of sight, according to Eq. 4.4 or 4.5.

Image reconstruction also depends on temporal isoplanatism — the maximum

integration time for which a given correction remains accurate before the wavefront phase angle changes. In general, turbulence cells evolve slowly enough that they can be considered to be static in the time it takes for them to move across the telescope aperture, and so the *coherence time*,  $\tau$ , depends on the wind speed, according to Eqs. 4.6–4.7. A large value of  $\tau$  allows longer integrations, which means that fainter guide stars can be used, thus increasing the number density of potential guide stars on the sky, and therefore increasing the probability that a suitable guide star will be found within range of the target source.

These parameters quantify the practical limits for the application of image correction methods at a particular site. With low values of  $\theta$  and  $\tau$ , relatively complex systems must be used in order to obtain any improvement in image resolution. Given the turbulence profiles measured by the microthermal probes at the South Pole, we might expect that this should be a better site in terms of these parameters. In particular, the isoplanatic angle should be wider, due to the concentration of turbulence close to the surface, despite the fact that the wavefront fluctuations are more intense.

Values of  $\theta$  and  $\tau$  were calculated for each of the the South Pole balloon flights, integrated over the entire atmosphere, and the results are shown in Table 4.3, compared with quoted values for La Palma and calculated values from the available  $C_N^2$  data from Cerro Paranal. Apart from  $\tau_{AO}$ , the results for the South Pole data are certainly somewhat better than the other sites, especially in the best observing conditions. The improvements are minor, however, and remain in the region of a few arcseconds and milliseconds. The benefit is not substantial enough to be of any practical significance.

Clearly the tight limitations on  $\theta$  and  $\tau$  mean that the ideal of perfect image correction of turbulence-distorted images is extremely difficult to achieve at any site, including the South Pole. A large number of independent sub-mirrors is required to correct the wavefront errors over the full field of view of the telescope. The strategy at other sites has generally been to settle for varying degrees of partial image correction, usually by ignoring the higher orders of the perturbations of the wavefront, and thus making the corrections applicable over a larger area. The aim is to make the maximum gains possible in image quality with a relatively simple and inexpensive system such as a tip-tilt mirror (i.e. first-order corrections). Evidently, the maximum “reconstruction angle” (the term coined by Cowie & Songaila (1988))

	South Pole <i>total</i>	South Pole <i>B.L. correction</i>	Cerro Paranal	La Palma	La Silla
$\theta_{AO}$ ["]					
mean	3.23	65.35	2.41	1.30	–
best	6.50	–	4.1	1.62	–
$\theta_{SI}$ ["]					
mean	2.76	118.22	4.45	2.18	2.59
best	5.17	–	4.8	2.66	4.49
$\tau_{AO}$ [ms]					
mean	1.58	1.62	5.6	6.64	–
best	6.09	–	14.5	9.60	–
$\tau_{SI}$ [ms]					
mean	17.34	17.81	10.1	12.88	12.2
best	35.04	–	20.5	19.52	17.5
$\sigma_I^2$					
mean	0.070	–	0.16	–	–
best	0.033	–	–	–	–

**Table 4.3:** Summary of the calculated values of the astrophysical parameters defined in Eqs. 4.4–4.8, based on the 15 balloon flights. The limit of the boundary layer is taken to be 220 m. Values for Cerro Paranal were obtained using the average  $C_N^2$  profiles measured at this site (Fuchs 1995); for La Palma from (Vernin & Tuñon-Muñoz 1994); for La Silla from (ESO-VLT working group 1987)

depends on the precision required in the corrections, and there is a trade-off between image quality and sky coverage.

These ideas are particularly important in relation to the situation at the South Pole, since, as noted earlier, high-altitude turbulence has a higher spatial frequency, when viewed from ground-level, than turbulence close to the surface. We may expect, therefore, that a low-order adaptive optics system that corrects the boundary layer component of the seeing, leaving the upper atmosphere uncorrected, would be effective over a substantially greater area of the sky at the South Pole than a similar system operating at the best mid-latitude sites, due to the concentration of optical turbulence nearer the surface. A glance at Fig. 4.13 indicates that image resolution of 0.2–0.3" should be obtainable over these larger angles.

In order to quantify these ideas, a simple approximation was made, in which partial-image correction angles were calculated by applying upper limits,  $h_u$ , to the integral in Eqs. (4.4–4.5). The degree of correction associated with these angles is specified by a residual seeing component  $\varepsilon_r$ , determined simply by setting  $h_u = h_0$

in Eq. 2.6, and using the values already calculated in Fig. 4.13. In other words,  $\varepsilon_r$  includes the seeing due to the atmosphere from  $h_u \rightarrow \infty$ , and will increase as  $h_u$  is reduced.

As expected, the reconstruction angles calculated in this way become very large for corrections limited to the boundary layer. The values of  $\theta_{\text{AO/SI}}$  increase by a factor of 30–40 for  $h_u = 220$  m, as shown in Table 4.3. Fig. 4.15 illustrates the range of possible combinations of  $\theta$  and  $\varepsilon_r$  that are possible, compared, once again, with Cerro Paranal. The difference between the sites can be seen very clearly, for partial image correction at the level of  $\varepsilon_r > 0.25''$  or so.

Although no vertical  $C_N^2$  profiles were available from other mid-latitude sites for a direct comparison, the result should be much the same, considering Fig. 4.14 and the discussion of Sect. 4.3. It may be even more favourable in comparison with Mauna Kea, where a much greater proportion of the seeing is due to upper atmosphere turbulence.

It is also possible to quantify the improvement in sky coverage that would be associated with these increased partial correction angles. This can be done by determining the probability of finding an appropriate guide star of magnitude  $m_v$  within an angle  $\theta$ , at Galactic latitude  $b$  (Olivier 1993):

$$P_{\text{sky}} = 1 - \exp[-\pi\theta^2\Sigma(m_v, b)] \quad (4.9)$$

where  $\Sigma(m_v, b)$  is the number density of stars of a given  $m_v$  and  $b$ . Values of  $\Sigma(m_v, b)$  are tabulated in various astronomical data books (e.g. Allen (1973)).

Combining Eq. 4.9 with Fig. 4.15 gives the relationship between  $P_{\text{sky}}$  and  $\varepsilon_r$  shown in Fig. 4.16, using values of  $m_v$  averaged over all Galactic latitudes. Sky coverage at the South Pole is up to around 50–80% at the  $\varepsilon_r = 0.3''$  level, for reference sources in the range  $m_v = 14$ –16, decreasing somewhat at the bright end in the adaptive optics case. By contrast, only around 1–2% of the sky is covered at Cerro Paranal for  $\varepsilon_r = 0.3''$ ; good sky coverage at this site is only possible for  $\varepsilon_r \sim 0.5''$ , which is not a great deal better than the natural seeing. The difference between the sites is clearly illustrated in this example. Overall, the lower-boundary layer component of the seeing at the South Pole is much more readily corrected than the more even vertical distribution of turbulence seen at Cerro Paranal, over a large fraction of the sky, and with an acceptable level of image resolution.

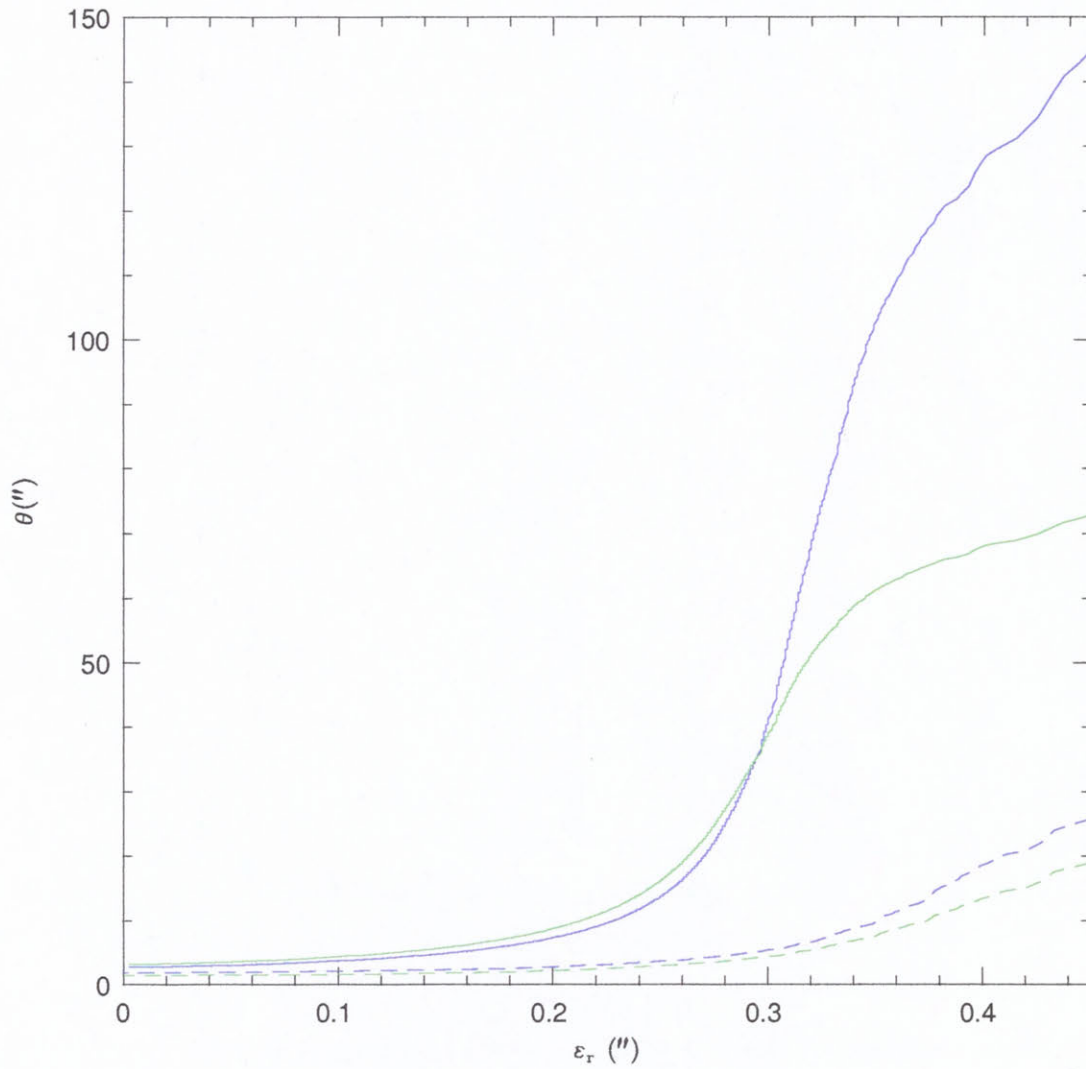


**Figure 4.15:**  $\theta_{\text{AO/SI}}$ , as a function of the residual seeing  $\varepsilon_r$ . Solid lines are derived from the average  $C_N^2$  profiles at the South Pole, and the dashed lines from the Cerro Paranal data. The curves are obtained by varying the upper and lower limits of Eqs. 4.4–4.5 and Eq. 2.6, respectively. The value of  $\theta$  for  $\varepsilon = 0$  is the isoplanatic angle.

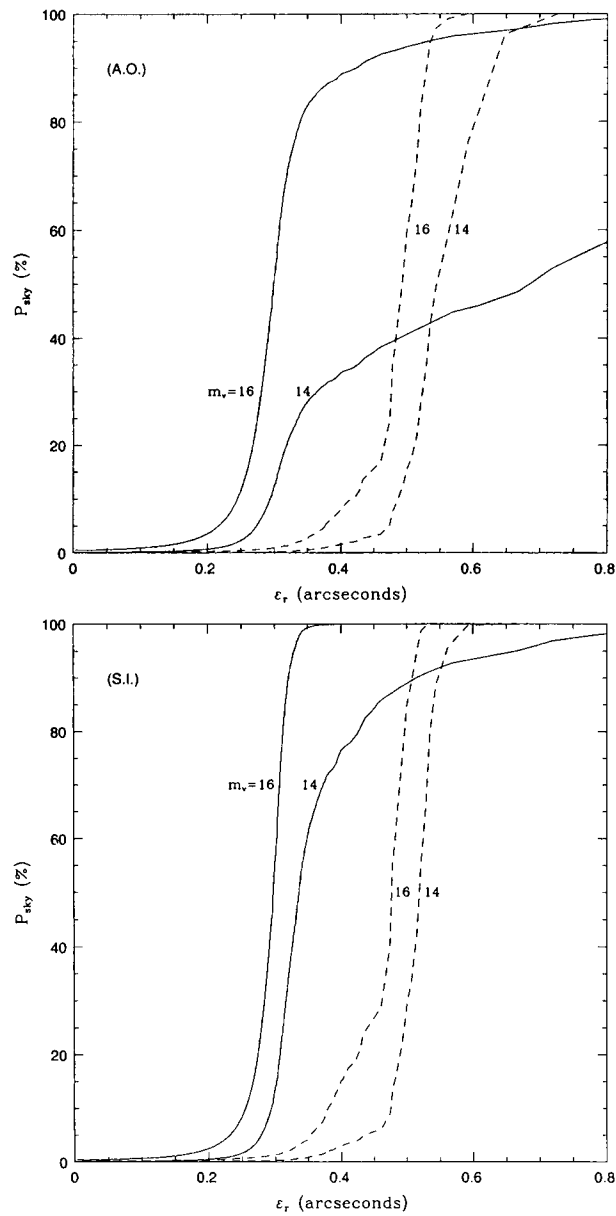


**Figure 4.16:** Percentage sky coverage as a function of the residual seeing, for a) adaptive optics and b) speckle interferometry, in the visual magnitude range  $m_v = 14-16$ . Solid lines show the results for the South Pole; dashed lines for Cerro Paranal. Calculations are averaged over all Galactic latitudes.

As noted above, this analysis is somewhat contrived in the sense that it uses partial corrections obtained by removing the effects of particular turbulent layers according to altitude. This is not a realistic situation, but rather, it is necessary to consider the effects of the high and low-frequency components of the power spectrum of the resultant wavefront at the aperture. The analogy remains valid qualitatively in the sense that the high frequency part of the power spectrum is due predominantly to upper atmosphere turbulence. Hence, the results described here give a reasonably accurate indication of the potential for partial-correction adaptive optics or speckle interferometry at the two sites.

It should also be noted that the calculations here use an average stellar number density; within  $10^\circ$  or so of the Galactic plane the achievable image quality increases by about  $0.05''$  for the same sky coverage, due to the greater number of stars in this part of the sky.

As mentioned above, adaptive optics systems have been employed at other sites around the world, in which partial corrections are sought by relaxing the requirement of full isoplanicity at high frequencies. Cowie & Songaila (1988) were able to achieve a image resolution of around  $0.3''$  at Mauna Kea over angles of up to  $30''$  (a factor of 5–6 greater than the isoplanatic angle at the site). Olivier (1993) obtained similar results using a slightly different method, and there have been other experiments making similar claims. While the treatment here is quite simple, aimed as it is at illustrating the potential of the South Pole in broad terms, some of the detailed studies of low-order image correction do indicate that the possible gains may be even greater than shown here.

The fundamental point to be made is that the South Pole, with such a high concentration of optical turbulence close to the surface, is by far the best site found to date for any low-order image correction techniques. This is illustrated by the favourable comparison with such a high-quality site as Cerro Paranal.

It is worth also mentioning some of the methods used for correction of higher-order components of the wavefront phase fluctuation. With a characteristic coherence length of  $r_0$ , the number of independent elements required for full image correction is on the order of  $(D/r_0)^2$ , for corrections made in planes conjugate to the telescope aperture. As discussed above, such a project is not expected to be any easier at the South Pole than other sites.

Another method that has been investigated is “turbulence conjugation” (Roddier 1981, Parenti 1992). Calculations of the relative performance of aperture and

turbulence conjugation have been performed by Wilson & Jenkins (1996), with the result that the turbulence conjugation case produces increases in sky coverage of a factor of 2–3, at the same level of image correction. In practice, of course, this would be heavily dependant on the vertical turbulence profile.

A “multiconjugate” approach (e.g. Tallon et al. 1992) requires, in principle, a single correction element for each turbulent layer, which, at any site, is likely to result in a less complex system than the usual aperture-conjugated case. It is a particularly powerful method in situations where the bulk of the image degradation is produced by a small number of turbulent layers. This is clearly the case at the South Pole, where the boundary layer seeing usually consists of 2–4 intense layers, with a similar number, or less, of much weaker layers in the free atmosphere. It is likely, therefore, that the South Pole represents a particularly good site for higher-order corrections using such a technique.

#### 4.4.2 Scintillation index

Atmospheric turbulence also causes fluctuations in the amplitude of the signal from a celestial source. These variations are a limiting factor in observations in which the flux of a source is important; for example, studies of variable stars and astroseismology. The magnitude of these fluctuations is described by the *scintillation index*,  $\sigma_I^2$ , which can be derived from the  $C_N^2$  profile above a site according to Eq. 4.8, and is represented as a fraction of the mean brightness. The  $h^{5/6}$  dependence of  $\sigma_I^2$  indicates that, once again, the South Pole should be a very good site for observations of this type.

Calculations of  $\sigma_I^2$  from the measured  $C_N^2$  profiles are summarised in Table 4.3, with the statistical distribution shown in Fig. 4.17. The average value of  $\sigma_I^2 = 0.07$  is about 40% of that derived from the Cerro Paranal data ( $\sigma_I^2 = 0.16$ ), which, again, is itself among the best conditions measured at a mid-latitude site (Roddier et al. 1982, Vernin et al. 1991). Hence the high antarctic plateau is also an exceptional site for accurate observations of the types mentioned above.

### 4.5 IR results

Optical astronomy is not likely to be seriously pursued in Antarctica, due to the relatively small amount of astronomical dark time and the (as yet unquantified)

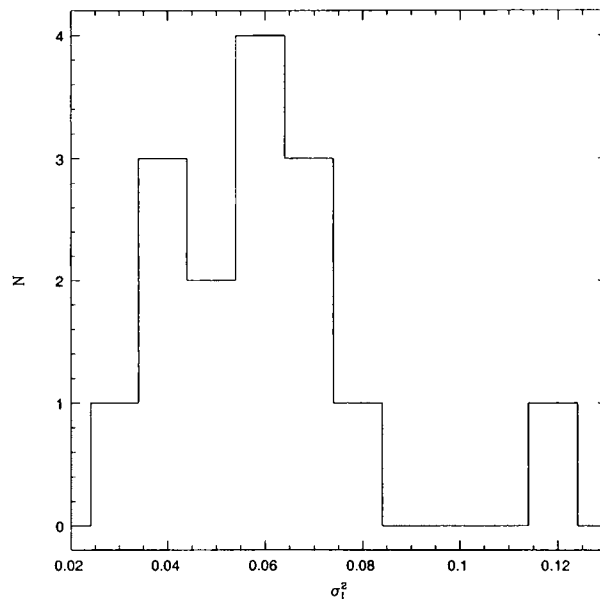


**Figure 4.17:** Distribution of the value of  $\sigma_1^2$  calculated for each of the fifteen balloon flights. The highest measured value,  $\sigma_1^2 = 0.118$ , is statistically more than  $3\sigma$  above the mean, and the  $C_N^2$  data from this flight were omitted when calculating the average value shown in Table 4.3.

effect of auroral activity. The focus, rather, will be on the infrared and longer wavelengths, for the reasons described in Ch. 1. Hence, it is worth looking at the seeing results converted to a more directly relevant wavelength, using Eqs. 2.8–2.9. A wavelength of  $2.4 \mu\text{m}$  has been chosen, which is near the short-wavelength end of the waveband where astronomers expect some of the most important gains in Antarctica. It is a very important wavelength since, due to the natural minimum in airglow emission (Ashley et al. 1996), the potential gains over temperate sites are particularly pronounced and it is likely to be strongly targeted in future.

The FWHM seeing and  $r_0$  values at this wavelength are shown in Table 4.4, by analogy with Table 4.1. Fig. 4.18 shows the comparison between the FWHM seeing profiles of the South Pole and Cerro Paranal for this wavelength using the same method as that used to produce Fig. 4.13. Of course, the proportional improvement from above 100–200 m remains the same. Every tenth of an arcsecond is increasingly significant, however, as the seeing reaches very low levels. Here we have the free atmosphere seeing at the South Pole getting down towards  $0.2''$ , while the Paranal curve remains at around the  $0.4''$  range. While the free atmosphere seeing at the South Pole is still about 65% of that at Paranal from the same level, in terms

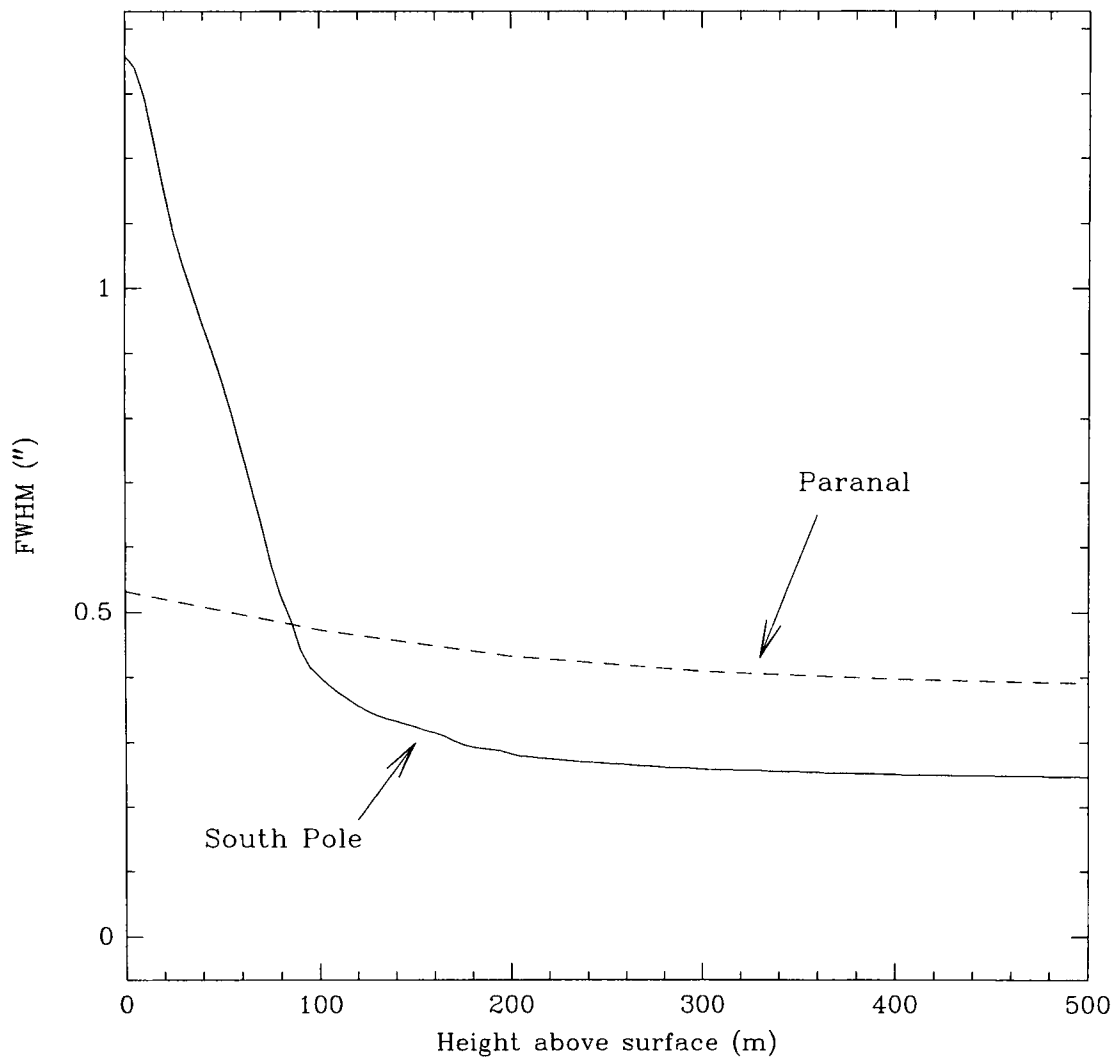


Figure 4.18: South Pole / Paranal seeing comparison (see Fig. 4.13) at  $K=2.4\mu\text{m}$

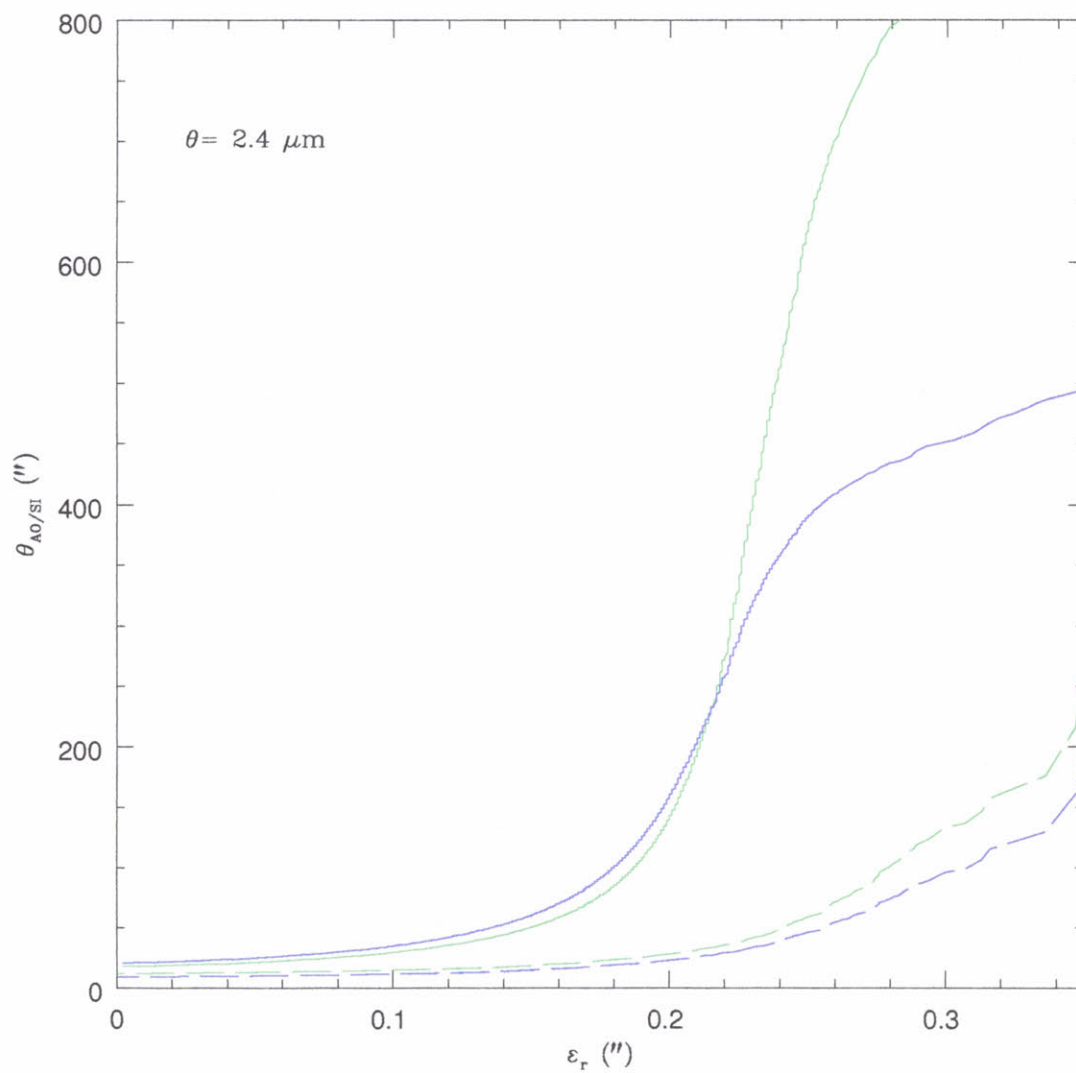


Figure 4.19:  $\theta$  vs  $\varepsilon$  (see Fig. 4.15) for  $K=2.4\mu\text{m}$

Measurement	Mean	Std. Dev.	Median	Best 25%	Best	Worst
Seeing (arcseconds)						
-total	1.36	0.55	1.2	0.7	0.6	2.3
-free atmosphere	0.27	0.05	0.23	0.21	0.17	0.38
$r_0$ (cm)						
-total	36.0	22.3	42.0	65.0	80.8	21.7
-free atmosphere	178.7	47.0	185.1	228.4	292.8	153.3

**Table 4.4:** Summary of integrated seeing and boundary layer data, from 15 balloon launches between 20 June and 18 August 1995. The “free atmosphere” refers to the entire atmosphere excluding the boundary layer. Values are quoted for a wavelength of  $2.4 \mu\text{m}$ .

of the actual values the difference between the sites is probably more notable here than in the visible.

The adaptive optics parameters also register a corresponding improvement, scaling as they do with  $r_0$ . Using Eq. 2.8, assuming a Kolmogorov spectrum, all values in Table 4.3 are increased by a factor of  $(2.4/0.5)^{6/5} = 6.57$ . Hence, the isoplanatic angles,  $\theta_{\text{AO/SI}}$ , over the entire atmosphere, are around 18–20”, while coherence times  $\tau_{\text{AO/SI}}$  increase to 10–100 ms. Angles obtained by the type of boundary layer correction discussed in the previous section increase to very significant values of around 7–12’. This is enough to give close to 100% sky coverage up to at least  $m_{\text{K}} = 10$ .

Even if an optical detector is used for the image correction system, with the same adaptive optics parameters applicable as before, the residual seeing would still be reduced at the IR detector by the wavelength ratio, as described above. The image quality can be determined following the analysis of Sect. 4.4.1. The results are shown in Fig. 4.19.

# Chapter 5

## DISCUSSION

In the broadest sense, the aim of the site-testing campaign is to find the best site for astronomy in Antarctica. Given that the only measurements of site conditions available at this point are from the South Pole, it is important to use the results of this experiment to attempt to draw some conclusions about the likely seeing conditions elsewhere on the high plateau. It is generally agreed that the South Pole is almost certainly not the best site for astronomy in Antarctica. Indeed, the only reason for choosing this location for the experiments conducted so far is that it has been the only place on the plateau that is easily accessible. In any case, the conditions there should provide a good indication of the magnitude of the improvements that might be expected from the very best sites, from infrared to millimetre wavelengths.

The problem with the South Pole in terms of its location on the continent, is that it lies a long way off the central “ridge” that marks the highest elevations on the plateau. The implications of this are quite obvious if we consider the three key words: “high”, “cold” and “dry”. Dome A (82°S, 80°E), at 4200 m, and some 1000 km from the South Pole, is the highest point on the plateau. Although no data are available from Dome A (in fact, it is uncertain whether anyone has ever set foot there), indications from the closest stations are that it should be at least 10°C colder than the South Pole on average. Given the enormous difference between the South Pole and the best mid-latitude sites in the infrared (Ashley et al. 1995, Phillips et al. 1999, Nguyen et al. 1996, Smith & Harper 1998), we might expect substantial reductions again in the thermal background from Dome A. In addition, the thinner atmosphere (~5000 m pressure altitude at the surface) and lower temperature should

	South Pole	Vostok	Plateau	Dome C	Dome A
Years	26(40)	24	3	8	–
Altitude (m)	2835	3488	3625	3280	4200
Latitude (S)	90	78.5	79.2	74.5	82
$\bar{T}$ °C	49.3	55.4(Aug)	56.4(Aug)	50.6	~ 60
$\bar{T}$ °C	59.9(Jul)	68.3	71.4	61.7	–
$\delta T_{BL}$ °C	20	23	~ 20	~ 20	> 25
slope	$1.0 \times 10^{-3}$	$1.3 \times 10^{-3}$	$0.8 \times 10^{-3}$	~ 0	–
$\bar{V}$ ms <sup>-1</sup>	5.8	5.1	–	2.8	~ 0
constancy	0.79	0.81	0.67	0.53	–
calm %	2	1	–	10	–
$V_{\max}$ ms <sup>-1</sup>	24	25	–	16	–
cloud < $\frac{3}{10}$ (winter)	63	56	65	–	–

**Table 5.1:** Comparison of weather parameters at all sites on the high plateau from which information is available. Data on Dome C are taken from Keller et al. (1991, 1993, 1995), values for Plateau and Vostok stations are from Schwerdtfeger (1984)

result in even lower water vapour content than the South Pole, which is already an order of magnitude lower than its nearest mid-latitude rival.

These ideas are widely known by now, and will not be discussed in any detail here. What is less certain, on the other hand, is the quality of the seeing we might expect higher on the plateau. Since the seeing depends on a more complex interplay of atmospheric conditions, it is not as easy to predict any improvements, let alone what the scale of those improvements might be. In this chapter, I will look at the available data from elsewhere in East Antarctica, and compare this with what we have discovered at the South Pole, in an attempt to give some indication of what we might expect to find at the higher elevations.

The paucity of information about atmospheric conditions over East Antarctica make this a difficult task. Reasonably continuous, long-term records of both surface and upper air meteorology parameters are available from only two places: the South Pole and Vostok (of which, only the South Pole continues to maintain a winter crew). These have been supplemented by a few Automatic Weather Stations (AWS), successfully deployed at other locations above 3000 m for periods of a few years at a time, which provide some valuable additional information about surface conditions. Overall, we have access to data from no more than four or five places,

in an area half the size of Australia. Many of the results are discussed in the book of Schwerdtfeger (1984), and it is from this source that much of the weather information used in this Section has been gleaned. Table 5.1 is a summary of all the measurements that could be found that are in some way related to the seeing (in particular, the boundary layer seeing). Some of the numbers quoted are based on no more than a couple of years data, especially from the AWSs, and so any conclusions made here on the basis of those particular figures should be treated with caution.

In Chapter 4, it was shown that the boundary layer seeing at the South Pole is generally intense, but highly variable and critically dependent upon the interplay of the temperature gradient and inversion wind, and in particular, any vertical irregularities that occur. The  $C_N^2$  signal tends to be most intense close to the surface, and above the boundary layer, the free atmosphere is in general exceptionally calm and clear. Whilst no microthermal data are available from any of the sites listed in the table, the climate parameters may offer some clues as to the likely structure of the boundary layer at these sites.

## 5.1 Temperature comparisons

Fig. 5.1 is a contour plot of the intensity of the temperature inversion across Antarctica. On the high plateau, it doesn't change a great deal, with a difference of only a little over  $5^\circ\text{C}$  from the South Pole to Dome A. One factor that does differ from the South Pole to the other sites, however, is diurnal variation. Fig. 5.2 shows the evolution of the temperature gradient in the first 32 m at Plateau Station over a 24 hour period. The depth of the temperature change falls from around  $15^\circ\text{C}$  at night to  $< 5^\circ\text{C}$  during the day.

Although the diurnal changes appear to be mostly restricted to the lowest 10–15 m, according to the data from the South Pole this is probably the most turbulent region in the whole boundary layer. Given that the winds at surface level at a site such as Plateau Station are driven by the inversion, it is likely that these too undergo some diurnal variation. The impact of this on the stability of the boundary layer in terms of turbulence is not clear, but certainly, at mid-latitude sites, it is a general rule that the best seeing is observed later in the evenings, when the boundary layer has stabilised. Such temperature variations are likely to have some minor effect in Antarctica, increasing as the latitude of the site decreases. Since all

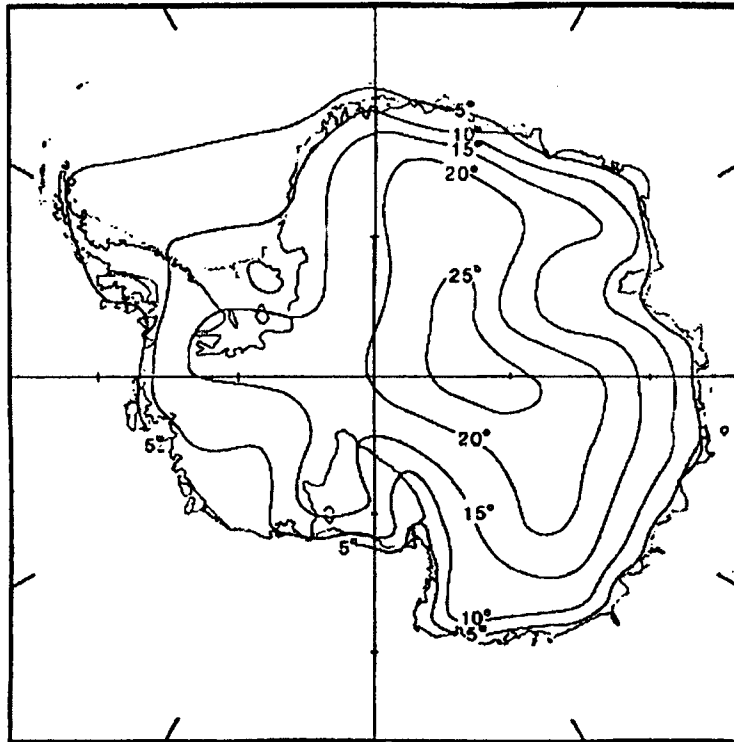


**Figure 5.1:** Contour map of temperature inversion strength over Antarctica ( $^{\circ}\text{C}$ ), taken from Schwerdtfeger (1984)

of the highest sites are south of  $75^{\circ}\text{S}$ , there are at least a few months everywhere during the winter when the sun doesn't rise, and little or no diurnal effects would be noticed during this period.

The increasing strength of the inversion at higher altitudes means that, in fact, the temperature of the warmest layer above the site is very similar from place to place. Comparison of weather balloon data from the South Pole and Vostok show that the temperatures at the 500 hPa level at each station in winter differ by less than a degree, with the South Pole being slightly warmer. The temperature inversion at the South Pole is about 400 m high, according to the temperature data from our microthermal balloon sondes (in terms of  $C_N^2$ , it levels off at about 200–250 m, as discussed in Section 4). While no information is available regarding the vertical extent of the inversion at Vostok, it is likely that it is slightly narrower at the higher altitude site, given that it reaches almost the same temperature at the same pressure altitude. If the temperature layers are to some degree stratified

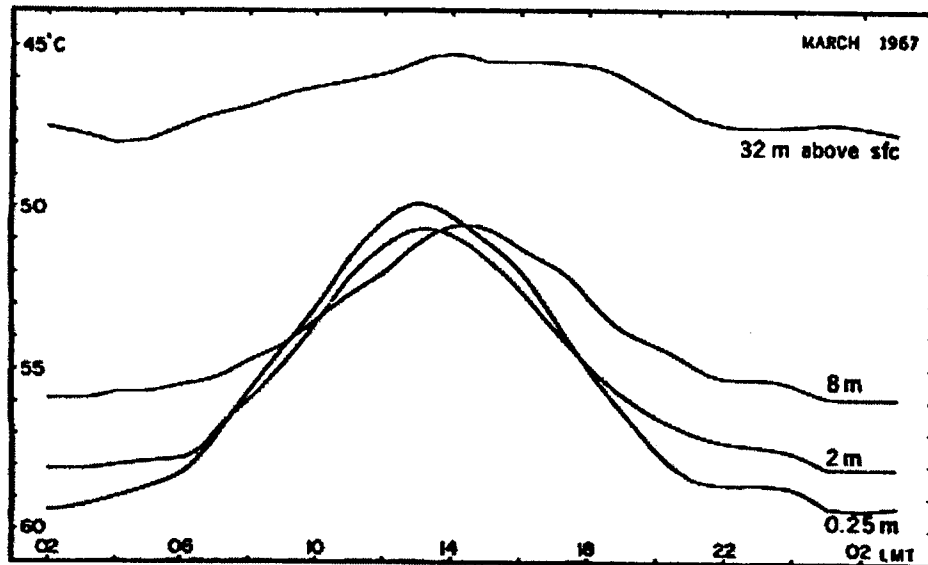


Figure 5.2: Variation of temperature inversion over a 24 hour period in March 1967 at Plateau Station, showing the effects of diurnal variation. The effect is strong close to the surface, and almost negligible above the 32 m level (Schwerdtfeger 1984)

across the plateau, according to pressure altitude, then it may be that Dome C also has a somewhat narrower inversion, while at Dome A it could be significantly narrower again.

Without discussing wind characteristics at each site for a moment, the results of our  $C_N^2$  measurements of boundary layer turbulence at the South Pole are clearly associated with vertical fluctuations in  $dT/dz$  in the boundary layer. The seeing contributions are generally proportional to the magnitude of the temperature fluctuations, for a given strength of wind shear. This indicates that individual turbulent disturbances in the boundary layer at higher sites may be greater in magnitude than those observed at the South Pole due to the combined effect of both of these differences: a stronger inversion, extending over a smaller vertical distance, means that the temperature *gradient* may be significantly steeper, especially close to the surface. Any mechanical turbulence, then, of a similar sort to that experienced at the South Pole would naturally produce more intense turbulent cells, in terms of  $C_N^2$ , following the results of Chapter 4, Section 4.2.

A narrower inversion also has implications from the point of view of image

correction techniques. We now know that the concentration of optical turbulence at the South Pole very close to the surface leads to very favourable conditions for the application of adaptive optics (see Section 4.4). If the boundary layer at the higher sites does turn out to extend over a shorter distance, this argument applies even more forcefully, regardless of the baseline seeing. The main conclusion of Section 4.4 is that a system designed to correct only the boundary layer seeing would be applicable over a characteristic angle of about 1–2' in the visible, at the South Pole. This is with a boundary layer about 200–250 m deep; some of the balloon flights with relatively narrow boundary layers give correction angles up to double the average value. Hence, any significant reduction of the height of the boundary layer at a place like Vostok or Dome C could result in a large increase in the angular scale, and hence the sky coverage, of adaptive optics-type image correction techniques.

What is hoped for, of course, is that the natural seeing will be better at other sites on the plateau, and the wind conditions must be considered before this possibility can be dismissed. A conclusion that came through strongly from the  $C_N^2$  radiosonde data (and, to some extent, the data from the mast) was that fairly strong wind shears within the boundary layer are a necessary ingredient of strong optical turbulence (e.g. Fig 4.4(a)). It is possible to have clear seeing through a deep inversion if there are no strong wind shear regions; peaks in  $dT/dz$  will not do the damage on their own. The available wind data from other sites on the plateau suggest that, here too, the effect on the seeing is likely to be somewhat different to that observed at the South Pole.

## 5.2 Wind comparisons

South Pole Station is located well down from the peak of the plateau, and lies on a gentle slope with a gradient of approximately  $1.0 \times 10^{-3}$ . This is roughly the same as Vostok and Plateau stations. These gentle slopes are enough to generate an inversion wind with an average speed of just over  $5 \text{ ms}^{-1}$  at both the South Pole and Vostok (see Table 5.1). The directional constancy is very high: around 0.8 at Pole and Vostok, slightly lower at Plateau, with the vectored average wind blowing in a direction oriented at about  $30^\circ$  to the fall line of the terrain. This is an indication that the ubiquitous inversion wind dominates the surface flow, but is modified in direction to some extent, by the lesser effects of synoptic air flows and

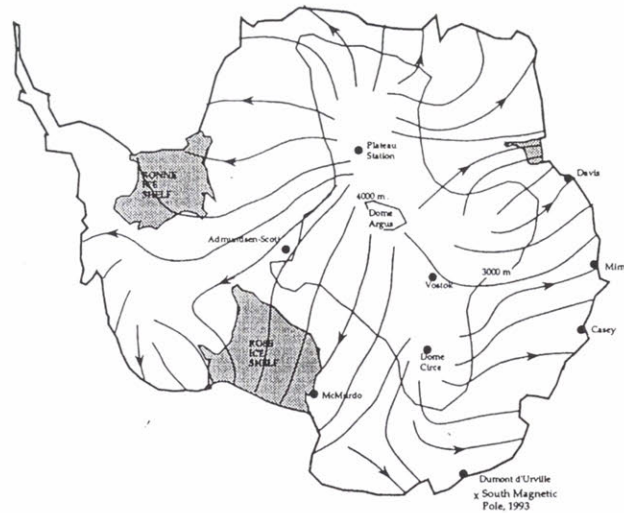


**Figure 5.3:** Contour map of surface wind directions over Antarctica, taken from Dopita (1993), based on results of Schwerdtfeger (1984)

the coriolis effect. The calculated average flow lines for the surface winds across the continent are shown in Fig. 5.3. This figure illustrates the importance of the local topography on the wind characteristics at any given location.

Since the geostrophic winds above the boundary layer do not generally blow from the same direction as the inversion wind, at the South Pole at least, there are inevitably shear layers in the boundary layer, where the winds change both speed and direction. The effect of this on the seeing is plainly illustrated by Fig. 4.4, and in the relationship between the average  $C_N^2$  profile and both the temperature and wind velocity gradients shown in Fig. 4.5. To restate one of the main conclusions of Chapter 4: virtually all of the turbulence responsible for the seeing occurs in layers where wind shear causes disturbances in the vertical temperature gradient. This statement describes almost all of the observed optical turbulence at the South Pole, and explains why the overwhelming majority of the seeing arises from the boundary layer.

Very close to the surface, looking at the data from the tower, the effect was noticeable too. Referring back to the four broad categories deduced from the mast data (Section 3.2.2), it seems that when the wind blows from close to  $90^\circ$  at the surface (i.e. the inversion wind dominates the flow) the surface layer is relatively stable, although one might still expect turbulence above this region. On the other hand, strong optical turbulence was often recorded with other wind directions.

The situation at Dome C is rather different. Here, the terrain is almost perfectly flat, and the inversion wind is negligible. Wind speeds are generally much lower ( $2.8 \text{ ms}^{-1}$  on average), with a lower constancy factor (about 0.5), reflecting the fact that the wind direction is determined by weather patterns rather than the slope of the terrain. A more detailed study of some of the monthly AWS data reveals that Dome C enjoys winds of less than  $2 \text{ ms}^{-1}$  roughly 50% of the time during winter, and below  $4 \text{ ms}^{-1}$  up to 80% of the time. This compares with approximate figures of 10% and 50%, respectively, at the South Pole. Dome C is a very calm site.

The absence of an inversion wind means that this source of turbulence, at least, can be discounted. The kinds of wind shear layers observed at the South Pole ought not exist. There may be other sources of vertical wind gradients, such as those observed occasionally in the free atmosphere over the South Pole. There is a possibility that there is in fact no significant source of mechanical turbulence in the boundary layer, in which case the seeing could be very good from ground level. Dome C, along with Dome A, may be an oasis of calm in the turbulent inversion layer stretching right across the plateau.

These considerations give us some reason to be hopeful that the oft-quoted “super seeing” may be available at one of these sites. The conclusion is very much speculation, though, based as it is on nothing more than the absence of the inversion wind. It is, of course, vital that some measurements be made of atmospheric turbulence at Dome C. The collection of this important information should become possible over the next few years. Dome C is the site of the new Franco-Italian “Concordia” station, which will support its first winter crew in 2003, according to current schedules. Before this time, the site will play host to the AASTO (the Automated Antarctic Site-Testing Observatory), which is essentially an AGO modified for astronomical site-testing (Storey et al. 1995). This experiment will include sky monitors through the near and mid-infrared wavebands, as well as a SODAR and a DIMM for measuring the seeing and the structure of the boundary layer.

Another feature of South Pole seeing is the remarkably quiescent free atmosphere (Section 4.2.3). Upper-level jet streams associated with the tropopause are virtually absent in the data, and very few other significant sources of turbulence were observed (see Figures 4.3, 4.8). From the long-term records, the strong upper-troposphere winds (jet streams) that limit the seeing at mid-latitude sites are virtually absent. At the 300 hPa level (about 10 km altitude at the South Pole),

winds of over  $30 \text{ ms}^{-1}$  occur 5% of the time, and over  $40 \text{ ms}^{-1}$  a mere 1%. This is compared with 14% / 3% at Byrd Station ( $80^\circ\text{S}$ ), and larger values further north. So it would appear that the free atmosphere is somewhat less stable as one moves out from the centre of the polar vortex, and there would probably be a corresponding increase in upper-atmosphere turbulence. Hence the average free atmosphere may be somewhat worse than the very low value of around  $0.3''$  (upward from 200 m) measured at the South Pole.

Once again, it is important that some experimental evidence be obtained at Dome C in the next few years. Accurate characterisation of the free atmosphere may require a campaign of microthermal balloon sondes, although there are some surface-based experiments such as the Scidar which do have some success in identifying high-altitude turbulence.

In summary, the available evidence suggests that the high-altitude sites such as Domes A and C probably experience better boundary layer seeing than the South Pole. Given that this is by far the dominant source of image degradation at the Pole, this is a very important result. The conclusion is based on the absence of the inversion winds that generate much of the wind shear responsible for the mechanical turbulence.

In addition, the inversion layers themselves may be significantly narrower at the higher sites. It has been shown in Section 4.4 that the narrow turbulent region at the South Pole, relative to mid-latitude sites, greatly increases the characteristic angles over which image correction techniques can be applied. The higher sites may also, therefore, be significantly better in terms of their potential for adaptive optics.

# Chapter 6

## CONCLUSION

An observatory can only be as good as the site upon which it is located. Spatial resolution is a critical parameter for any telescope, and in the optical and infrared wavelengths this is generally limited by the astronomical seeing at a site. These are the result of refractive index fluctuations caused by the micro-turbulent changes in the temperature of the atmosphere along the sight line of a light ray. This thesis investigates the seeing in Antarctica, in particular over the South Pole and the summits of the Antarctic plateau, Dome C and Dome A.

The high, dry and cold air above the Antarctic plateau provides many advantages for astronomical observations, from visible to millimetre wavelengths. Notable are the reduced thermal backgrounds and increased transmission – resulting from lower intrinsic emission at the colder temperatures from temperate sites, reduced particulate concentrations in the atmosphere lowering the emissivity, and the lower water vapour content, again lowering the emissivity but particularly opening up new windows for observation. However, it is the stability of the atmosphere that is the critical feature with regards to the seeing. The thinness of the surface inversion layer, combined with high altitude disturbance from the jet stream rarely intruding, suggest that the seeing conditions will be very different in Antarctica compared to temperate latitude locations, and possibly provide conditions of extraordinary stability and therefore low seeing. This thesis aimed to find out whether this was indeed so.

Microthermal turbulent measurements were conducted of the air column above the South Pole through the winter months of 1994–1996 in two experiments. The first experiment used an array of sensors placed at three levels on a tower that was

27 m high. The seeing contribution from this narrow region was high compared with similar measurements taken at temperate-latitude sites, with a mean value of  $0.64''$ . The turbulence was found to often decrease significantly over the height of the tower. The second experiment involved launches of balloons bearing microthermal temperature probes, allowing the atmospheric column to be examined. A marked division of the atmosphere into two characteristic regions was observed. The first was a narrow, but highly turbulent boundary layer extending over the lowest 220 m of the atmosphere. The second was a stable free atmosphere above it. The mean seeing, averaged over 15 balloon flights, was found to be  $1.86''$ , but the free atmosphere component contributed only  $0.37''$  to this. The seeing from above 200 m is greatly superior to that measured at temperate latitude sites. The surface boundary layer contribution is correlated with both a strong temperature inversion and wind shear. The proximity of the seeing layer to a telescope at the South Pole would lead to increased isoplanatic angles and coherence times from temperate sites, so facilitating adaptive optics measurements, even though the total seeing is inferior to the temperate sites. These parameters are quantified for the South Pole.

The South Pole, however, at 2,835 m, is on the flank of the plateau and suffers from the katabatic air flow off the summit at Dome A, which disturbs the seeing in the surface inversion layer. Better sites than South Pole might be expected to be found on the summits of the plateau, in particular at the accessible site of Dome C. This thesis considers what the seeing conditions on the summits of the plateau might be, in light of the measurements made at the South Pole. The depth of the inversion layer will be much less than the Pole, with a strong temperature gradient within it, but there will also be a much lower wind speed gradient because of the lower overall wind speeds. Conditions of "super-seeing" are predicted to occur on the summits of the plateau at times, and measurements are called for to test this prediction.

Since the work for this thesis was completed, subsequent measurements examining the predictions made here have been conducted from Dome C. The results do indeed indicate that there are periods of extraordinary good seeing conditions. A mean value of  $0.27''$  for the V band was determined from the first 6 weeks of winter-time data to be obtained from the site (Lawrence et al. 2004), a value less than half that measured on Mauna Kea. For more than 25% of the time the seeing is below  $0.15''$ , values never attained from temperate locations. The daytime seeing has also

been shown to be very good, being less than  $1''$  for much of the time (Aristidi et al. 2003), and falling as low as  $0.2''$ . Since the seeing varies as  $\lambda^{-1/5}$ , these results suggest that a 2 m-sized telescope in Antarctica would have near-diffraction-limited performance longward of the H band ( $1.65\mu$ ) in average seeing conditions, and if using tip-tilt optics be able to obtain near-diffraction limited images even in the optical bands.

# References

- ESO-VLT working group on site evaluation, 1987, VLT report no. 55., M. Sarazin (ed)
- Allen C.W., 1973, *Astrophysical Quantities*, The Athlone Press, London
- Ashley M.C.B., Burton M.G., Lloyd J.P., Storey J.W.V., 1995, SPIE, 2552, 33
- Ashley M.C.B., Burton M.G., Storey Lloyd, J.P., J.W.V., Bally J., Briggs J.W., Harper D.A., 1996, PASP, 108, 721
- Aristidi, E., Agabi, K., Azouit, M., Fossat, E., Vernin, J., Travouillon, T., Lawrence, J.S., Meyer, C., Storey, J.W.V., Halter, B., Roth, W.L. & Walden, V. 2005, A&A, 430, 739
- Bally J., Theil D., Billawala Y., Potter D., Loewenstein R.F., Mrosek F., Lloyd J.P., 1996, Proc. Astron. Soc. Aust. 13, 22
- Barletti R., Ceppatelli G., Paternò L., Righini A., Speroni N., 1976, J. Opt. Soc. Am. 66, 1380
- Bely P.-Y., 1987, PASP 99, 560
- Bester M., Danchi W.C., Degiacomi C.G., Greenhill L.J., Townes C.H., 1992, ApJ 392, 357
- Buften J.L., 1973, Appl. Opt. 12, 1785
- Burton M.G., Aitken D.K., Allen D.A., Ashley M.C.B., Cannon R.D., Carter B.D., DaCosta G.S., Dopita M.A., Duldig M.L., Edwards P.G., Gillingham P.E., Hall P.J., Hyland A.R., McGregor P.J., Mould J.R., Norris R.P., Sadler E.M., Smith C.H., Spyromilio J., Storey J.W.V., 1994, Proc. Astron. Soc. Aust. 11, 127

- Burton M.G., 1996, Pub. Astron. Soc. Aust., 13, 2
- Coulman C.E., 1973, Boundary Layer Met. 4, 169
- Coulman C.E., 1985, Ann. Rev. A&A 23, 19
- Cowie L.L., Songaila A., 1988, J. Opt. Soc. Am., 5, 1015
- Dierickx P., 1992, J. Mod. Optics, 39, 569
- Dopita M.A., 1993, IABO: The International Antarctic Balloon Observatory (draft copy)
- Dopita M., Ford H., Bally J., Bely P., 1996, Publ. Astron. Soc. Aust. 13, 48
- Dopita, M.A., Wood P.R., Hovey G.R., 1996, Publ. Astron. Soc. Aust. 13, 39
- Forbes F.F., 1989, SPIE 1114, 28
- Fried D.L., 1966, J. Opt. Soc. Am., 56, 1372
- Fuchs A., 1995, Contribution a l'étude de l'apparition de la turbulence optique dans les couches minces. Concept du SCIDAR generalise (PhD Thesis), Université de Nice-Sophia Antipolis, France
- Gillingham P.R., 1993, ANARE Res. Notes 88, 290, Australian Institute of Physics 10th Congress, University of Melbourne, February 1992 (publications of the Antarctic Division)
- Gur'yanov A.É., Irkaev B.N., Kallistratova M.A., Pekur M.S., Petenko I.V., Ryl'kov V.P., Semenikin A.A., Thieme N.S., Shurygin E.A., Shcheglov P.V., 1988, Sov. Astron. 32, 328
- Hufnagel R.E., Stanley N.R., 1964, J. Opt. Soc. Am. 54, 52
- Keller L.M., Weidner G.A., Stearns C.R., 1991, *Antarctic Automatic Weather Station Data for the Calendar Year 1990*, Dept. of Meteorology, University of Wisconsin, Madison WI USA
- Keller L.M., Weidner G.A., Stearns C.R., 1993, *Antarctic Automatic Weather Station Data for the Calendar Year 1991*, Dept. of Atmospheric and Oceanic Sciences, University of Wisconsin, Madison WI USA

- Keller L.M., Weidner G.A., Stearns C.R., Whittaker M.T., 1995, *Antarctic Automatic Weather Station Data for the Calendar Year 1993*, Dept. of Atmospheric and Oceanic Sciences, University of Wisconsin, Madison WI USA
- Kolmogorov A.N., 1941, in *Turbulence* (1961), p. 151, Interscience, New York
- Lawrence, J.S., Ashley, M.C.B., Tokovinin, A. & Travouillon, T., 2004, *Nature*, 431, 278
- Loewenstein R.F., Bero C., Lloyd J.P., Mrozek F., Bally J., Theil D., 1998, in *Astrophysics from Antarctica*, eds. Randy Landsberg & Giles Novak, ASP Conf. Ser., 141, 296
- Loos G.C., Hogge C.B., 1979 *Appl. Opt.* 18, 2654
- Marks R.D., Vernin J., Azouit M., Briggs J.W., Burton M.G., Ashley M.C.B., Manigault J.-F., 1996, *A&AS* 118, 385
- Marks R.D., Vernin J., Azouit M., Manigault J.-F., Clevelin C., 1999, *A&AS* 134, 161
- McIlveen R., 1992, *Fundamentals of Weather and Climate*, Chapman & Hall, London
- Merrill K.M., Forbes F.F., 1987, NNTT Technology Program Development Report no. 10, Tucson
- Murtagh F., Sarazin M., 1993, *PASP*, 105, 932
- Murtagh F., Sarazin M., 1995, *PASP*, 107, 702
- Neff W.D., 1981, *An Observational and Numerical Study of the Atmospheric Boundary Layer Overlying the East Antarctic Ice Sheet* (PhD Thesis), Wave Propagation Laboratory, Boulder CO USA
- Mightingale N.S., Butcher D.F., 1991, *MNRAS* 251, 155
- Nguyen H.T., Rauscher B.J., Severson S.A., Hereld M., Harper D.A., Loewenstein R.F., Mrozek F., Pernic R.J., 1996, *PASP*, 108, 718
- Obukhov A.M., 1949, *Izv. Akad. Nauk SSSR, Ser Geograf. Geofis.* 13, 58

- Olivier S.S., Max, C.E., Gavel, D.T., Brase, J.M., 1993, ApJ, 407, 428
- Olivier S.S., Gavel D.T., 1994, J. Opt.Soc.Am. 11, 368
- Parenti R.R., 1992, Lin. Lab. J., 5, 93
- Persson, S.E., Carr, D.M., Jacobs, J.H., 1990, Experimental Astron. 1, 195
- Phillips A., Burton M.G., Ashley M.C.B., Storey J.W.V., Lloyd J.P., Harper D.A., Bally J., 1999, ApJ 527, 1009
- Roddier F., 1981, Prog. Opt., 19, 281
- Roddier F., Gilli J.M., Lund G., 1982, J. Optics Paris, 13, 263
- Roddier F., Cowie L., Graves J.E., Sogaila A., McKenna D., Vernin J., Azouit M., Caccia J.L., Limburg E., Roddier C., Salmon D., Beland S., Cowley D., Hill S., 1990, SPIE 1236, 485
- Sarazin M., 1986, SPIE 628 Advanced Technology Optical Telescopes III, 138
- Sarazin M., Roddier F., 1990, A&A 227, 294
- Sarazin M., 1995, AO'95, Adaptive Optics Topical Meeting, Garching, M. Cullen, ESO (ed.)
- Schwerdtfeger W. (Ed.), 1984, *Weather and Climate of the Antarctic*, Elsevier Science Pub. Co. NY
- Smith C.H., Harper D.A., 1998, PASP 110, 747
- Storey J.W.V., Ashley M.C.B., Burton M. G., 1995, Publ. Astron. Soc. Aust. 13, 35
- Tallon M., Foy R., Vernin J., 1992, Laser guide star adaptive optics workshop, Fugate, R.Q. (ed), Albuquerque (10–12 March 1992)
- Tatarski V.I., 1961, *Wave Propagation in a Turbulent Medium*, McGraw-Hill, New York
- Vernin J., 1994, Recherche de site pour l'astronomie en Antarctique, Colloque Acad. Sci. Paris, 16-18 Dec. 1992, 92-96

- Vernin J., Marks R., Ashley M.C.B., Azouit M., Briggs J.W., Burton M.G., Manigault J.F., 1994, Optical Turbulence at the South Pole: First Measurements and Future Plans, XXIIIrd SCAR Meeting, Rome, Aug. 29-Sep. 1
- Vernin J., Muñoz-Tuñoz C., 1992, *A&A* 257, 811
- Vernin J., Muñoz-Tuñoz C., 1994, *A&A* 284, 311
- Vernin J., Weigelt G., Caccia J.-L., Müller M., 1991, *A&A* 243, 553
- Wilson R.W., Jenkins C.R., 1996, *MNRAS*, 268, 39